

**DEEP SPACE RADIATIONS-LIKE EFFECTS ON VO<sub>2</sub> SMART NANO-COATINGS**

**FOR HEAT MANAGEMENT IN SMALL SATELITTES**

By

**LANGUTANI EULENDA MATHEVULA**

Submitted in accordance with requirements for

the degree of

**MASTER OF SCIENCE**

in the subject

**PHYSICS**

at the

**UNIVERSITY OF SOUTH AFRICA**

**SUPERVISOR: PROF. Malik Maaza**

**CO-SUPERVISOR: PROF. Vijaya Srinivasu Vallabhapurapu**

**Date Submitted: January 2014**

# DECLARATION

**Student number: 50886940**

I declare that '*DEEP SPACE RADIATIONS-LIKE EFFECTS ON VO<sub>2</sub> SMART NANO-COATINGS FOR HEAT MANAGEMENT IN SMALL SATELITTES*' is my own work and that all the sources that I have used or quoted have been indicated and acknowledged by means of complete references.

---

Ms L.E Mathevula

---

Date

## **DEDICATIONS**

This thesis is dedicated to my mother Tsakani Joyce Mahlaule for her endless love and support. Thank you for your contribution to the success of my work.

# Acknowledgements

I thank GOD almighty for giving me the strength to finish my project. It's by his grace that I made it thus far as nothing is impossible with him.

I would like to extend my gratitude to the National Research Foundation (NRF) for financial support. Thank you very much for funding me for the two years for conducting my research.

I wouldn't be writing this thesis if it was not for my supervisor Prof M. Maaza, iThemba LABS. I really thank you for believing in me that I can make it. Your guidance is deeply appreciated.

I appreciate the guidance of my Co- supervisor Prof V.V Srinivasu, UNISA, thank you very much for helping with my work.

I greatly appreciate a support from Dr B.D Ngom for working with me and helping me with interpretation of data

I greatly appreciate the guidance and support from my Mentor Mrs N.Y Kheswa

I would also like to use this opportunity to express my gratitude to the following people:

Dr R. Nematudi, Head of Sciences, iThemba LABS, for welcoming me into the group and making me feel at home

Dr C. Pineda, Head of Material Sciences department, for making the MRD facilities available for me

Dr. R. Butcher, for helping me with XRD measurements.

Mr. P. Sechogela, for helping me with RBS and PLD

Dr. M. Nkosi, for helping in AFM imaging

Dr C.B Mtshali, for helping with proton irradiation

Prof T. Doyle, for helping with electrical measurements

Dr L. Kotsedi, for helping with all the administrative work and data analysis

Prof Basil, UWC, for helping with SEM and TEM imaging

Lastly I would like to thank my family, especially my mother Tsakani Mahlaule who has been supporting me throughout my life. I thank her for being patient with me, you are the best mother. To my late grandfather who never wanted to hear anything than education from his grandchildren, I thank you for the encouragement and support. my siblings Khensani, Nkateko and Mbuyelo, thank you for supporting me, even though it was hard for you to understands when I'm studying further, thank you for being my friends. It wasn't easy at all, but GOD was with us. Thank you!!!



# ABSTRACT

Thermal control in spacecraft will be increasingly important as the spacecraft grows smaller and more compact. Such spacecraft with low thermal mass will have to be designed to retain or reject heat more efficiently. The passive smart radiation device (SRD) is a new type of thermal control material for spacecraft. Current space thermal control systems require heaters with an additional power penalty to maintain spacecraft temperatures during cold swings. Because its emissivity can be changed without electrical instruments or mechanical part, the use of SRD decreases the request of spacecraft power budget. The (SRD) based on VO<sub>2</sub> films is one of the most important structures of the functional thermal control surface, being lighter, more advanced and without a moving devices. A large portion of the heat exchange between an object in space and the environment is performed throughout radiation, which is in turn determined by the object surface properties. The modulation device is coated on the spacecraft surface and thus provides a thermal window that can adapt to the changing conditions in orbit.

VO<sub>2</sub> is well known to have a temperature driven metal to insulator transition  $\approx 68^{\circ}\text{C}$  accompanying a transformation of crystallographic structure, from monoclinic (M-phase, semiconductor) at temperature below  $68^{\circ}\text{C}$  to tetragonal (R-phase, metal) at temperature above  $68^{\circ}\text{C}$ . This transition temperature is accompanied by an increase of infrared reflectivity and a decrease of infrared emissivity with increasing temperature. This flexibility makes VO<sub>2</sub> potentially interesting for optical, electrical, and electro-optical switches devices, and as window for energy efficiency buildings applications. This study reports on effect of thickness on VO<sub>2</sub> as well as the effect of proton irradiation on VO<sub>2</sub> for active smart radiation device (SRD) application. VO<sub>2</sub> was deposited on mica by Pulsed laser deposition techniques. The thickness of the film was varied by varying the deposition time. To characterize VO<sub>2</sub> the following techniques were performed: XRD, AFM, SEM, TEM, XPS, RBS, RAMAN and transport measurements for optical properties. The effect of proton irradiation was observed using the SEM, where the change in structure, from crystal grains to rods, was observed.

## **Keywords:**

Vanadium dioxide; transition temperature; thin film; proton irradiation; smart radiation device; tetragonal; monoclinic

# Table of Content

DECLARATION .....	ii
DEDICATIONS .....	iii
Acknowledgements.....	iv
ABSTRACT.....	vii
List of Figures .....	x
Chapter 1 LITERATURE REVIEW .....	1
1.1 Introduction .....	1
1.2 Physical properties.....	2
1.2.1 Structural properties.....	2
1.2.2 Electronic properties.....	4
1.2.3 Electrical and Optical properties.....	8
1.2.4 Characteristics of the MIT .....	9
1.3 Synthesis of VO <sub>2</sub> .....	12
1.3.1 Pulsed laser deposition .....	12
1.3.2 Chemical vapour deposition .....	13
1.3.3 Reactive evaporation/sputtering.....	14
1.4 References .....	16
Chapter 2.....	18
PROTON IRRADIATION INDUCED DEFECT IN VO <sub>2</sub> .....	18
2.1 proton-Matter interaction .....	18
2.3 References .....	25
Chapter 3.....	26
EXPERIMENTAL AND CHARACTERIZATION TECHNIQUES.....	26
1.1 Pulsed Laser Deposition.....	26
1.1.1 Characteristics of pulsed laser deposition .....	27
1.2 Irradiation setup .....	33
3.3 Characterization Techniques .....	37
3.3.1 X-ray Diffraction .....	37
3.3.2 Atomic force microscopy .....	39
3.3.3 SCANNING ELECTRON MICROSCOPY .....	42
3.3.4 TRANSMISSION ELECTRON MICROSCOPY.....	44

3.3.5 Rutherford back scattering .....	47
3.3.6 Attenuated Total Reflection.....	51
3.3.7 Raman spectroscopy .....	53
1.2.1 X-ray Photoelectron Spectroscopy .....	55
3.4 References .....	59
Chapter 4.....	62
Results and Discussions .....	62
4.1 film micro-structure study .....	62
4.2 High Resolution transmission electron microscopy (HRTEM) .....	64
4.3 Rutherford backscattering spectroscopy results .....	67
4.4 Film surface Topography.....	70
4.5 surface morphology .....	73
4.6 Electrical measurements.....	75
Chapter 5.....	82
Irradiation of VO <sub>2</sub> .....	82
5.1 Surface morphology of irradiated VO <sub>2</sub> .....	82
5.2 Surface topology .....	84
5.3 Raman Study of VO <sub>2</sub> .....	85
Chapter 6 Conclusion .....	90

# List of Figures

<b>Figure1.1</b> The phase diagram of vanadium oxygen system [6] .....	3
<b>Figure1. 2</b> VO <sub>2</sub> unit cell above (left) and below (right) the phase transition temperature. the formation of V-V pairs lead to doubling of the c parameter in the semiconducting phase .....	4
<b>Figure1. 3</b> Band structure diagram of VO <sub>2</sub> near fermi level in metallic and insulating phase as the result of the hybridization of V and O orbital based on Goodenough's description .....	6
<b>Figure1. 4</b> A set of first-order reversal curves. (a) Cooling FORC. (b) Heating FORC. Solid lines are major loops between fully insulating and fully metallic state. Dotted lines show reversal curves for three different T <sub>c</sub> .....	7
<b>Figure1. 5</b> the change of atomic structure determines the behaviour of conductivity with respect of temperature [12] .....	9
<b>Figure1. 6</b> (a) the discontinuous line shows the equilibrium path of the free energy of a system that has a semiconducting phase stable at low temperatures and a metallic phase stable at high temperatures. (b) free energy as a function of the nucleating embryo size during the VO <sub>2</sub> phase transition.....	11
<b>Figure2.1</b> The Sun-Earth connection [3] .....	19
<b>Figure3. 1</b> Mixed growth (Stranski- Krastanov).....	32
<b>Figure3. 2</b> The main principle of the van de Graff accelerator (According to R.S Shankland) .....	34
<b>Figure3. 3</b> Irradiation set-up showing the vacuum chamber .....	36
<b>Figure3. 4</b> Incident X-Rays are diffracted by the layers of atoms in a crystalline material .....	38
<b>Figure3. 5</b> Basic AFM set-up.....	40
<b>Figure3. 6</b> Schematic representation of scanning electron microscopy .....	43
<b>Figure3. 7</b> Schematic representation of transmission electron microscopy .....	46
<b>Figure3. 8</b> A collision between two positively charged particles before and after the collision. Momentum and energy is conserved [23].....	48
<b>Figure3. 9</b> Schematic representation of the experimental set-up for rutherford backscattering analysis.....	50
<b>Figure3. 10</b> Schematic diagram of the attenuated total reflection of the infrared beam in a monoreflexion ATR accessory .....	52
<b>Figure3. 11</b> Schematic of Laser Raman system.....	54
<b>Figure3. 12</b> Schematic diagram of Principle of XPS .....	56
<b>Figure3. 13</b> Schematic representation of XPS components .....	57
<b>Figure4. 1</b> X-ray diffraction pattern of VO <sub>2</sub> deposited on mica by PLD for (a) 5 min, (b) 10 min, (15) min, (d) 30 min.....	63
<b>Figure4. 3</b> shows (a) HRTEM images of VO <sub>2</sub> on mica, (b) clear lattice fringes of VO <sub>2</sub> on mica.....	65
<b>Figure4. 4</b> RBS spectrum of VO <sub>2</sub> deposited on mica by PLD. The solid red line is the corresponding fitting using XRUMP .....	68
<b>Figure4. 5</b> EDS spectrum of VO <sub>2</sub> deposited on mica.....	69

<b>Figure4. 6</b> shows the AFM scan of VO <sub>2</sub> on mica deposited for (a) 50 sec, (b) 5 min, (c) 10 min, (d) 15 min, and (e) 30 min .....	71
<b>Figure4. 7</b> Graph of thickness v/s roughness of VO <sub>2</sub> on mica.....	72
<b>Figure4. 8</b> shows SEM images of VO <sub>2</sub> on mica for thickness of (a) 34.8 nm, (b) 138.6 nm, (c) 154.9nm, (d) 348.1 nm.....	74
<b>Figure4. 9</b> shows the electrical resistance as a function of temperature of VO <sub>2</sub> on mica for the thickness of (a) 34.8 nm, (b) 138.6 nm, (c) 154.9nm, (d) 348.1 nm .....	77
<b>Figure4. 10</b> O1s and V2p spectra and fit of VO <sub>2</sub> on mica polycrystalline for (a) 34.8 nm, (b) 138.6 nm, (c) 154.9 n, (d) 348.1 nm.....	79
<b>igure5. 1</b> shows the SEM images of VO <sub>2</sub> on mica with fluency of (a) 18 x10 <sup>15</sup> ions cm <sup>2</sup> , (b) 36 x 10 <sup>15</sup> ions cm <sup>2</sup> , (c) 72 x 10 <sup>15</sup> ions cm <sup>2</sup> , (d) 110 x 10 <sup>15</sup> ions cm <sup>2</sup> , (e) 140 x 10 <sup>15</sup> ions cm <sup>2</sup> , (f) 210 x10 <sup>15</sup> ions cm <sup>2</sup> .....	83
<b>Figure5. 2</b> Graph showing the roughness v/s fluency of VO <sub>2</sub> on mica irradiated thin film.....	84
<b>Figure5. 3</b> Raman shift of non-irradiated VO <sub>2</sub> on mica.....	87
<b>Figure5. 4</b> Raman shift of irradiated VO <sub>2</sub> on mica.....	88

# Chapter 1 LITERATURE REVIEW

## 1.1 Introduction

Transition metal oxides exhibit many fascinating phenomena, such as high-temperature superconductivity, colossal magneto resistance, and insulator-metal transition. In these oxides, competing states can often coexist and form Nano- or micro scale domains of different phases. This inhomogeneity often obscures the intrinsic property of individual phases and makes it challenging to test theoretical models based on homogeneous system [1].

Metal-insulator transition (MIT) is a physical phenomenon in which material undergoes an abrupt change from insulating or semi-conductive state to conductive metallic state. Depending on the material, the change of resistivity can be 4 to 9 order of magnitude. Besides the electrical conductivity, also other physical properties of material can significantly change during the transition. One of the best known MIT materials is vanadium dioxide ( $\text{VO}_2$ ). The MIT of  $\text{VO}_2$  was first introduced by Morin in 1959. [2].

Vanadium oxides are a rich and diverse family of compounds with several applications. Vanadium dioxide ( $\text{VO}_2$ ) undergoes a well-documented transition from a semiconductor to a metal at  $\sim 340$  K, accompanied by a structural change. Above this temperature,  $\text{VO}_2$  adopts the tetragonal rutile structure and is metallic. Below the transition temperature,  $\text{VO}_2$  is monoclinic, because of the pairing of V atoms, and this is associated with semiconducting behaviour, with a band gap of  $\sim 0.7$  eV. The resistivity of  $\text{VO}_2$  in its metallic state is in the range of  $2 \times 10^{-4}$  to  $5 \times 10^{-4} \Omega \text{ cm}^3$  and displays a sudden and large increase when cooled below the transition temperature. Changes in electrical properties drive large changes in optical properties between the low- and high-temperature phases; the low-temperature monoclinic structure is somewhat infrared (IR)-transparent, whereas the tetragonal phase is opaque [3]

Much experimental work was carried out on this material, and the gross features of its electronic structure are understood. However, only qualitative and unsatisfactory explanations of the transition were given so far. From an application's point of view this is the most promising material since the material's transition temperature can be changed between  $-150$  and  $150^\circ\text{C}$  by proper doping, without affecting the abrupt and large change in the conductivity at  $T_t$  [4].

## 1.2 Physical properties

### 1.2.1 Structural properties

Since Morin investigated the thermo-conductive properties of several transition-metal oxides in the late 1950's, research has been undertaken to understand the nature of this transition and utilize these properties in various applications. The transition was named a metal-to-insulator transition owing to the change in conductive properties of the material, but other properties of these materials soon become apparent and the transition has since been relabelled a metal-to-semiconductor transition (MST). Optical properties also displayed discontinuous behaviour with large decrease in transmittance and increases in reflectance on passing through the transition temperature [5]

$\text{VO}_2$  belongs to the vanadium-oxygen system, as shown in Fig 1.1 below. This system is complete due to the multivalent vanadium ion but also contains a very wide range of ordered and disordered defect structures. These defect structures result in the large range of stoichiometry of vanadium oxides and the existence of the homologous series of separate oxides with the general formula  $\text{V}_n\text{O}_{2n-1}$  between  $\text{V}_3\text{O}_5$  and  $\text{VO}_2$ . This latter series can be visualized to be composed of blocks of the parent  $\text{VO}_2$  lattice bounded by defect places caused by the removal of every  $n$ th plane of anions [6].

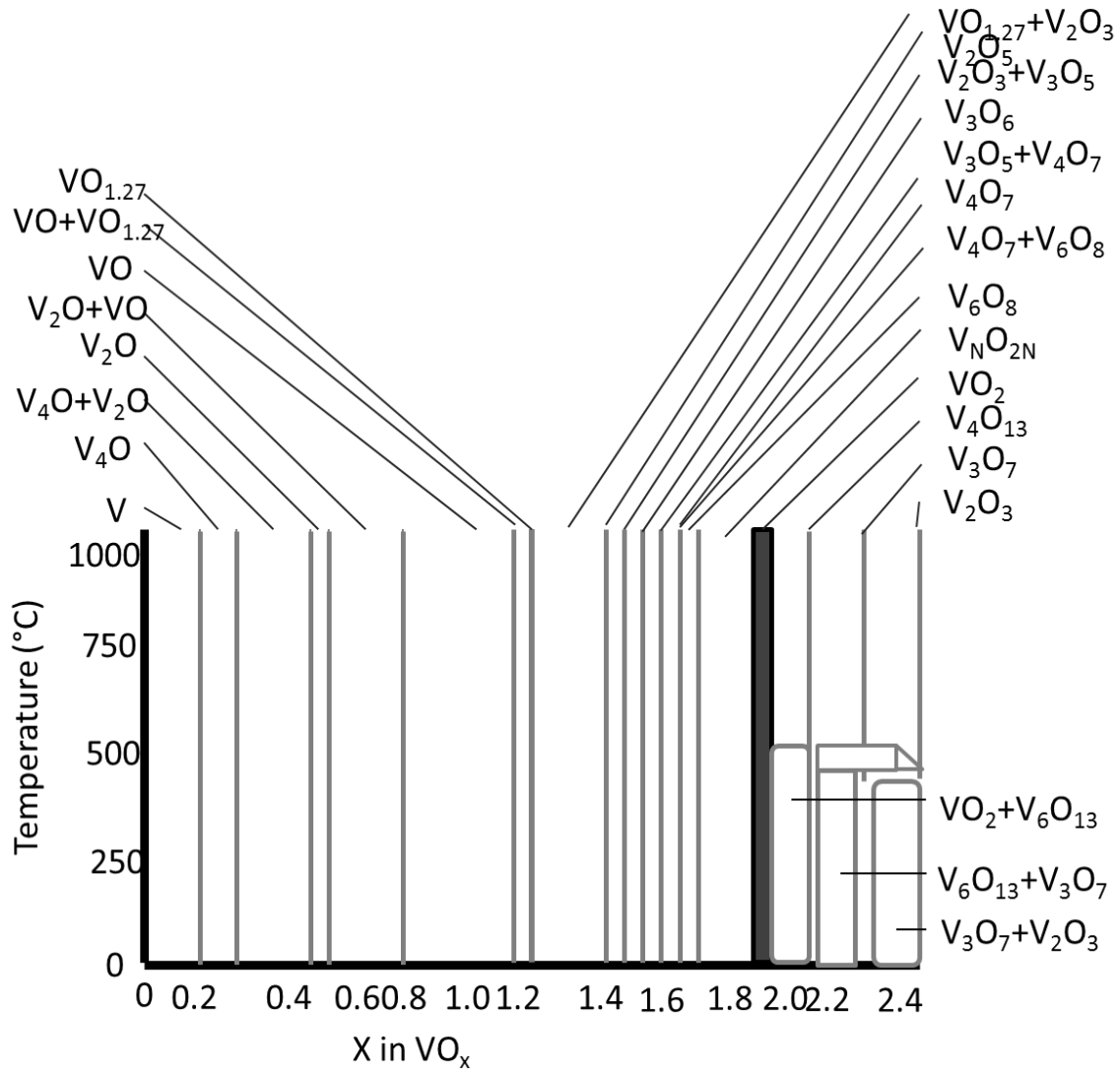


**Figure 1.1** The phase diagram of vanadium oxygen system [6]

The high temperature metallic VO<sub>2</sub> phase has the tetragonal rutile structure ( $p4_2/mnm$ ), each vanadium ion being located at the centre of oxygen octahedral. The rutile structure has the following primitive translation vectors:

$$\mathbf{a}_r = a_r \mathbf{i}, \quad b_r = a_r \mathbf{j}, \quad c_r = c_r \mathbf{k},$$

Where  $a_r = 4.55 \text{ \AA}$  and  $c_r = 2.88 \text{ \AA}$ . The subscript  $r$  refers to rutile structure, and  $\mathbf{i}$ ,  $\mathbf{j}$ , and  $\mathbf{k}$  are the usual rectangular unit vectors. Each unit cell contains two V<sup>4+</sup> ions and four O<sup>2-</sup> ions. In particular, the high-temperature phase is characterized by chains of equidistant V<sup>4+</sup> ions along the rutile  $c_r$  axis.

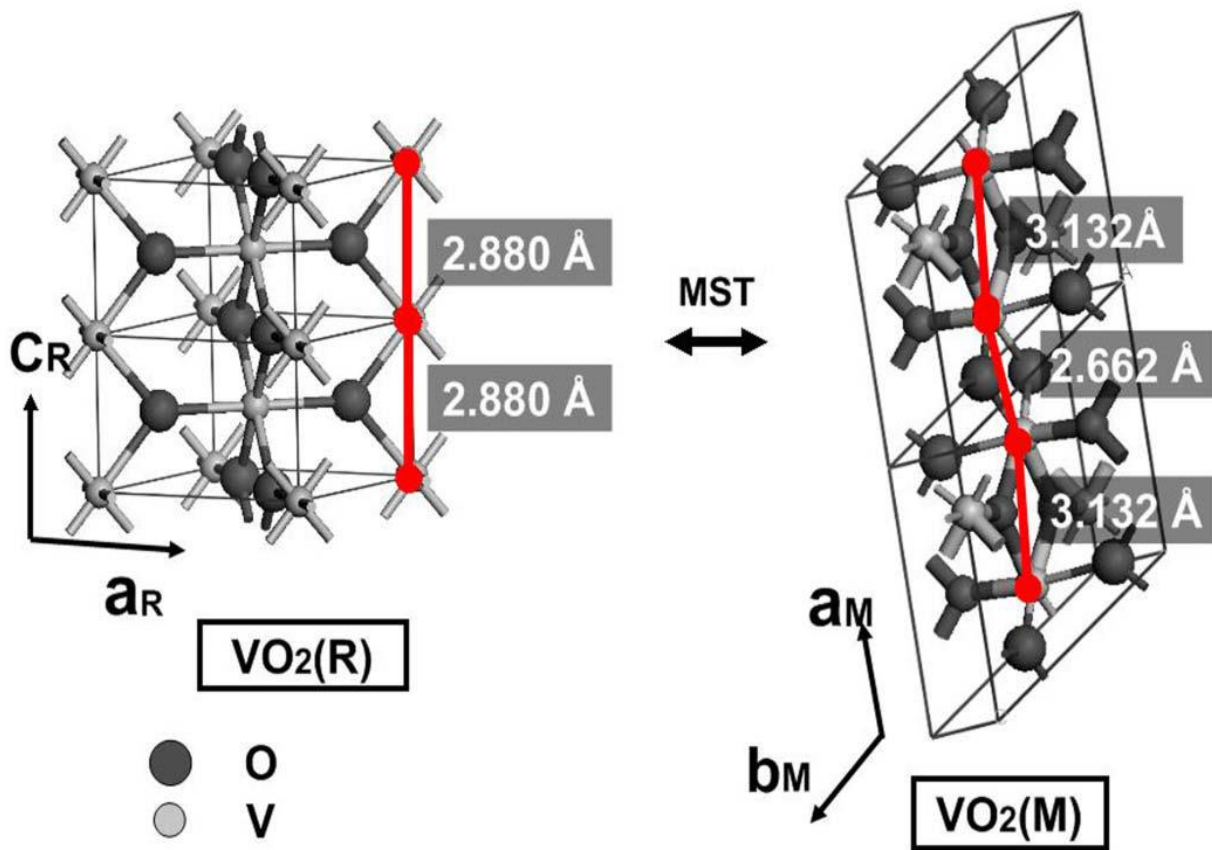


**Figure 1. 2** VO<sub>2</sub> unit cell above (left) and below (right) the phase transition temperature. the formation of V-V pairs lead to doubling of the c parameter in the semiconducting phase

On the other hand, the low-temperature insulating phase has the monoclinic structure (p21/c). The lattice parameters are  $|\mathbf{a}| = 5.75\text{\AA}$ ,  $|\mathbf{b}| = 4.56\text{\AA}$ ,  $|\mathbf{c}| = 5.38\text{\AA}$ , and  $\beta = 122.6^\circ$ . Where  $\mathbf{a}$ ,  $\mathbf{b}$ , and  $\mathbf{c}$  are the primitive translation vectors of the monoclinic structure, and  $\beta$  is the angle between  $\mathbf{a}$  and  $\mathbf{c}$ . The monoclinic structure contains four 'VO<sub>2</sub>' molecules per unit cell. A striking feature of the monoclinic phase is the presence of cation-cation pairs along the a-axis; alternate V<sup>4+</sup>-V<sup>4+</sup> separations from a zig-zag chain [7].

### 1.2.2 Electronic properties

The origin of the MIT in VO<sub>2</sub> is a subject of a debate. Two main mechanisms of the MIT have been suggested in literature. In the Peierls model, the lattice transformation at the structural phase transition temperature is accompanied by the band structure changes that result in the opening of the band gap, consequently, the MIT. In this scenario the material is referred to as band insulator. In the Mott transition model, electron correlations alone cause the transition to the insulating state, while the ion arrangement

and lattice–electron interactions are of secondary importance to the MIT. If electron–electron correlations are considered to be primarily responsible for the insulating state of  $\text{VO}_2$ , the material is often referred to as Mott or Mott–Hubbard insulator, even though current models go generally beyond the standard Mott–Hubbard picture.

The knowledge of the density of electronic states near the Fermi level is important in order to develop theoretical description of insulating and metallic phases of  $\text{VO}_2$  and understand the details of MIT. The near-Fermi level energy band structure of  $\text{VO}_2$  can be described using the level diagram based on the molecular orbital picture proposed by Goodenough [8], who described the band structure of the two phases of  $\text{VO}_2$  in terms of molecular orbital [5]. The band structure is the result of the hybridization of V 3d and O 2p levels and reflects the symmetries of the atomic arrangement in the crystal lattice. In the tetragonal metallic phase the octahedral crystal field causes the splitting of V 3d levels into  $e_g$  and  $t_{2g}$  levels. The  $e_g$  orbitals are bridged by the ligand (oxygen) 2p orbitals in the way that the bonding possesses  $\sigma$ -symmetry. The corresponding levels lie further away from the Fermi level and are depicted by antibonding  $\sigma^*$  bands (the notations are commonly used for this system).

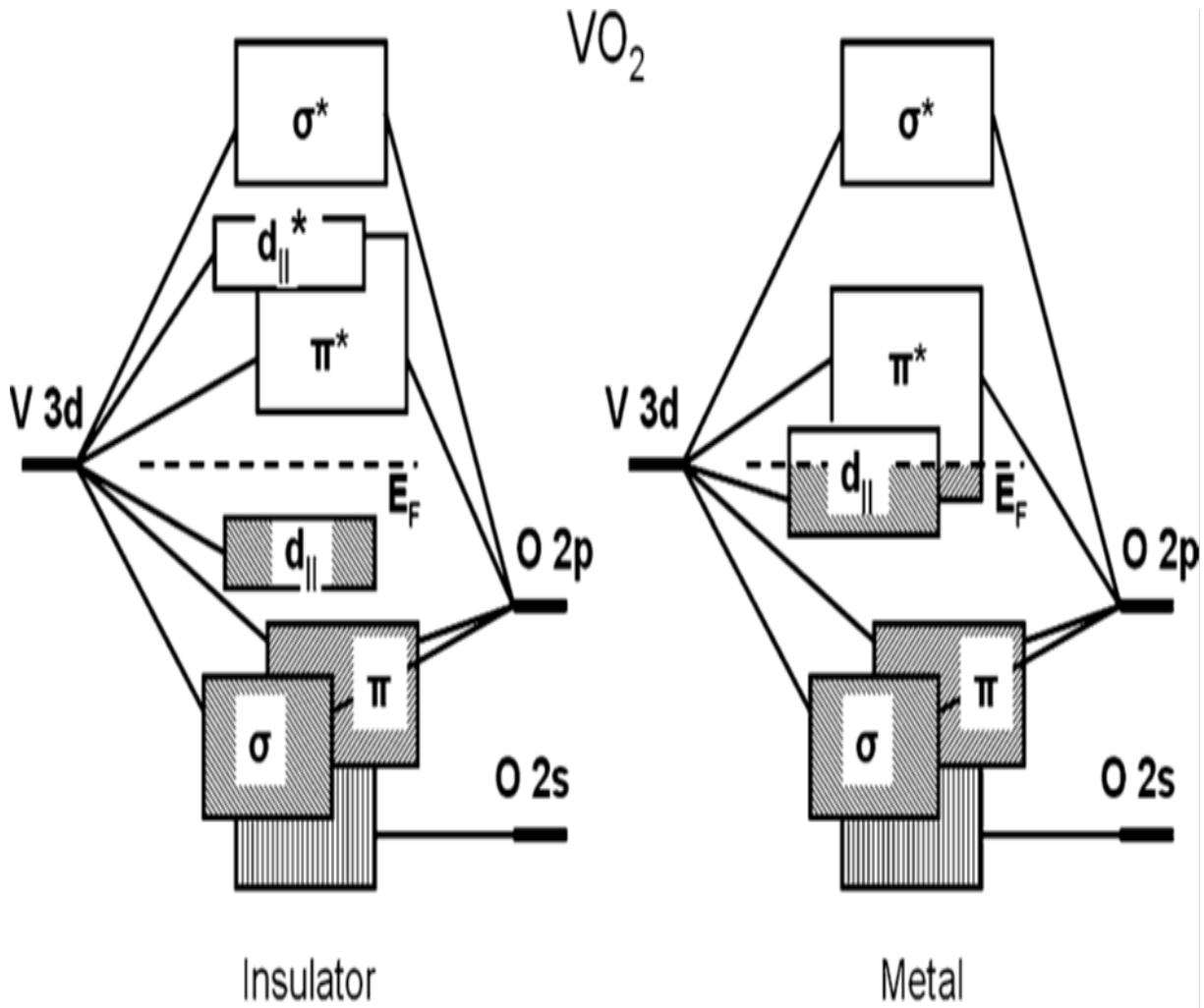


**Figure 1. 3** Band structure diagram of  $VO_2$  near Fermi level in metallic and insulating phase as the result of the hybridization of V and O orbital based on Goodenough's description

The  $t_{2g}$  levels are grouped into the bands  $\pi^*$  and  $d_{||}$  that lie right near the Fermi level.  $d_{||}$  Orbitals are aligned along the rutile c-axis and are consequently of almost 1D character. In the low-T phase (below  $T_t$ ), the dimerization of the V atoms, i.e., their pairing and tilting with respect to the c-axis as a part of the monoclinic distortion, causes the splitting of the  $d_{||}$  band into bonding  $d_{||}$  and antibonding  $d_{||}^*$  bands and the shift of  $\pi^*$  band up and away from the Fermi level. As a result, a band gap opening occurs between the top of  $d_{||}$  and the bottom of  $\pi^*$  [8].

The nature of the electronic and structural phase transition has been a matter of research and debate for over three decades with many recent experiments shedding additional light on the issue. But during this period the hysteretic nature of  $VO_2$  has received much less attention. The hysteresis nature and mechanism in  $VO_2$  are still an open question which is interesting from a basic research view point and might provide

both information regarding the MIT mechanism in  $\text{VO}_2$  and of hysteresis in general. It is also of vast importance from a technological aspect. For example, for optical memory-type applications, a large hysteresis is needed, while a small hysteresis is preferable in  $\text{VO}_2$ -based room-temperature bolometers for UV detectors. So, understanding the origin of the hysteresis can lead to a better control of its properties. The  $\text{VO}_2$  thermal hysteresis characteristics are found to vary between samples grown under different conditions, such as thickness of thin films, growth temperature, grain size, and choice of substrate [9].

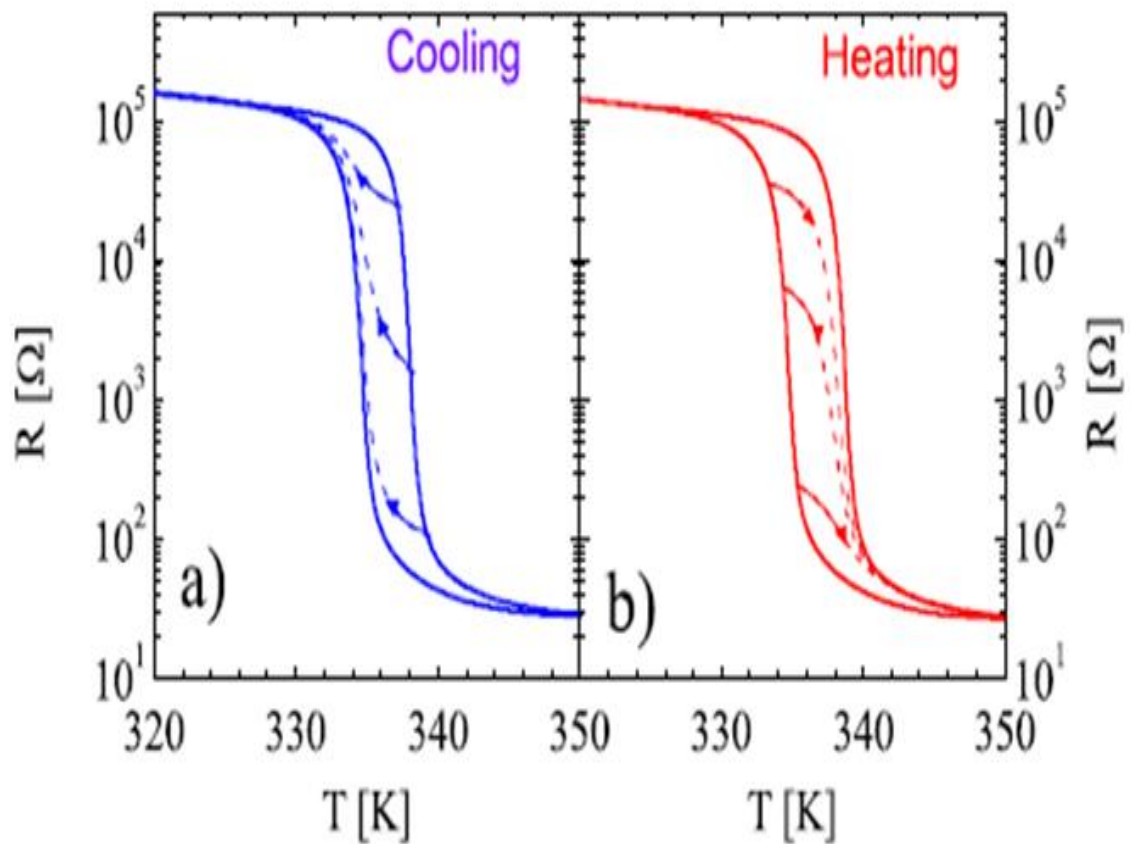


**Figure 1. 4** A set of first-order reversal curves. (a) Cooling FORC. (b) Heating FORC. Solid lines are major loops between fully insulating and fully metallic state. Dotted lines show reversal curves for three different  $T_c$

### 1.2.3 Electrical and Optical properties

VO<sub>2</sub> exhibits very fast MIT transition that can be triggered by different external excitations such as temperature change, optical excitation or charge injection. During the phase transition the electrical resistivity of the VO<sub>2</sub> thin film can decrease by several orders of magnitude. Optically the material is transparent in the semiconductor state and highly reflective in the metallic state for a large spectral range (from 1mm up to THz frequencies) [10]. The optical properties of the oxide are also greatly affected by the transition. In particular, the transmittivity of the metallic phase is lower than the one of the semiconducting phase in the near infrared region. This can be partially explained by free carrier absorption in the metal which occurs at wavelength larger than 600nm [11].

Sharp changes of the electrical properties of VO<sub>2</sub> upon the MIT are accompanied with the abrupt changes in the optical properties. The measurements made on VO<sub>2</sub> by Morin and later work done by Eastwood [12] and many others by means of the four-point technique [13] confirm that this material behaves like a semiconductor at room temperature, gradually decreasing its resistivity as the temperature is increased. At the transition temperature the resistance falls abruptly, indicating the transition from semiconductor to metallic state. If the temperature continues to be increased, the resistance of the material becomes stabilized corroborating a metallic behaviour [14]. Upon passing through the transition temperature, the electrical conductivity increases significantly. This is accompanied by a dramatic increase in infrared reflectivity, with virtually no change in the visible region. Above T<sub>c</sub>, the material reflects infrared radiation. Yet, below T<sub>c</sub>, it is transparent, which is crucial in its application as a thin film coating for "intelligent" architectural glazing [15].

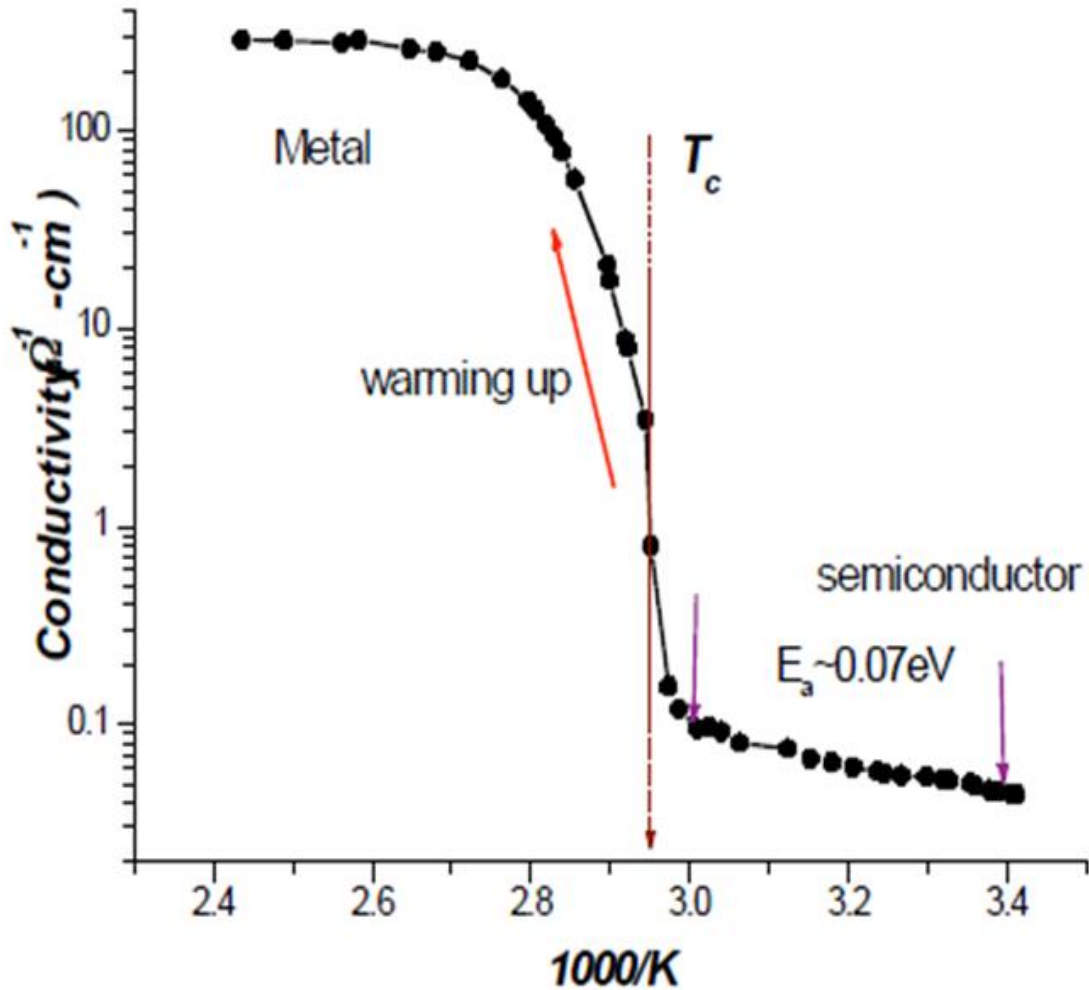


**Figure 1. 5** the change of atomic structure determines the behaviour of conductivity with respect of temperature [12]

#### 1.2.4 Characteristics of the MIT

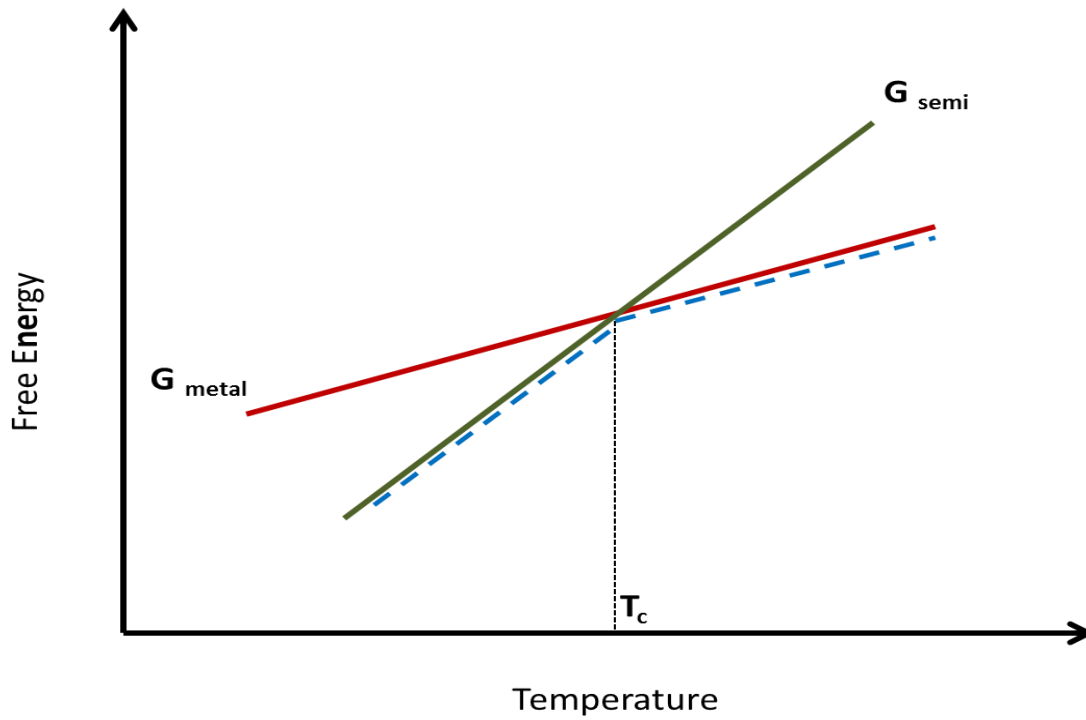
Numerous theoretical studies have been undertaken to understand the details of the MIT in transition-metal oxides and vanadium (IV) in particular. Despite these studies, the MIT is still not understood fully. Goodenough discussed the possibility of an antiferroelectric transition being the driving force for the MIT in vanadium (IV) oxide. He initially constructed an energy-level diagram for tetragonal vanadium (IV) oxide and then argued that V-V pairing becomes energetically stable on cooling after the rearrangement of the band structure in forming the monoclinic phase. In this way, he argued that there are two transition temperatures:  $T_c$  due to the antiferroelectric distortion and  $T_c$  due to the crystallographic distortion, which happens to be coincident for vanadium (IV) oxide. Goodenough concluded that the "...driving mechanism for the

low-temperature distortion in vanadium(IV) oxide is the anti-ferroelectric component of the distortion... the transition temperature  $T_c$  is controlled by the entropy of the lattice vibrational modes and not by the thermal excitation of electrons into the antibonding bands.”[5]

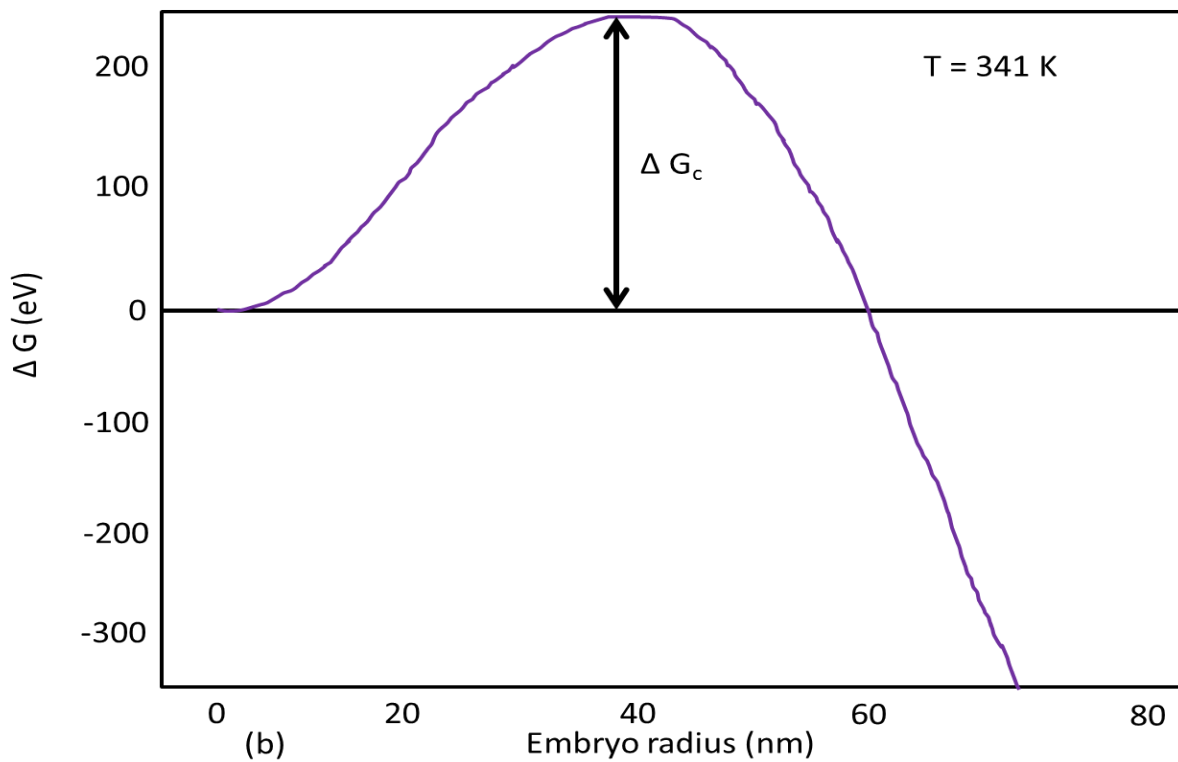
The driving force of phase transition is the reduction of the total free energy

$$G = H - TS$$

Where  $H$  is the enthalpy and  $S$  the entropy. As illustrated in figure 1.6(a) below, two phases have distinct curves  $G(T)$ . These intersect at the critical temperature  $T_c$  and the system ideally follows the lower energy path. The MIT of vanadium dioxide is a first order transition, meaning that is a discontinuity in the first derivative of the free energy at  $T_c$ . first order transitions are activated processes and some thermal fluctuations are required to overcome an energy barrier. So, the dynamics of the transition need to be taken into account [11].



(a)



(b)

**Figure 1. 6** (a) the discontinuous line shows the equilibrium path of the free energy of a system that has a semiconducting phase stable at low temperatures and a metallic phase stable at high temperatures. (b) free energy as a function of the nucleating embryo size during the VO<sub>2</sub> phase transition

A recent work based on X-ray absorption fine structure (XAFS) spectroscopy measurements clearly showed that the phase transition of VO<sub>2</sub> towards a metallic phase occurs in the intermediate monoclinic-like structure with a large twist in the V–V pairs. On the other hand, there is also considerable evidence indicating that a competing process or a causal relationship between electron–electron correlations (Mott-type transitions) and phonon contributions (Peierls-type transitions) occurs in the MIT [16]. The introduction of impurities at dopant levels can influence the temperature at which the MIT occurs. It was observed at high valent metal ions, for example, W<sup>6+</sup> and Nb<sup>5+</sup>, when substitutionally doped into VO<sub>2</sub>, decreases the MIT temperature of VO<sub>2</sub> considerably, as low as room temperature with ~2 atom percent W<sup>6+</sup>. Low valent ions, for example, Al<sup>3+</sup> and Cr<sup>3+</sup>, were shown to increase the MIT temperature [5].

### **1.3 Synthesis of VO<sub>2</sub>**

Many methods have been developed for fabricating VO<sub>2</sub> thin films, including sputtering, chemical vapor deposition (CVD), Pulsed laser deposition (PLD), and sol-gel. These methods are capable of producing VO<sub>2</sub> films with various thermochromic properties. However, if VO<sub>2</sub> is to be used in applications like smart windows, several issues must be addressed: the low visible transmittance, the weak optical contrast in the IR region, the high MIT temperature, the unfavourable color (yellow/brown), and inadequate knowledge on the durability and stability [17].

#### **1.3.1 Pulsed laser deposition**

Thermochromic thin films have also, more recently, been deposited using laser ablation. Pulsed laser deposition (PLD) is another physical vapour deposition technique, initially developed for the deposition of oxide superconductors in the late 1980s, and is ideal for metal oxide film growth and was first used for VO<sub>2</sub> deposition by Borek et al. in 1993. In PLD a high power pulsed laser beam is used to energetically remove atoms from a metal target of desired composition, which is placed inside a vacuum chamber. This can be an ultra-high vacuum, or can be carried out in the presence of a background gas, commonly oxygen when depositing oxides. The metal oxide material that is vaporized from the target is then deposited as a thin film on a substrate. One of the major advantages of PLD is the possibility of maintaining the stoichiometry of the target in the deposited films, due to the high rate of ablation allowing all elements or compounds of the target

to simultaneously evaporate. The laser source is situated outside the reaction chamber, thus the system is easy to manage. PLD is a clean, versatile, cost-effective deposition technique. However, the drawbacks include limited sample size, hence the difficulty in controlling film thickness and uniformity, and the splashing of particulates on the film, resulting surface defects under thermal shock [14]. *ZHU Pei-ran et al.* (1998) deposited VO<sub>2</sub> on (0001) sapphire substrate by PLD. They studied the dependence of the surface electrical resistance of the films on the temperature and found the semiconductor-to-metal transitions with a resistance change of  $7 \times 10^3 - 2 \times 10^4$  [18]. *S. Heinilehto et al.* (2008) prepared a VO<sub>2</sub> film by using *in-situ* PLD on r-plane sapphire substrate. As a result, vanadium oxide thin films with various compositions were produced. Thin films produced by using PLD contained also pure VO<sub>2</sub> thin films. SPM surface analysis showed that pulsed laser deposited films were very smooth with  $R_q < 16.7$  nm. The magnitude of metal-insulator transition (MIT) of the optical transmission measured from pulsed laser deposited VO<sub>2</sub> thin films was around 50% at the wavelengths of 1.5 and 2.5  $\mu\text{m}$  [19].

### 1.3.2 Chemical vapour deposition

Chemical vapor deposition (CVD) is a common industrial process for depositing high-quality and high-performance thin films. In a typical CVD process, the wafer (substrate) is exposed to one or more volatile precursors, which react and/or decompose on the substrate surface to produce the desired deposit. Frequently, volatile by-products are also produced, which are removed by gas flow through the reaction chamber. In the case of VO<sub>2</sub>, the process is almost always based on organometallic precursors, and is therefore often called organometallic chemical vapor deposition (OMCVD) or metal-organic chemical vapor deposition (MOCVD). The first deposition technique used for the deposition of VO<sub>2</sub> thin films appear to have been CVD, and after half a century it is still used extensively [20]. The main advantages of CVD are that the technique holds the ability to produce highly pure, dense materials and uniform films with excellent adhesion, high and adjustable deposition rates, at relatively low temperatures, and is reproducible [14]. *Dimitra Vernardou et al.* (2006) worked on the growth of thermochromic VO<sub>2</sub> thin film on glass, where they examine and compared three different CVD approaches and two precursor systems for the production of these materials. It is found that atmospheric pressure (AP) CVD using vanadium (IV) chloride (VCl<sub>4</sub>) and H<sub>2</sub>O on commercial SiO<sub>2</sub>-precoated glass yields the smoothest films, with transition temperature ( $T_c$ ) values of around 58°C, while APCVD using vanadyl (IV) acetyl acetonate (VO (acac)<sub>2</sub>) on the same substrates produces slightly rougher films, which

are more crystalline and possess a  $T_c$  with a value as low as 51.5 °C. Films grown using VO (acac)<sub>2</sub> in a direct liquid-injection metal-organic (DLI-MO) CVD reactor exhibited considerably poorer thermochromic and morphological properties as compared with those grown by APCVD [21]. *M. B. Sahana et al.* (2001) deposited thin film of VO<sub>2</sub> on glass by low pressure metal-organic chemical vapour deposition using the β-diketonate complex, vanadyl acetylacetonate, as the precursor. It is found that nearly monophasic, monoclinic VO<sub>2</sub>(M) films are formed in the narrow temperature range 475–520°C, films formed outside this range comprising significant proportions of other vanadium oxide phases beside VO<sub>2</sub>(M). The microstructure of these well-crystallized films varies significantly with temperature in this range. Films grown at 475°C are dense and have a very strong (200) orientation. At 520°C, films are somewhat porous, and display little preferred orientation. Film microstructure influences the semiconductor–metal transition noticeably. Films deposited at 475°C have a large change in resistance at 66°C, and display a small temperature hysteresis in the transition. The transition temperature in films grown at 520°C is higher (72°C), whereas the change in resistance is smaller and the hysteresis larger [22].

### **1.3.3 Reactive evaporation/sputtering**

Inverted cylindrical magnetron sputtering is a supplementary exceptional way to engineer nano-systems at high deposition rates onto complex shapes substrates such as the ones used in biomedical, aerospace, and machine tool industries. This exclusive geometry of an inverted cylindrical magnetron confines the plasma to a volume in which the target area is often much larger than the anode area and it presents unique challenges when sputtering dielectrics in particular. Inverted cylindrical magnetron sputtering is a promising potential vacuum technology for the synthesis of nanostructured VO<sub>2</sub> thin films [23]. Sputtering offers several advantages, such as the ability to produce uniform films, scalability to larger substrates, and efficient deposition. Although there are, of course, various disadvantages with this method, for instance, it is an off-line process with slow growth rates, relatively poor film adhesion and requires expensive equipment. By controlling the amount of material removed from the target, and the volume of reactive gas present in the deposition chamber, the composition and thickness of the film can be accurately determined [14]. *A. Lafort et al.* (2010) deposited thermochromic film of VO<sub>2</sub> by DC reactive magnetron sputtering on stainless steel substrate. In their work, Complex refractive indexes of VO<sub>2</sub> were determined by ellipsometric spectroscopy (0.35–16.5 μm) for different film thicknesses. Optical

simulations were performed to model the spectral reflectance of the film/ substrate system for a film thickness of 100 nm and 200 nm and to monitor the optical contrast of the thermochromic layers by comparing the spectral reflectance at 25 °C and 100 °C. The good agreement observed between experimental and theoretical spectra demonstrates the adequacy of the model for predicting the optical properties of the samples [24]

#### **1.3.4 Sol-gel method**

Sol-gel processing has existed for many years and has provided new view in the domain of VO<sub>2</sub> fabrication because of its low cost, its suitability for large-area deposition and the feasibility of metal doping. The basic idea is to progressively create an oxide network by a polymerization reaction of chemical precursors dissolved in a liquid medium. Generally, the chemical precursors for VO<sub>2</sub> include metal alkoxide, metaloxide, inorganic metal salts, and V<sup>IV</sup> molecular precursors, including V (AcAc)<sub>4</sub> and VO (AcAc)<sub>2</sub>. These precursors are heated to approximately 600<sup>0</sup>C in a neutral, oxygen or reduction atmosphere after spin coating or dip coating to crystallize VO<sub>2</sub> [25]. Gao et al. reported a VO<sub>2</sub>@TiO<sub>2</sub> core-shell structure, in which the VO<sub>2</sub> NANO-rod core exhibits remarkable modulation ability for solar infrared light, and the TiO<sub>2</sub> anatase shell exhibits significant photocatalytic degradation of organic dye. In addition, the TiO<sub>2</sub> over coating not only increased the luminous transmittance of VO<sub>2</sub> based on an antireflection effect, but also modified the intrinsic colour of VO<sub>2</sub> films from yellow to light blue. The TiO<sub>2</sub> also enhanced the chemical stability of VO<sub>2</sub> against oxidation. This is the first report of such a single nanoparticle structure with both thermochromic and photocatalytic properties that offer significant potential for creating a multifunctional smart coating [26].

## 1.4 References

- [1] Wei-Tao Liu, J. Cao, W. Fan, Zhao Hao, Michael C. Martin, Y. R. Shen, J. Wu, and F. Wang, *Nano Lett.*, 11, 466–470 (2011)
- [2] S. Heinilehto, J. Lappalainen, V. Lantto, H. Jantunen, *Proc. of SPIE Vol. 7022 70221G-1* (2008)
- [3] Serena A. Corr, Madeleine Grossman, Joshua D. Furman, Brent C. Melot, Anthony K. Cheetham, Kevin R. Heier, and Ram Seshadri, *Chem. Mater.*, 20 (20), 6396-6404 (2008)
- [4] David Redfield and Isaac Balberg, *rca laboratories princeton, nj 08540*, (1972)
- [5] Ivan P. Parkin and Troy D. Manning, *Journal of Chemical Education*, 83 (3), (2006)
- [6] Ganhua Fu, Metal-Semiconductor Transition Materials: FeS and VO<sub>2</sub> Thin Films by RF Reactive Sputtering, *I. Physikalisches Institut ,Justus-Liebig-Universität Gießen* (2007)
- [7] H. Nakatsugawa and E. Iguchi, *Physical Riview B* 4 (55), ( 1997)
- [8] S. Ramanathan (ed.), *Thin Film Metal-Oxides: Fundamentals and Applications in Electronics and Energy*, DOI 10.1007/978-1-4419-0664-9 2,(2010)
- [9] J.-G. Ramírez, A. Sharoni, Y. Dubi, M. E. Gómez and Ivan K. Schuller, *physical review B* 79, 235110 (2009)
- [10] Celine Eypert, Melanie Gaillet, *Application Scientists HORIBA Scientific*, (2009)
- [11] John Rozen, *Properties of Nanocrystalline Vanadium Dioxide*, (2005)
- [12] H.K.Eastwood, *Appl.Phys.Lett.*, vol 20, 93-95, (1972)
- [13] Van der Pauw, L.J., *Phillips. Res. Rep.*, 13, 1-6, (1958)
- [14] F. Mendoza<sup>1</sup> F. Fernandez, electrical properties of vo<sub>2</sub> thin films grown by pld
- [15] Pragna Kiria, Geoff Hyettb, Russell Binionsa, *Adv. Mat. Lett.*, 1(2), 86-105, (2010)
- [16] Ran Long, Bingyan Qu, Renchang Tan, Yongfu Sun, Xiaogang Tan, Wu Ying, Bicaï Pan, Yujie Xiong and Yi Xie, *Phys. Chem.*, 14, 7225–7228, (2012)

- [17] Langmuir, 26(13), 10738–1074, (2010)
- [18] ZHU Peiran, S. Yamamoto, A. Miyashita, H. Naramoto, *CHIN.PHYS.LETT*, 15(12), 94-96, (1998)
- [19] S. Heinilehto\*, J. Lappalainen, V. Lantto, H. Jantunen, *Proc. of SPIE*,7022, 70221G-2, (2008)
- [20] Joyeet Nag and R F Haglun J, *J. Phys.: Condens. Matter* (20)264016, (2008)
- [21] Dimitra Vernardou, Martyn E. Pemble, and David W. Sheel, *Chem. Vap. Deposition*, 12, 263–274, (2006)
- [22] M. B. Sahana, M. S. Dharmapakash and S. A. Shivashankar, *J. Mater. Chem.*, 12, 333–338, (2002)
- [23] J.B.K. Kana et al. *Applied Surface Science*, (254) 3959–3963, (2008)
- [24] A. Lafort, H. Kebaili, S. Goumri-Said, O. Deparis, R. Cloots , J. De Coninck, M. Voué, F. Mirabella,F. Maseri , S. Lucas. *Thin Solid Films*, 519, 3283–3287, (2011)
- [25] Y.Gaoetal., *Nano Energy*, (1) 221–246, (2012)
- [26] Yamei Li, Shidong Ji, Yanfeng Gao, Hongjie Luo, & Minoru Kanehira, *SCIENTIFIC REPORTS*, 3(1370), 1-13, (2013)

# Chapter 2

## PROTON IRRADIATION INDUCED DEFECT IN VO<sub>2</sub>

### 2.1 proton-Matter interaction

Radiation effects have been a major problem for electronic devices used in defence and space systems for many years and radiation-hardened devices, circuits and systems have been so far developed to meet the need of these systems [1]. Space represents a functional and/or durability challenge to many materials due to high levels of gamma radiation, charged particles, vacuum ultraviolet radiation and reactive atomic oxygen that are present to a greater, or lesser extent, in various orbits. These environmental factors can significantly modify the performance of the outer layers of a spacecraft. The outer spacecraft coverings control the thermal balance between the spacecraft, incident solar and terrestrial radiation, and thermal emittance to dark space. The efficient thermal control of spacecraft structure is an important issue that impacts directly on the performance and longevity of attached and internal subsystems. While spacecraft can be subjected to external temperature swings from about -150 °C to +150 °C; the corresponding internal temperature must be regulated over a nominal range. The higher the temperature controls of the spacecraft the better performance rating and the lifetime of the spacecraft subsystem and payloads. Thermal control systems typically require heaters with significant power requirements to maintain payload temperatures at acceptable levels during cold swings to compensate for the radiator heat loss to dark space [2].

Solar flares produce high energy particles and radiation that are dangerous to living organisms. However, on the surface of the earth, we are well protected from the effects of solar flares by earth's magnetic field and atmosphere. The most dangerous emission from flares is energetic charged particles (primarily high-energy protons) and electromagnetic radiation (primarily x-rays). X-rays from flares are stopped by our atmosphere well above the earth's surface. They do disturb the earth ionosphere, however, which in turn disturbs radio communications. Along with energetic ultraviolet radiation, they heat the earth's outer atmosphere, causing it to expand. This increases

the drag on earth-orbiting satellites, reducing their lifetime in orbit. Also, both intense radio emission from flares and changes in the atmosphere can degrade satellite communications [3].

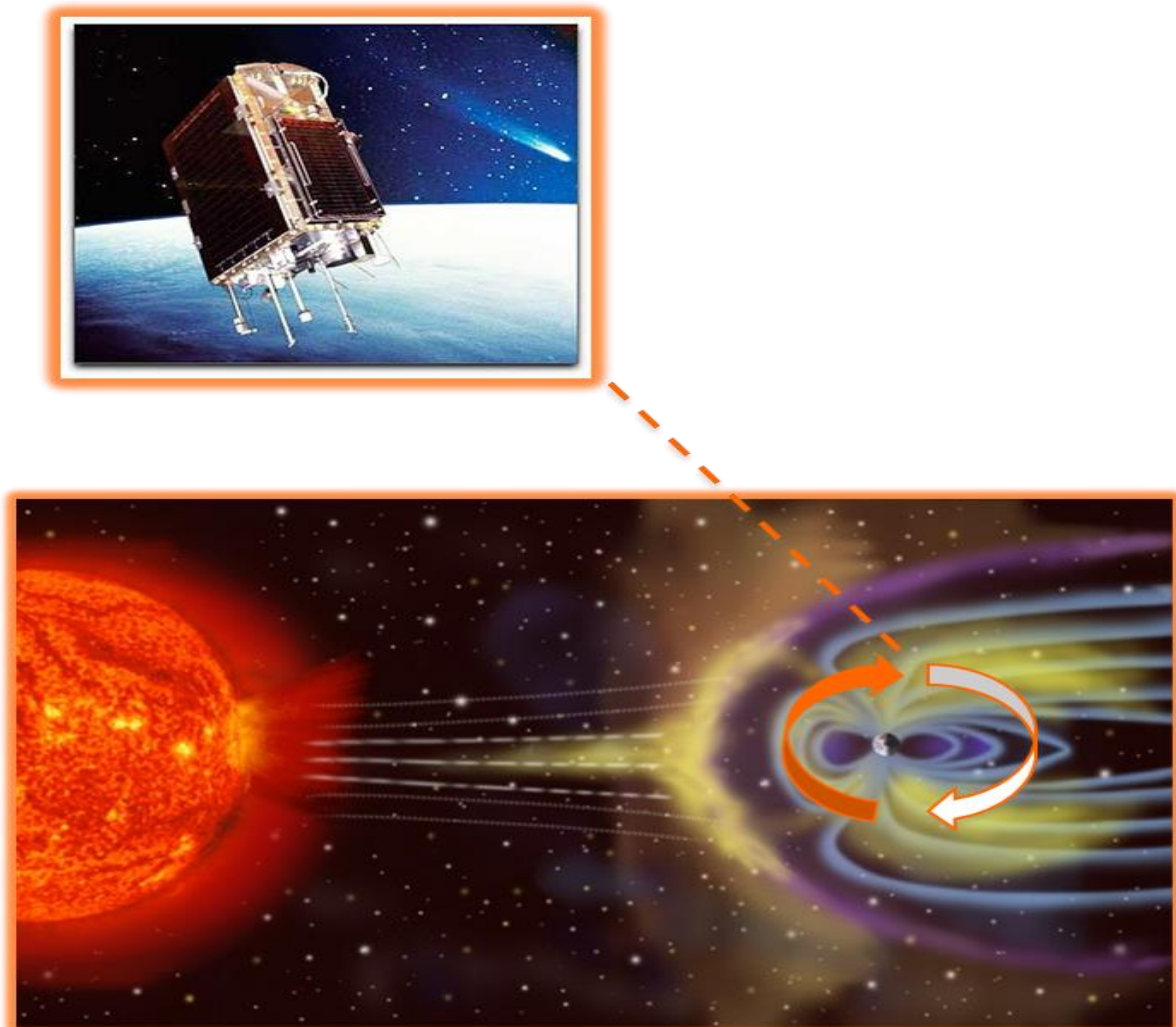


**Figure 2.1** The Sun-Earth connection [3]

The behaviour of protons when passing through matter is fundamentally different from that of a neutral radiation. Protons strongly interact with the orbital electrons of the material through which the material move. Proton loses energy in small steps through interaction with electrons in the material through which it passes. Once it loses enough energy such that it no longer has sufficient energy to excite an electron, then it loses energy by nuclear collision. As the protons slow down almost entirely due to Coulombic interaction with the atomic electrons, the electrons from a neutral atom are captured.

The slowing down is nearly continuous because of the large number of these interaction. Protons have a well-defined range of only few centimetres in air, for 4MeV proton has a range of 22 cm.

The general types of radiation effects on materials can be categorized into:

(1) **Impurity Production**, that is, transmutation of nuclei into other nuclei which themselves may be Radioactive; this mechanism is caused by neutrons through fission and activation (capture). Impurities can also be deposited from the creation of hydrogen or helium when a proton or an alpha particle, respectively, becomes neutralized in the material of passage.

(2) **Atom Displacement** from their normal position in the structure of the material; displacement atoms may leave lattice vacancies and lodge in interstitial locations or cause interchange of dissimilar atoms in the lattice structure.

(3) **Ionization**, that is, the removal of electrons from atoms in the material and the formation of ion pairs in the path of the charged particles.

(4) **Large Energy Release** in a small volume, which can result in thermal heating of the material. This may be especially important in those cases where the material is a radiation shield.

All radiation courses energy deposition within the absorbing material through the ionization process. In metals, almost all of the absorbed energy from ionization appears as heat. It is the kinetic energy deposition that generally manifests as thermal heating of the material. Radiation can cause change material properties e.g chemical, electrical, magnetic, mechanical, and electrical and more [4].

Radiation damage mechanism:

- **Displacement damage:** incident radiation displaces atoms from their lattice sites resulting in alteration of the electronic characteristics of the crystal
- **Ionization damage:** electronic ionization in insulating layers absorb energy which liberate charge carriers, which diffuse to other locations where they are trapped, leading to unintended concentration of charge and, as a consequence, parasitic field.

The displacement damage depends on the non-ionization energy loss, i.e energy and momentum transfer of lattice atoms, which depends on the mass and energy of the incident quanta. A simple measure of ionization radiation is not possible, so that displacement damage must be specific particle type and energy. Ionization effects depend on the absorbed energy, independent of the type of radiation. In general,

radiation effects must be measured for both damage mechanisms, although one may choose to combine both, for example by using protons, if one has sufficient understanding to unravel the effects of the two mechanisms by electrical measurements [5].

Protons interact with matter in three distinct ways. They slow down by myriad collision with atomic electron. They are deflected myriad collision with a nucleus, setting secondary particles in motion. The three processes are stopping, scattering and nuclear interaction. Stopping and scattering proceed via the electromagnetic (EM) interaction between the charge of the proton and the charge of atomic electrons or nucleus.

### **1. Stopping**

Protons do stop in solid matters, and at the end of range the dose is negligible. Proton range is approximately proportional to kinetic energy squared. For a mono energetic proton beam, all protons stop at nearly the same depth. The slight spread in stopping point, which increases if the incident beams itself has energy spread, is called range straggling. Most important, the rate at which the protons losses energy increases as the protons slows down because, in a given proton-electron collision, more momentum is transferred to the electron, the longer the proton stays in its vicinity. Hence, the rate of energy loss depends on the energy itself and on the stopping material.

### **2. Scattering**

The deflection of a proton by a single atomic nucleus is extremely small. Therefore the observed angular spread of a proton beams leaving a slab of matter mainly due to the random combination of many such deflections. If protons scattered in a slab of matter fall on screen, their spatial distribution is very nearly Gaussian. Materials high in the periodic table scatter much more strongly than the materials like water.

### **3. Nuclear interaction**

Because the outgoing proton retains characteristic similar to its fellows, we are not interested if the primary proton merely scatters elastically off a nucleus, or leaves it mildly excited. More interesting are the occasional train wrecks and knocks out one or more constituent protons, neutrons, or light nucleon clusters. These secondary tend to have much lower energies and much larger angles than primary protons [6].

Energetic particles and photons can interact with solids to produce atomic displacement, electronic excitations, or both. Atomic displacements result from the elastic scattering of an energetic particle by an atomic nucleus so that the kinetic energy transferred to the nucleus in the collision is sufficient to break the chemical bonds to neighbouring atoms.

The moving atom may then serve as a projectile to produce secondary displacement or, if sufficiently energetic, will ionize or otherwise excite other atoms adjacent to its path. Determination of the radiation energy at a particular point in the spacecraft requires consideration of secondary sources, as well as the processes of attenuation and scattering by intervening and adjacent materials. Common secondary sources include (1) bremsstrahlung, which are high-energy X-rays, emitted as a result of the deceleration of energetic-charged particles; (2) the gamma rays and X-rays emitted during neutron capture and inelastic scattering of neutrons; and (3) massive particles (e.g., alphas) which result from some nuclear reactions in materials. Transport of gamma rays and neutrons through absorbers can be described by the product of an attenuation factor (absorption and scattering out of the beam) and a build-up factor (scattering from the surrounding medium into the point of observation). Build-up factors are complex functions of radiation energy, materials, and geometrical configuration [7].

## **2.2 Irradiation effect on VO<sub>2</sub>**

Irradiation with high-energy particles is an important method for the study of condensed matter, and can provide information about its properties which is not obtainable by other means. One reason for this is that during irradiation a high concentration of defects in excess of the thermodynamic equilibrium concentration can be introduced in a controlled manner. This high concentration produced changes in the properties of the material by several processes, which include radiation-enhanced diffusion, radiation-induced segregation and radiation-induced precipitation, and can lead to alterations in phase stability [8]. Thermal control coatings have been widely applied on exterior surfaces of spacecraft to maintain a given thermal regime. While in-orbit, a spacecraft is subjected to the harsh effects of space environment factors, such as charged particle radiation in the earth radiation belt. With an increase in the use on spacecraft, degradation of thermal control coatings in space is drawing more and more attention [9]. Modification of semiconducting materials using beams of light ions, in particular protons, has become one of the most promising and actively developing physic-technological methods in recent years. The interest in proton irradiation is caused by the wide and controlled range of the treated depth of the material (from 0.1  $\mu\text{m}$  to 1 mm) and by the absence of complex radiation-defect clusters with high annealing temperature. The three main factors influencing variation in the semiconductor properties as a result of proton irradiation are the formation of new impurities due to nuclear reactions, the radiation-induced formation of defects, and the accumulation of hydrogen atoms. The radiation-

induced modification accomplished by the controlled introduction of defects into the material is referred to as radiation-induced doping.

In contrast to an impurity atom which is typically a defect in the composition of the material, a radiation defect is, as a rule, a structural defect of the semiconductor material. However, the influence of both composition and structural defects on semiconductor properties is similar. Typically, defect formation is accompanied with the emergence of local energy levels in the semiconductor band gap. Defect serves either as the source or trap of electrons (donors or acceptors) or as radiative (non-radiative) recombination centre for non-equilibrium charge carriers. The controlled introduction of radiation defect in combination with heat treatment makes it possible to significantly change the semiconductor electrical characteristics, such as electrical conductivity; the type of conductivity; and the concentration, mobility, and lifetime of the charge carriers [10].

A thermal smart radiation device (SRD) is a new type of thermal control material for spacecraft. Current space thermal control systems require heaters with an additional power penalty to maintain spacecraft temperatures during cold swings. Because its emissivity can be changed without electrical instruments or mechanical part, the use of SRD decreases the request of spacecraft power budget. As an SRD, a thin film should have a low emissivity at low temperature to maintain the heat, whereas at high temperature its emissivity should be high to dissipate the additional unnecessary heat [11]. There are mainly two methods for the thermal control system of the satellites, more specifically, active or passive approaches. The active approach includes all the thermal management systems that are actively electrically. This approach requires temperature sensors, actuators, control circuits, and, eventually moving parts. However, there are many problems associated with active thermal control system such as cost, risk of damage of the mechanical and the power supply system. The passive approach control the internal temperature of the satellite, known also as the thermochromic approach which is based on employing specific coatings (SRD), with an emittance that can be tailored with temperature. An SRD comprises at least one thermochromic layer to adapt its emittance to the temperature.  $\text{VO}_2$  is an interesting material for the multilayer thin film SRD because it presents one of the most significant changes of electrical and optical properties in response to external stimuli such as temperature, electric field and /or optical signal.

The observation of degree of alteration induced by proton bombardment of  $\text{VO}_2$  film may be due to details in their inherent electronic structure or those imposed by morphology. Proton irradiation is expected to introduce crystalline defects such as vanadium or

oxygen displacements (and vacancies) and hydrogen impurities for the proton energy and sample thickness. Such imperfections are likely to be responsible for the decrease in semiconductor phase resistivity and reduction observed in  $T_c$ . Production of vanadium displacement or vacancies will influence the localized V-V interactions, yielding and enhancement in the otherwise semiconducting phase conductivity and thus reducing the temperature necessary to convert the entire sample to the metallic state. Proton irradiation may also produce regions of locally mixed phases resulting in a net decrease in resistivity. Proton bombardment significantly alters semiconductor phase resistivity, infrared transmissivity, transition temperature, and the hysteresis width [12]

As materials are irradiated, their material properties change due to displacements of atoms in the crystal structure. In addition, transmutation of target atoms generates hydrogen and helium gas which can be detrimental to the material structure. The manner in which the damage manifests in the material properties varies depending upon the material, the initial material structure, the type of radiation, the irradiation dose rate and the irradiation environment (especially irradiation temperature). Many common structural materials, such as stainless steel, can withstand 10 DPA (displacements per atom) or more before reaching end of useful life. However other materials, such as graphite, suffer significant damage at doses as low as 0.1-0.2 DPA. Properties affected by radiation damage include tensile properties, ductility, He embrittlement, thermal and electrical properties, creep, oxidation, and dimensional changes (swelling). In addition, many of these effects are annealed above the irradiation temperature [13].

## 2.3 References

- [1] Ron Schrimpf, *Semiconductor Radiation Physics: From Defects to Devices*, Institute for Space and Defense Electronics, (2005)
- [2] Roman V. Kruzelecky, Emile Haddad, Brian Wong and Wes Jamroz. *Multi-function smart coatings for space applications*
- [3] <http://hesperia.gsfc.nasa.gov/rhessi2/home/mission/science/the-impact-offlares/>  
(accessed 05 may 2013)
- [4] K. E Holbert, *Radiation effect and damage*
- [5] Helmuth Spieler, *Introduction to radiation-resistant semiconductor devices and circuits*
- [6] Harald Paganetti, *PROTON THERAPY PHYSICS*, Chapter 2, p.19
- [7] NASA, *NUCLEAR AND SPACER RADIATION EFFECTS ON MATERIALS*, National aeronautics and space administration, 1970
- [8] A. TOLLEY, M.P. MACHT, M. MULLER, C. ABROMEIT and H. WOLLENBERGER,  
*PHILOSOPHICAL MAGAZINE A*, VOL. 72, No. 6, 1633-1 647, (1995)
- [9] Li et al. / *nucl. Instr. And meth. In phys. Res. B* 234 (2005) 249-255]
- [10] V. A Kozlov, V. V Kozlovski, *semiconductors*, (35) 735-761 (2001)
- [11] M. Benkahoul, M.Chakera, J.Margot, E.Hadda, R.Kruzelecky, B.Wong, W.Jamroz, P.Poinas., *Solar Energy Materials & Solar Cells*, 95,3504–3508, (2011)
- [12] A. Kone, A. m. Trione, F. Junga, *Transactions on nuclear science*, (37) 1739-1743 (1990)
- [13] P. Hurh, K. Ammigan, B. Hartsell, R. Tschirhart, *Targetry challenges at megawatt proton accelerator facilities*.

# Chapter 3

## EXPERIMENTAL AND CHARACTERIZATION TECHNIQUES

### 1.1 Pulsed Laser Deposition

One of the most versatile deposition techniques for thin film growth is pulsed laser deposition (PLD). (PLD) is a growth technique in which the photons, which have specific pulse duration, wavelength and fluence, interacts with a bulk material. A schematic and a picture of experimental setup are shown in Fig.3.1. A short-pulsed, high-power laser beam that can be varied between  $\sim 100$  fsec to 20 nsec is focused onto the target surface thereby converting a finite volume of a solid instantaneously into its vapour phase, thereby forming a luminous ablation plume. Subsequently, the vapour moves away from the target at a high velocity (several km/sec) to the substrate placed on the substrate holder in the evaporating chamber [1].

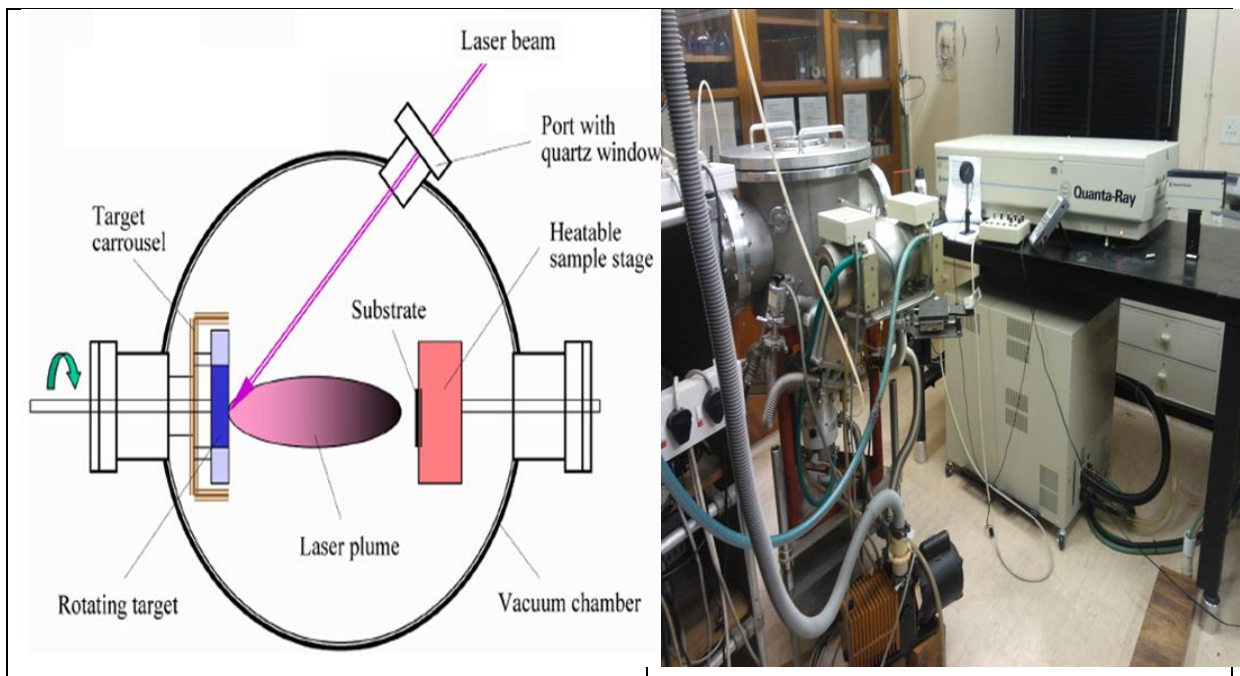


**Figure 3.1** Schematic view of a PLD-System [2]

### **1.1.1 Characteristics of pulsed laser deposition**

PLD has several characteristics that distinguish it from other deposition techniques and has advantages for the growth of oxides and other chemically complex materials because the stoichiometry of the growth film is similar to that of the target.

- The film has the same composition as the target when the focused laser energy density is chosen properly. This stoichiometric transfer is a consequence of the high initial rate of heating.
- Atoms and ions have typical initial velocity of  $\geq 10^6$  cm/s in the ablation plume, which for an atom of 100 atomic mass units correspond to a kinetic energy  $\geq 52$  eV. The kinetic and internal excitation energies of ablated species can be used to assist film formation and to promote chemical reactions, both in the gas phase and on the growing film surface
- No electron beam or hot filaments needed inside the deposition chamber, so ambient gases can be used. Energetic species in the ablation plasma react readily with gas molecules to form simple compounds (oxides, nitrides and hydrides).
- In the multilayer thin film structures, adjacent layers have different composition, but all layers share a common, continuous crystal structure. A separate target can be used to grow each layer, with a multi-target 'carousel' for rapid target exchange. The growth is inherently digital because each layer's thickness can be controlled precisely simply by calibrating the deposition rate per laser pulse and continuous pulses [2].

**The process of PLD is generally divided into four stages:**

- Laser ablation of target material and creation of a plasma
- Dynamic of the plasma
- Deposition of the ablation material on the substrate
- Nucleation and growth of the film on the substrate surface

#### **1.1.1.1 *Laser ablation of the target material and creation of a plasma***

The interaction between the laser pulse and the target depends strongly on the intensity of the incoming laser beam. In PLD, the fluency is of the order of  $10^8$ - $10^9$  W/cm<sup>2</sup> corresponding to a pulse duration of a few nanoseconds (such as those from a Nd:YAG laser). Therefore, there is enough time for the pulses to be absorbed, heat the target surface, and, finally, lead to the removal of matter. Sputtering is considered to be the

principal interaction mechanism of a laser pulse with the target. The incident photons strike the target, producing electron-hole pairs and electronic excitations in a femtosecond timescale. After a few picoseconds, the energy is transferred to the crystal lattice, and during the laser pulse, within a few ns, a thermal equilibrium between the electrons and the lattice is reached. This leads to a strong heating of the lattice and, with continued irradiation, to a massive p-particle emission from the surface.

#### **1.1.1.2      *Dynamic of the plasma***

The material that is ablated from the target is hot and, therefore, part of the atoms in the vapour is ionized. In addition, the particle cloud absorbs energy from the laser beam and becomes more ionized. Finally, fully ionized plasma is formed in the vicinity of the target. The plasma expands away from the target, much like the rocket exhaust from jet nozzles, with a strongly forward-directed supersonic velocity distribution. The visible part of the particle jet is referred to as an ablation plume. The plume consists of several types of particles: neutral atoms, electrons, and ions. Furthermore, clusters of different compounds of the target elements are observed near the target surface. Although atomic transitions have typical lifetimes of a few nanoseconds, collisions can re-excite atoms such that the emission lines are observed many microseconds after the initial laser pulse. In vacuum, the plume does not expand unidirectionally but backward velocity components appear as well because of the high density of the plasma. The ejected species diffuse in the plume and collide with each other, which lead to a rapid thermalization of the particle cloud. Moreover, the plume in vacuum is visible to the eye only in the immediate vicinity of the target. Ambient gas scatters kinetic energy distribution of the different species. In addition, reactive scattering results in the formation of molecules which are essential for the proper stoichiometry and content of the film. [3].

#### **1.1.1.3      *Deposition of the ablated material on the substrate***

During PLD the stoichiometry of the deposited film is close to that of the used target and, therefore, it is possible to prepare stoichiometric thin film from a single alloy bulk target. This stoichiometry transfer between target and substrate has made the PLD technique interesting for growth of complex systems, for instance of high-temperature superconductors, piezoelectric and ferroelectric materials with perovskite structure, and also for technical applications. Stoichiometry transfer between target and substrate is difficult to obtain with evaporation or sputtering by using a single target, because in general the partial vapour pressure and sputtering yields of the components are different

from each other which give rise to a different concentration of the thin film growing on the substrate. In the case of PLD, with most materials a stoichiometry transfer between target and substrate is obtained, which can be explained as follows.

The fast and strong heating of the target surface by the intense laser beam (typically up to temperatures of more than 5000 K within a few ns, corresponding to a heating rate of about  $10^{12}$  K/s) ensures that all target components irrespective of their partial binding energies evaporate at the same time. When the ablation rate is sufficiently high (which normally is the case at laser fluencies well above the ablation threshold), a so-called Knudsen layer is formed and further heated (for instance by Inverse Bremsstrahlung) forming a high-temperature plasma, which then adiabatically expands in a direction perpendicular to the target surface. Therefore, during PLD, the material transfer between target and substrate occurs in a material package, where the separation of the species is small. The expansion of the whole package can be well described by a shifted Maxwell-Boltzmann centre-of-mass velocity distribution

$$f(v_z) \propto v_z^3 \cdot \exp[-m_A(v_z - v_{cm})^2 / (2kT_{\text{eff}})] \quad 3.1$$

With a centre-of-mass velocity  $v_{cm}$  and an effective temperature  $T_{\text{eff}}$ . Then, adiabatic collision less expansion occurs transferring the concentration of the plasma plume towards the substrate surface. Thus one can understand that complex structures such as oxides or perovskites are built up again at the substrate surface, when the substrate temperature is high enough, because all components are transferred from target to substrate at the right composition [4].

#### **1.1.1.4 Nucleation and Film growth mechanism on the substrate surface**

The ejected high-energy species impinge onto the substrate surface and may induce various type of damage to the substrate. These energetic species sputter some of the surface atoms and a collision region is formed between the incident flow and the sputtered atoms. Film grows after a thermalized region is formed. The region serves as a source for condensation of particles. When the condensation rate is higher than the rate of particles supplied by the sputtering, thermal equilibrium condition can be reached quickly and film grows on the substrate surface at the expenses of the direct flow of the ablation particles and the thermal equilibrium obtained. Nucleation-and-growth of crystalline films depends on many factors such as the density, energy, ionization degree, and the type of the condensing material, as well as the temperature and the physico-chemical properties of the substrate. The two main thermodynamic parameters for the

growth mechanism are the substrate temperature  $T$  and the supersaturation  $D_m$ . They can be related by the following equation

$$D_m = kT \ln(R/R_e) \quad 3.2$$

where  $k$  is the Boltzmann constant,  $R$  is the actual deposition rate, and  $R_e$  is the equilibrium value at the temperature  $T$ .

The nucleation process depends on the interfacial energies between the three phases present - substrate, the condensing material and the vapor. The minimum-energy shape of a nucleus is like a cap. The critical size of the nucleus depending on the driving force, i.e. the deposition rate and the substrate temperature. For the large nuclei, a characteristic of small supersaturation, they create isolate patches (islands) of the film on the substrate which subsequently grow and coalesce together. As the supersaturation increases, the critical nucleus shrinks until its height reaches on atomic diameter and its shape is that of a two-dimensional layer. For large supersaturation, the layer-by-layer nucleation will happen for incompletely wetted foreign substrates.

The crystalline film growth depends on the surface mobility of the adatom (vapour atoms). Normally, the adatom will diffuse through several atomic distances before sticking to a stable position within the newly formed film. The surface temperature of the substrate determines the adatom's surface diffusion ability. High temperature favours rapid and defect free crystal growth, whereas low temperature or large supersaturation crystal growth may be overwhelmed by energetic particle impingement, resulting in disordered or even amorphous structures [5].

The conventional theory of film growth during deposition separate the nucleation into three different modes: three-dimensional island growth, two-dimensional monolayer formation, and growth of Separate Island on top of a full monolayer. In three-dimensional growth, the formation of film-atom clusters involves several processes that a particle can undergo after arriving on the substrate. The balance between growth and dissociation of a cluster is governed by the total free energy of the system. Either a decrease in the surface energy between the arriving atoms and the cluster or an increase in the magnitude of the negative volume free energy decrease the size of a stable cluster. As a result, the nucleation rate of the cluster increases. The quality of the deposited film is, above all, determined by the crystallinity of the lattice and the surface smoothness. The generation of particulates during the PLD process is one of the most important factors affecting the smoothness of the resulting film. [4].

During Pulsed laser deposition there are three possible film growth modes:

#### 1.1.1.4.1 Frank Van der Merwe (Layers)

- Occurs if the substrate-vapour surface energy is larger than other two combined growth models.
- A smooth film will form
- Layer growth will occur
- The film wets the surface to lower surface energy.



**Figure 3.2** Layer by Layer growth (Frank- van Der Merwe)

#### 1.1.1.4.2 Volmer Weber (Islands)

- Occurs if the total surface energy of the film interface is larger than that of the substrate-vapour interface.
- The material balls up to minimize interface with the substrate
- Uneven growth
- Slow diffusion



**Figure3. 3** Island growth (Volmmer- Weber)

#### 1.1.1.4.3 Stranski-Krastanov (Mixed)

- Initial layer growth
- Changes into island growth after a few monolayers.

- The initial layer is strained to match the substrate. After a few layers, the strain is relaxed.



**Figure 3. 1** Mixed growth (Stranski- Krastanov)

Laser ablation for thin films growth has many advantages:

- the energy source (laser) is outside the vacuum chamber which, in contrast to vacuum-installed devices, provides a much greater degree of flexibility in materials use and geometrical arrangements;
- almost any condenser matter material can be ablated;
- the pulsed nature of PLD means that film growth rates may be controlled to any desired amount;
- the amount of evaporated source material is localized only to that area defined by the laser focus;
- under optimal conditions, the ratios of the elementary components of the bulk and film are the same, even for chemically complex systems;
- the kinetic energies of the ablated species lie mainly in a range that promotes surface mobility while avoiding bulk displacements;
- the ability to produce species while electronic states far from chemical equilibrium opens up the potential to produce novel or metastable materials that would be unattainable under thermal conditions.

PLD also has technical and fundamental drawbacks, in particular:

- the production of macroscopic ejecta during the ablation process;
- impurities in the target material;
- crystallographic defect in the film caused by bombardment by high kinetic energy ablation particles;
- in-homogeneous flux and angular energy distributions within the ablation plume [6].

In this work, VO<sub>2</sub> films were prepared by reactive pulsed laser deposition using vanadium metal target and ND: YAG laser with 355 nm wavelength, having pulse energy 180 mJ at 10 Hz. The depositions were performed in a controlled gas-phase background consisting of O<sub>2</sub>. The substrate (mica) temperature was kept at 500°C and was mounted at slightly off axis with respect to the plume axis and rotated at the rate of 8 rpm during the deposition in order to get a uniform film thickness. The film thickness ranged from 10 – 348 nm. The experiment was done at laser research institute Stellenbosch University.

## **1.2 Irradiation setup**

Irradiation was done by the Van de Graff accelerator (VdG). The VdG generator is made up of a motor-driven belt stressed between two rollers, an insulating column and a spherical or rounded high-voltage terminal electrode which is installed on top of the insulating column. The belt is electrically charged by a brush or comb of metallic wires which is connected to a DC voltage source. The amount of electric charge sprayed onto the belt is controlled by the voltage. The charge, which can be negative or positive depending on the polarity of the source, is carried by the belt to the terminal electrode [7]. The principle of the VdG accelerator is illustrated in Fig 3.5 a rapidly moving belt of non-conducting material such as rubberized fabric accumulates positive charge as it passes an array of sharp spray point which transfers electrons from the belt to the spray points. The positive charge on the belt is continuously transferred by the movement of the belt away from ground. At high-voltage terminal, a hollow metal sphere or nearly cylindrical shape, another set of spray point neutralized the charge on the belt by electrons emitted from the spray point. The result is the transfer of the positive charge to the sphere. By a continuous process of transfer of positive charge to the sphere via movement of the belt a high potential relative to ground can be built up on the sphere. The limit of the voltage that can be accumulated on the hollow electrode is determined by its discharge potential to the surrounding housing. If it is insulating by some pressurized non-conducting gas such as N<sub>2</sub>, CO<sub>2</sub>, or SF<sub>6</sub>, potential of ~ 15 MV can be achieved [8].

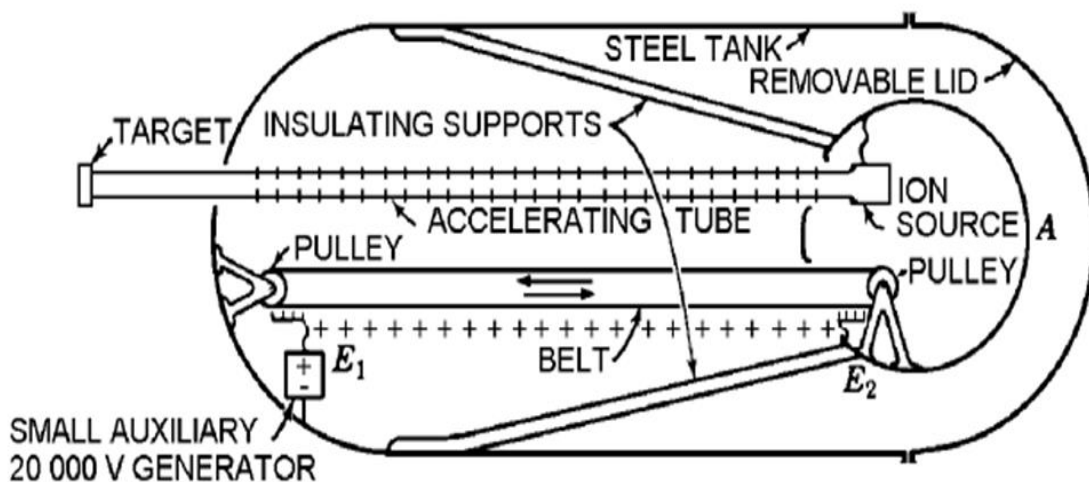


**Figure3. 2** The main principle of the van de Graaff accelerator (According to R.S Shankland)

The 348.1 nm film was irradiated at different fluencies. The film was mounted on the substrate holder, perpendicular to the beam. The experiment was done at iThemba LABS by the Van der Graaff with a Beam of  $H^+$ , Beam Energy of 2MeV, Beam spot of 2mm and a Current of 50nA.

Protons have been one of the particles of choice throughout the more than 70-years history of accelerated particles as a tool of high energy physics-indeed; 'high energy' has generally been defined by the energy of the most powerful proton accelerator available at a given time. Protons are the most common heavy particles in the trapped radiation belts, solar particle events (SPE) and the energies of greatest interest for space radiation health are from tens to hundreds of MeV, corresponding to a range of several centimetres in tissues. The effects of materials and structures on the internal radiation environment will be a constraint on the design of future spacecraft and habitats—it is already a consideration on whether to add shielding material to the ISS (Miller et al., 2003). Consequently, a great deal of effort has gone into modelling and testing the radiation transport properties of materials for use in space. Reducing the uncertainties in the model predictions is critical: the greater the uncertainty, the greater the weight penalty in the form of increased shielding thickness required under the ALARA (As Low As Reasonably Achievable) principle of radiation protection practice.

**Advantages:**

The energy range of greatest interest for space radiation application is fortuitously comparable to what has been available for many years at proton and heavy ion accelerators. Accelerators can produce well-characterized, almost mono-energetic beams, so that data can be gathered rapidly under controlled conditions for specific particles and energies, and well-defined materials and configurations. This is useful both for gathering basic physics and biology data and for calibrating flight instrument such as dosimeters. Ground-based experiments have many fewer constraints on size, power and complexity than do flight experiments, and, while access to accelerators is limited, it is much easier to obtain than access to space.

**Limitations:**

It is not practical at an accelerator to replicate the mixed radiation fields found in space. Operational spacecraft have complex internal structures that are difficult to replicate on the ground, and new structural and shielding materials are constantly being proposed. These complications have necessitated the development of models to simulate the effects of the space radiation environment under realistic flight conditions. Models and accelerator-based measurements therefore complement one another, and physics measurements and models are being coupled with biology data and models to make possible comprehensive theoretical analysis of space radiation risk and risk mitigation [8].

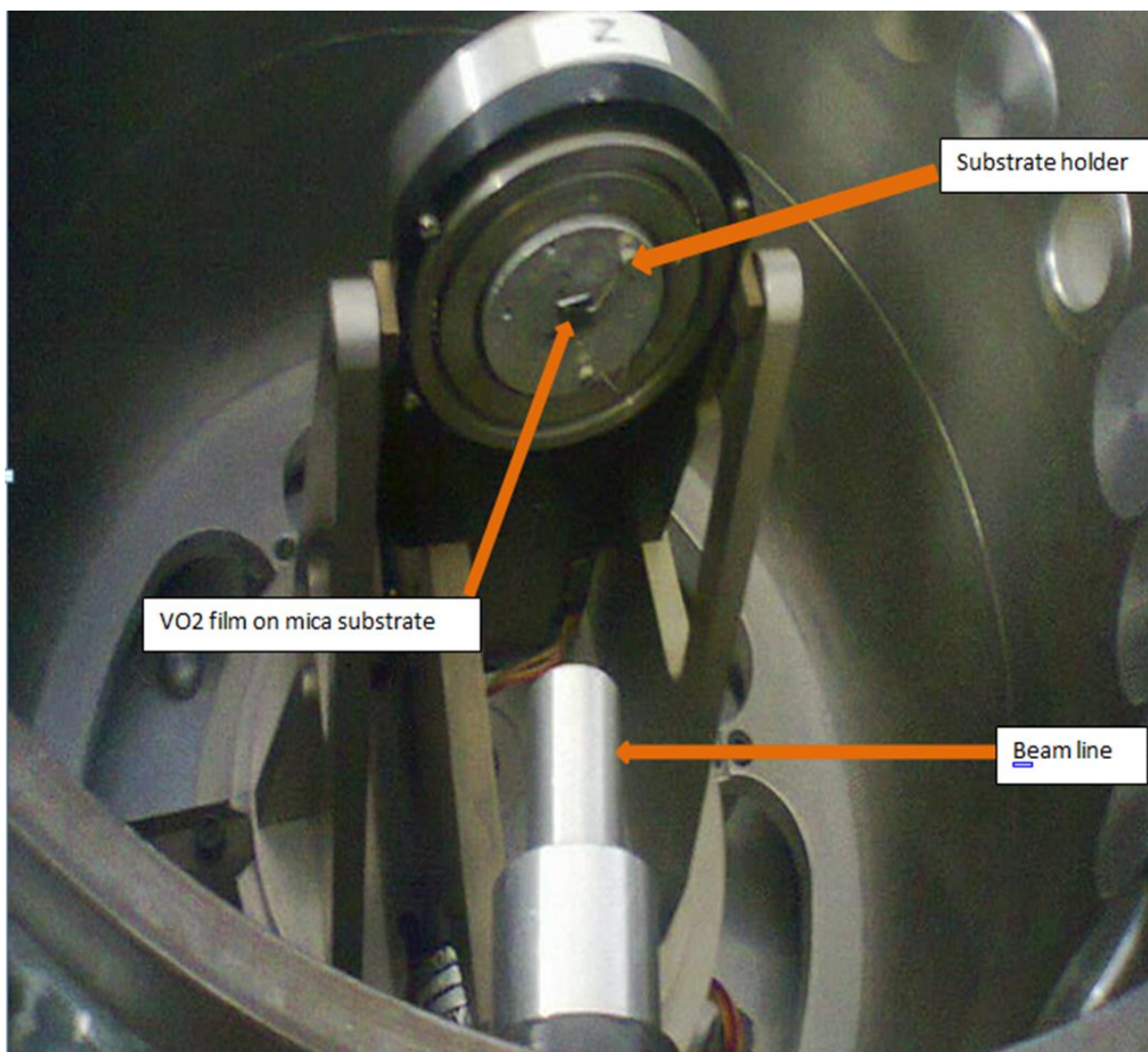


**Figure3. 3** Irradiation set-up showing the vacuum chamber

## 3.3 Characterization Techniques

### 3.3.1 X-ray Diffraction

When matter is irradiated with a beam of X photons, it emits an X-ray beam with a wavelength equal or very close to that of the incident beam, which is an effect referred to as scattering. The scattered energy is very small, but in the case where scattering occurs without a modification of the wavelength (coherent scattering) and when the scattering centres are located at non-random distances from one another, see how the scattered waves interfere to give rise to diffracted waves with higher intensities are seen. The analysis of the diffraction figure, that is, the analysis of the distribution in space of the diffracted intensity, makes it possible to characterize the structure of the material being studied. This constitutes the core elements of X-ray diffraction (XRD) [9].

XRD is an important experimental technique that has been used to address issue related to the crystal structure of solids, including lattice constant and geometry, identifying of unknown materials, origination of single crystals, defects, stress and many more. In XRD a collimated beam of X-rays, with a wavelength typically ranging from 0.7 to 2 Å, is an incident on a specimen and is diffracted by the crystalline phases in the specimen according to Bragg's law:

$$\lambda = 2d \sin \theta \quad 3.3$$

where  $d$  is the spacing between atomic planes in the crystalline phase and  $\lambda$  is the X-ray wavelength. The intensity of the diffracted X-ray is measured as a function of the diffraction angle  $2\theta$  and the specimen's orientation. The diffraction pattern is used to identify the specimen's crystalline phase and to measure its structural properties. XRD is non-destructive and does not require elaborate samples preparations, which partly explains the wide usage of XRD method in materials characterization [10].

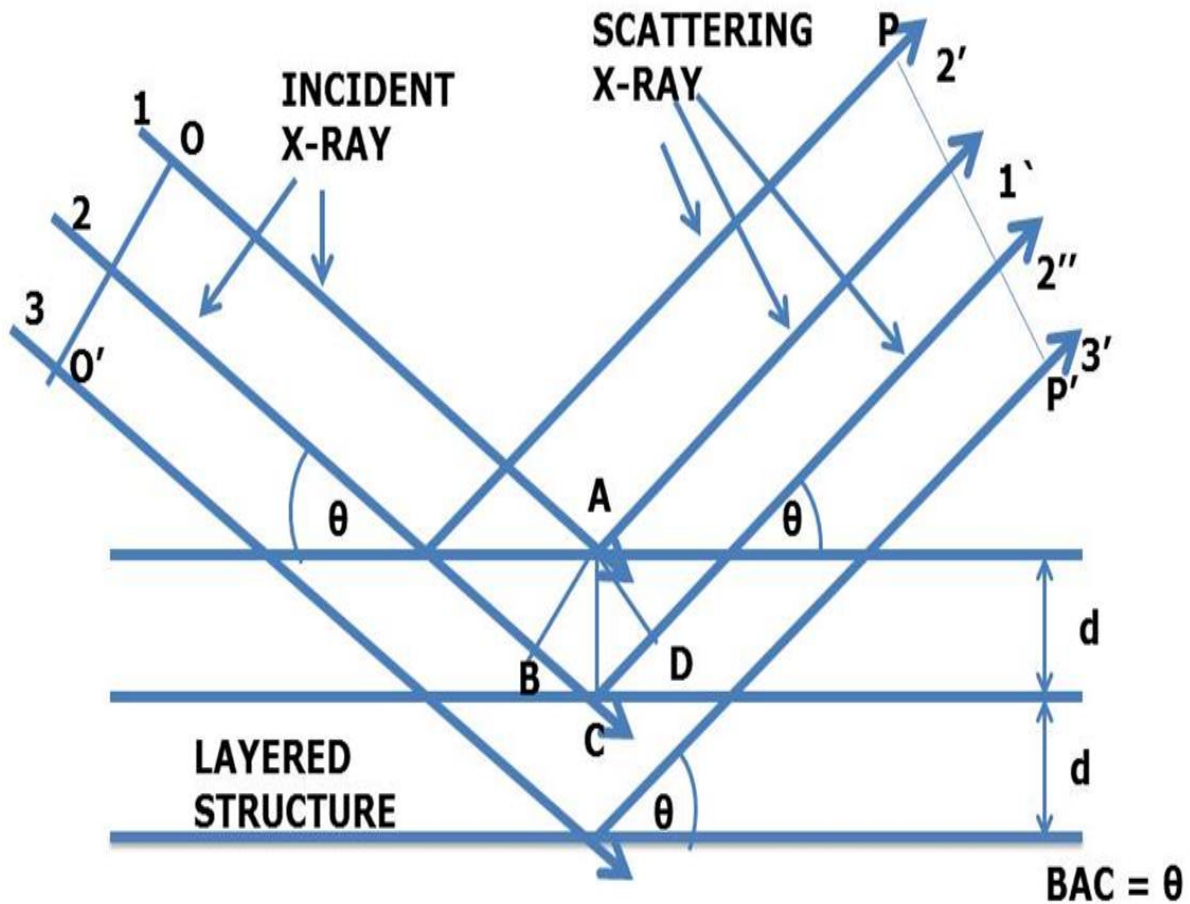


**Figure3. 4** Incident X-Rays are diffracted by the layers of atoms in a crystalline material

**Advantages:**

Accurate characterization of residual stresses in welds has been difficult and often impractical since most residual stress measurement techniques are destructive and lack the resolution to accurately characterize the steep stress gradients that exist in weld HMs. Recently, the measurement of residual stresses using x-ray diffraction techniques has become both practical and efficient. In addition, the introduction of stress mapping techniques has allowed the quick and precise characterization of entire welds, including areas of interest such as steep stress gradients and their associated tensile residual stress maxima. The stress map display has given engineers a complete and accurate visual analysis of the magnitude and distribution of residual stresses in their welded components. Since surface stress measurements using x-ray diffraction techniques are non-contact and non-destructive, measurements can be performed at the same point before and after a process such as post weld heat treating or shot peening, so that residual stresses can be characterized at all steps of the manufacturing process. This can

help in the optimization of these manufacturing processes and the management of their associated residual stresses [11].

### **Limitations:**

XRD also has size limitations. It is much more accurate for measuring large crystalline structures rather than small ones. Small structures that are present only in trace amounts will often go undetected by XRD readings, which can result in skewed results [12]. The grain size of heavy mineral samples from typical heavy mineral dune sand is too large to be analysed directly since the suggested particle size for powder XRD measurements should be less than 10  $\mu\text{m}$  (Brindley 1945)

### **3.3.2 Atomic force microscopy**

The atomic force microscope (AFM) was also invented by Binnig et al. in 1986. While the STM measures the tunnelling current (conducting surface), the AFM measures the forces acting between a fine tip and a sample. The tip is attached to the free end of a cantilever and is brought very close to a surface. Attractive or repulsive forces resulting from interactions between the tip and the surface will cause a positive or negative bending of the cantilever. The bending is detected by means of a laser beam, which is reflected from the back side of the cantilever [13].

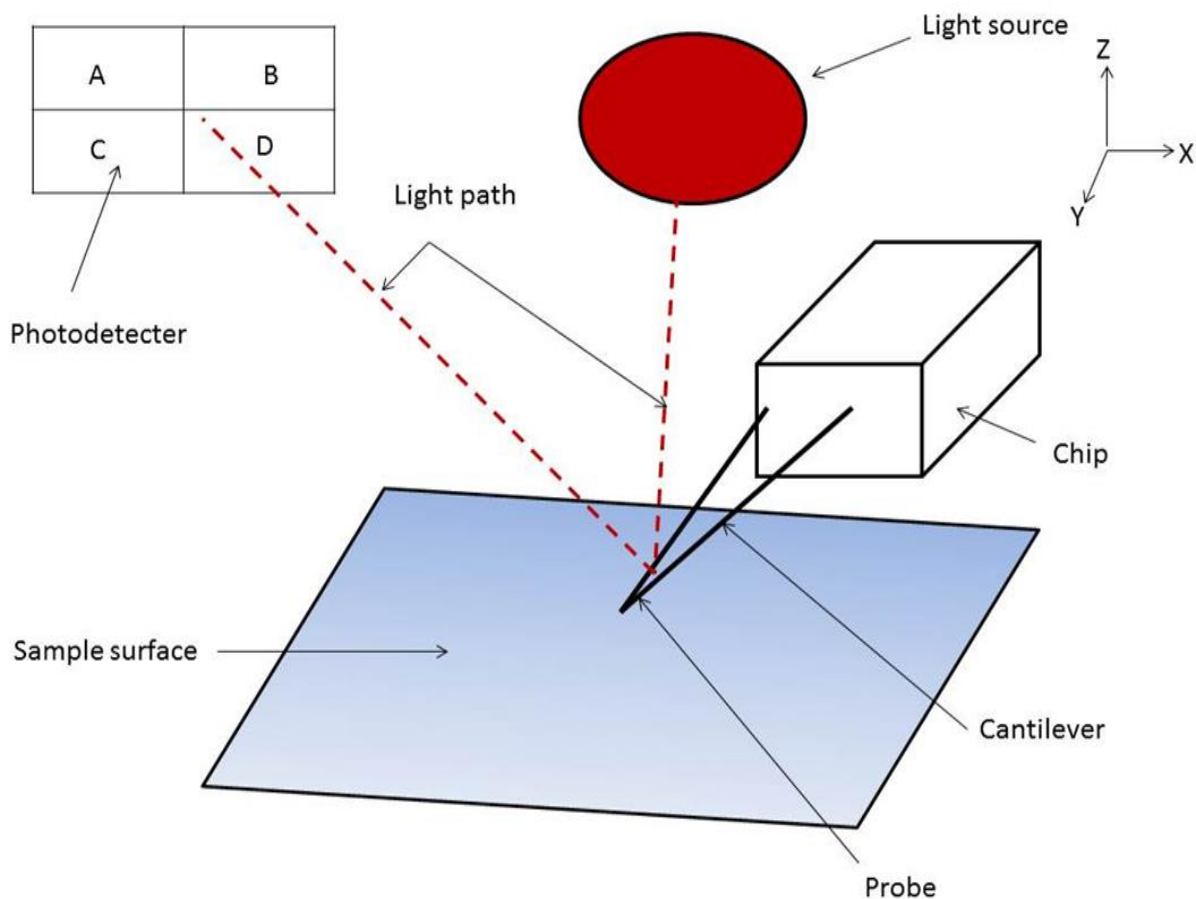


**Figure 3. 5** Basic AFM set-up

The basic set-up of a typical AFM is shown. Cantilevers are commonly either V-shaped, as shown, or rectangular, 'diving board' shaped. The cantilever has at its free end a sharp tip, which acts as the probe of interactions. This probe is most commonly in the form of a square-based pyramid or a cylindrical cone. Commercially manufactured probes and cantilevers are predominantly of silicon nitride (the formula normally given for silicon nitride is  $\text{Si}_3\text{N}_4$ , although the precise stoichiometry may vary depending on the manufacturing process) or silicon (Si). Typically the upper surface of the cantilever, opposite to the tip, is coated with a thin reflective surface, usually of either gold (Au) or aluminium (Al). The probe is brought into and out of contact with the sample surface by the use of a piezocrystal upon which either the cantilever chip or the surface itself is mounted, depending upon the particular system being used (these two configurations are referred to as tip-scanning or surface scanning, respectively). Movement in this direction is conventionally referred to as the z-axis. A beam of laser light is reflected from the reverse (uppermost) side of the cantilever onto a position-sensitive photodetector. Any deflection of the cantilever will produce a change in the position of the laser spot on the photodetector, allowing changes to the deflection to be monitored. The most common configuration for the photodetector is that of a quadrant photodiode

divided into four parts with a horizontal and a vertical dividing line. If each section of the detector is labelled A to D as shown in Figure 4.4, then the deflection signal is calculated by the difference in signal detected by the A + B versus C + D quadrants. Comparison of the signal strength detected by A + C versus B + D will allow detection of lateral or torsional bending of the lever. Once the probe is in contact with the surface, it can then be raster-scanned across the surface to build up relative height information of topographic features of the sample [14].

### **Advantages:**

AFM provides a number of advantages over conventional microscopy techniques. AFMs probe the sample and make measurements in three dimensions, x, y, and z (normal to the sample surface), thus enabling the presentation of three-dimensional images of a sample surface. This provides a great advantage over any microscope available previously. With good samples (clean, with no excessively large surface features), resolution in the x-y plane ranges from 0.1 to 1.0 nm and in the z direction is 0.01 nm (atomic resolution). AFMs require neither a vacuum environment nor any special sample preparation, and they can be used in either an ambient or liquid environment. With these advantages AFM has significantly impacted the fields of materials science, chemistry, biology, physics, and the specialized field of semiconductors [15].

### **Limitations:**

The physical probe used in AFM imaging is not ideally sharp. As a consequence, an AFM image does not reflect the true sample topography, but rather represent the interaction of the probe with the sample surface, this is called tip convolution [16]. It has a single scan image as compared to SEM. The scanning speed is limited. The relative slow rate of scanning during AFM imaging often leads to thermal drift in the image making the AFM microscope less suited for measuring accurate distance between topographical features on the image. Due to the nature of AFM probes, they cannot normally measure steep walls or overhangs [17]. Lateral forces can distort the image. Capillary forces from a fluid layer can cause large forces normal to the tip sample interaction. Combination of these forces reduces spatial resolution and can cause damage to soft samples [18].

### **3.3.3 SCANNING ELECTRON MICROSCOPY**

Scanning electron microscopy (SEM) is a powerful method for the investigation of surface structures of molecules. This technique provides a large depth of field, which means, the area of the sample that can be viewed in focus at the same time is actually quite large [19]. SEM uses a focused beam of electrons, scanning in vacuum the specimen surface, imaging one point at a time. The interaction of the electron beam with every point of the specimen surface is registered, forming the entire image. Since the wavelength of the electron beam is much lower than the wavelength of the visible light, the magnification of SEM is much higher than that of optical microscopes. Electrons in the electron gun are emitted from the cathode and accelerated by the anode to the energy 1-50 keV. The electron beam is condensed by the condenser lenses. Magnetic field, produced by the scan coils deflects the electron beam back and forth. The electron beam, focused by the objective lens to very fine spot (1-5 nm), scans the sample in a raster pattern. Primary electrons interact with the atoms of the sample surface, causing emissions of the secondary electrons, which are detected, producing the image. The back scattered electrons of the electron beam may also be detected. The backscattered electron image is used for contrasting the sample regions, having different chemical composition [20].

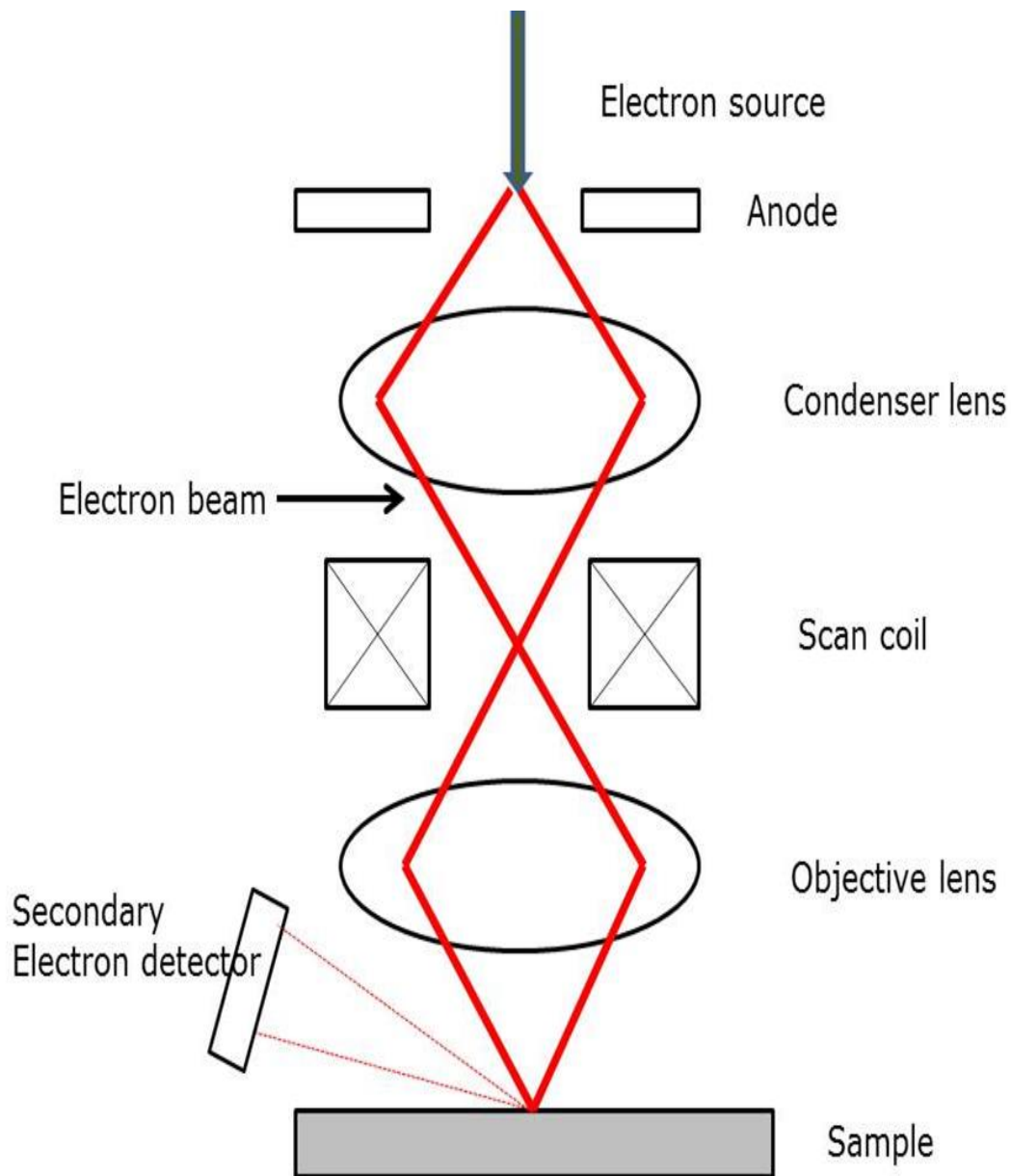


**Figure3. 6** Schematic representation of scanning electron microscopy

**Advantages:**

SEM has also the advantage that the range of magnification is relatively wide allowing the investigator to easily focus in on an area of interest on a specimen that was initially scanned at a lower magnification. Furthermore, the three-dimensional appearing images may be more appealing to the human eye than the two-dimensional images obtained with a transmission electron microscope. Therefore, an investigator may find it easier to interpret SEM images. The number of steps involved for preparing specimens for SEM

investigation is lower and thus the entire process is less time consuming than the preparation of samples for investigation with a transmission electron microscope [19].

### **Limitations:**

SEM specimen preparation harbours various risk factors that can easily distort the integrity and ultrastructure of the mollicutes [19]. This technique utilizes graded solvents (alcohol, acetone, and xylene) to gradually dehydrate the specimen prior to examination, since water of hydration is not compatible with the vacuum used with the electron beam. While any pretreatment can alter specimen morphology, drying appears to significantly alter biofilms due to EPS polymers collapsing. The dehydration process results in significant sample distortion and artifacts; the extracellular polymeric substances, which are approximately 95% water and the liquid loss, led them to appear more like fibers surrounding the cells than like a gelatinous matrix. Several ultrastructural studies have used conventional scanning electron microscopy (SEM) to investigate the glycocalyx, but these studies were hampered by low resolution and also by the inability to use low voltages (<5 keV), which yield increased information from small topographical features. SEM imaging requires a high vacuum,  $\leq 10^{-8}$  Torr, having first been chemically fixed, dehydrated, and coated with a conductive material (e.g. Gold) to prevent charge build-up from the electron beam [21].

### **3.3.4 TRANSMISSION ELECTRON MICROSCOPY**

Transmission electron microscopy (TEM) is a technique where an electron beam interacts and passes through a specimen. The electrons are emitted by a source and are focused and magnified by a system of magnetic lenses. The electron beam is confined by the two condenser lenses which also control the brightness of the beam, passes the condenser aperture and "hits" the sample surface. The electrons that are elastically scattered consist of the transmitted beams, which pass through the objective lens. The objective lens forms the image display and the following apertures, the objective and selected area aperture are used to choose of the elastically scattered electrons that will form the image of the microscope. Finally, the beam goes to the magnifying system that is consisted of three lenses, the first and second intermediate lenses which control the magnification of the image and the projector lens. The formed image is shown either on a fluorescent screen or in monitor or both and is printed on a photographic film.

The operation of TEM requires an ultra-high vacuum and a high voltage. The first step is to find the electron beam, so the lights of the room must be turned off. Through a

sequence of buttons and adjustments of focus and brightness of the beam, we can adjust the settings of the microscope so that by shifting the sample holder find the thin area of the sample. Then tilting of the sample begins by rotating the holder. This is a way to observe as much areas as we can, so we can obtain as much information [13].

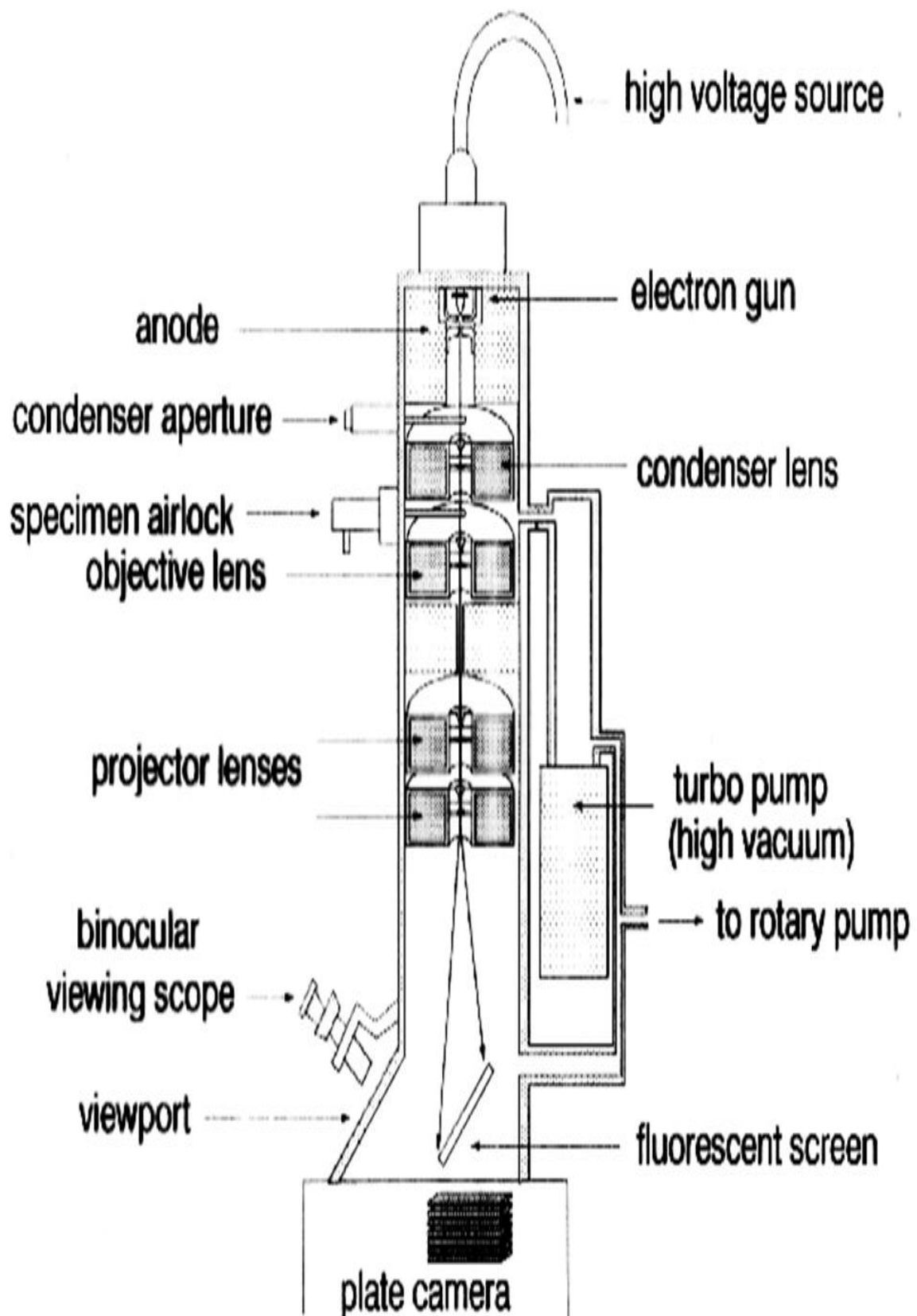


**Figure 3. 7** Schematic representation of transmission electron microscopy

**Advantages:**

TEM has the advantage over SEM that cellular structures of the specimen can be viewed at very high magnifications [19]. The advantage of the transmission electron microscope is that it magnifies specimens to a much higher degree than an optical microscope. Magnification of 10,000 times or more is possible, which allows scientists to see extremely small structures. The transmission electron microscope offers excellent resolution of the crystallographic structure of specimens, and can even show the arrangement of atoms within a sample [22]

**Limitations:**

TEM sample preparation for mollicutes is longer and more difficult than that for SEM and includes additional steps such as post fixation, the embedding of mollicutes in a resin, the sectioning of samples, and the staining of semi-thin and ultrathin sections [19]. The diffraction patterns show dots, regions or circles originating from the sample area illuminated by the electron beam that depend on the material's structure. Monocrystals show distinguished dots in diffraction patterns, polycrystalline materials common centred circles and amorphous materials diffused circles. Distortions and defects are visible in bright and dark field images, but expertise is needed in order to interpret whether they are defects or artifacts. Electron or ion beam damages must be considered in TEM analysis, because of the sensibility of the sample and its really low thickness. Additionally, there's always the problem of calibration and alignment of the instrument. Both of them require experience and skills so the resulting images and data that emerge are reliable and free of objective astigmatism. These works have to be done in order to keep the instrument in excellent working condition [13].

**3.3.5 Rutherford back scattering**

Rutherford Backscattering Spectrometry (RBS) is a widely used nuclear method for the near surface layer analysis of solids. A target is bombarded with ions at an energy in the MeV-range (typically 0.5–4 MeV), and the energy of the backscattered projectiles is recorded with an energy sensitive detector, typically a solid state detector. RBS allows the quantitative determination of the composition of material and depth profiling of individual elements [22]. In RBS a few MeV ion beam is sent towards a sheet of material

and analysing the energy spectrum of the backscattered particles, placing in a chosen direction ( $\theta = 180^\circ$ ) a solid state detector. Therefore it is a nuclear collision based experiment used in material science for in-depth compositional analysis of laterally uniform samples.

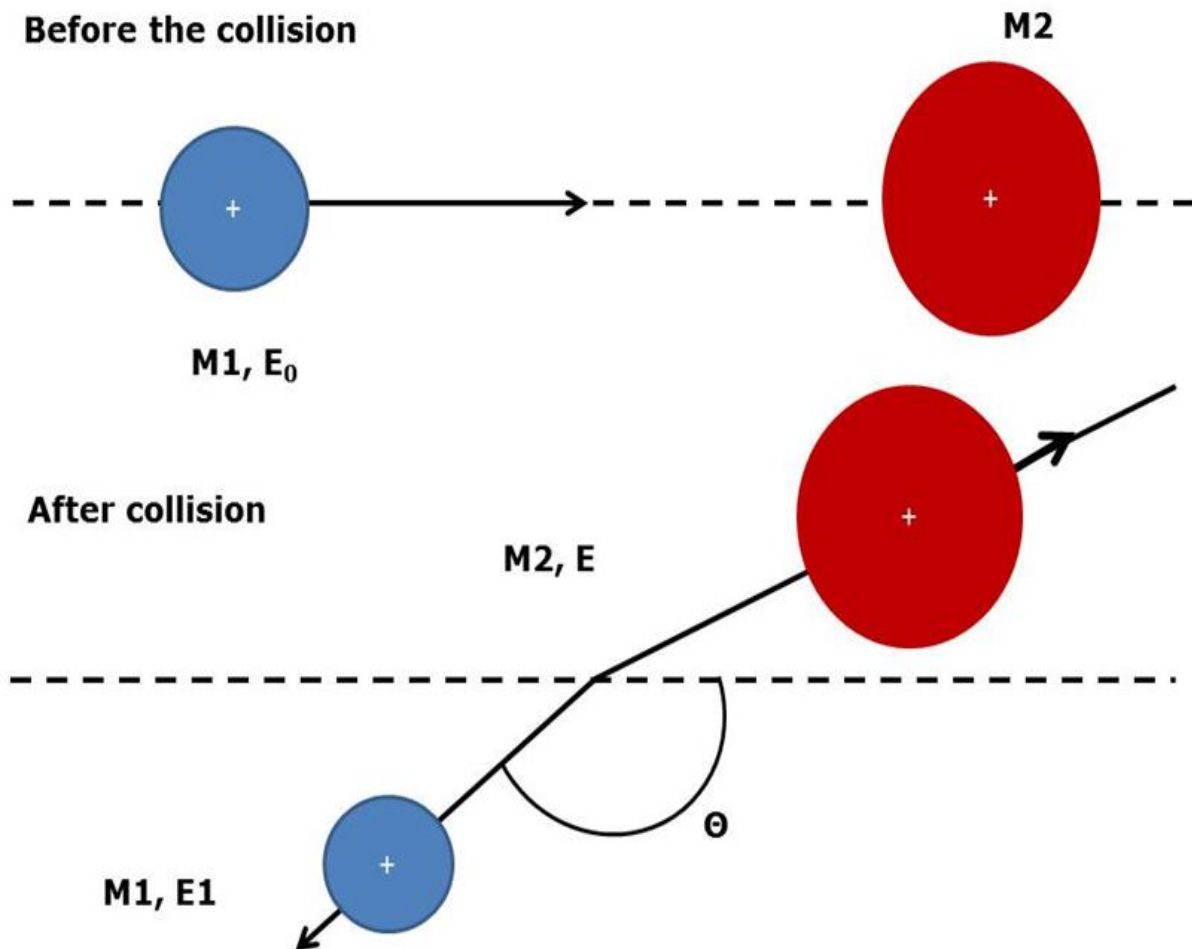


**Figure3. 8** A collision between two positively charged particles before and after the collision. Momentum and energy is conserved [23]

At a basic level, RBS demonstrates the electrostatic repulsion between high energy incident ions and target nuclei. The specimen under study is bombarded with monoenergetic beam of  $^4\text{He}^+$  particles and the backscattered particles are detected by the detector-analysis system which measures the energies of the particles.

During the collision, energy is transferred from the incident particle to the target specimen atoms; the change in energy of the scattered particle depends on the masses of incoming and target atoms. For an incident particle of mass  $M_1$ , the energy is  $E_0$  while

the mass of the target atom is  $M_2$ . After the collision, the residual energy  $E$  of the particle scattered at angle  $\phi$  can be expressed as:

$$E = K^2 E_0 \quad 3.4$$

$$E = k = \frac{(M_1 \cos \phi + \sqrt{M_2^2 - M_1^2 \sin^2 \phi})}{M_1 + M_2} \quad 3.5$$

Where  $k$  is the kinematic scattering factor, which is actually the energy ratio of the particle before and after the collision. Since  $k$  depends on the masses of the incident particle and target atom and the scattering angle, the energy of the scattered particle is also determined by these three parameters. The probability of a scattering event can be described by the differential scattering cross section of a target atom for scattering an incoming particle through the angle  $\phi$  into differential solid angle  $d\Omega$  as follows,

$$\frac{d\sigma_R}{d\phi} = \left( \frac{zZe^2}{2E_0 \sin^2 \phi} \right) \left[ \frac{\cos \phi + \sqrt{1 - \left(\frac{M_1}{M_2} \sin \phi\right)^2}}{\sqrt{1 - \left(\frac{M_1}{M_2} \sin \phi\right)^2}} \right]^2 \quad 3.6$$

Where  $d\sigma_R$  is the effective differential cross section for the scattering of a particle. The above equation may look complicated but it conveys the message that the probability of scattering event can be expressed as a function of scattering cross section which is proportional to the  $zZ$  when a particle with charge  $ze$  approaches the target atom with charge  $Ze$ . Helium ions not scattered at the surface lose energy as they traverse the solid. They lose energy due to interaction with electrons in the target. After collision the He particles lose further energy on their way out to the detector. We need to know two quantities to measure the energy loss, the distance  $\Delta t$  that the particles penetrate into the target and the energy loss  $\Delta E$  in this distance. The rate of energy loss or stopping power is a critical component in backscattering experiments as it determines the depth profile [24].

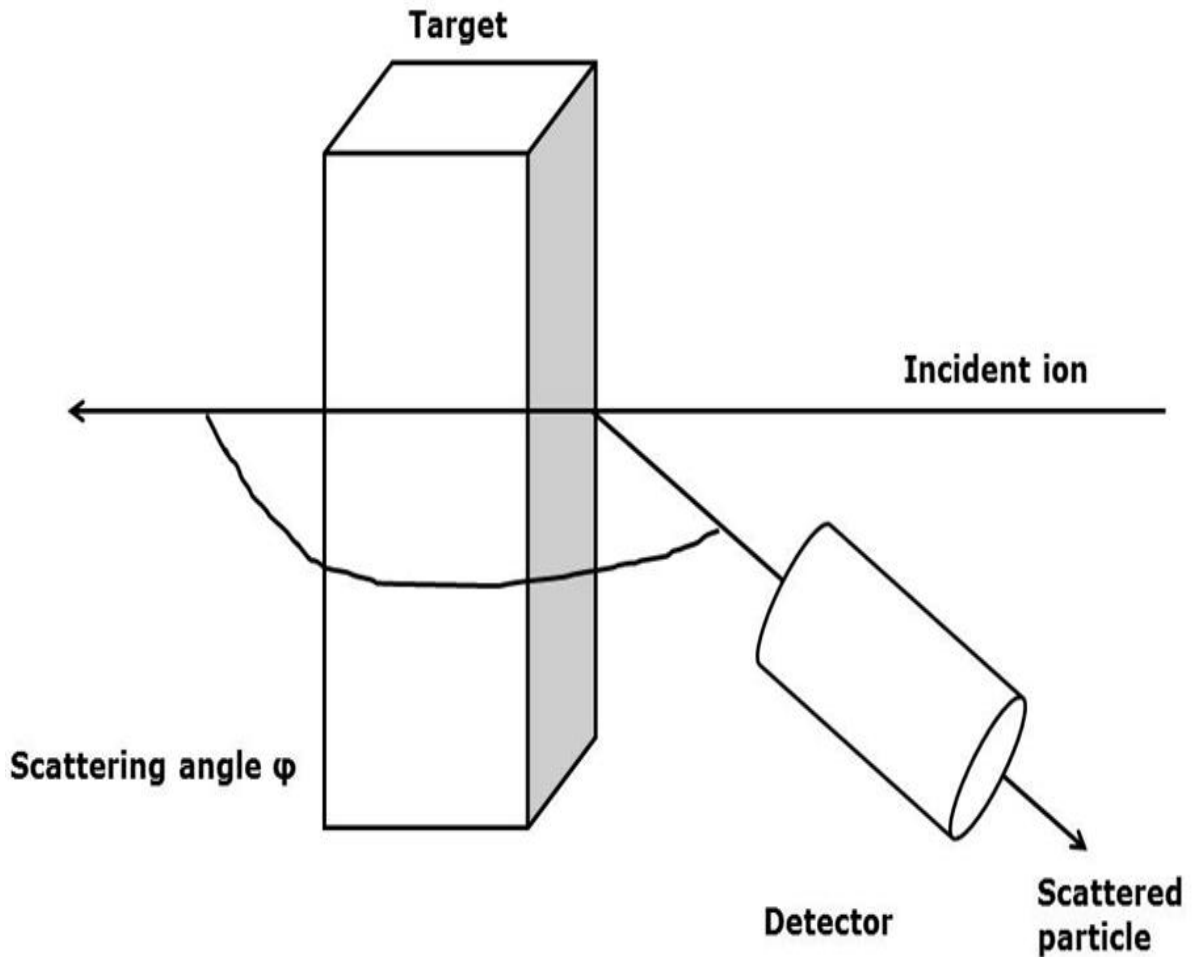


**Figure 3. 9** Schematic representation of the experimental set-up for rutherford backscattering analysis

**Advantages:**

RBS is quantitative without the need for reference samples, non-destructive, has a good depth resolution of the order of several nm, and a very good sensitivity for heavy elements of the order of parts-per-million (ppm). The analysed depth is typically about 2  $\mu\text{m}$  for incident He-ions and about 20  $\mu\text{m}$  for incident protons [25].

**Limitations:**

The drawback of RBS is the low sensitivity for light elements, which often requires the combination of other nuclear based methods like nuclear reaction analysis (NRA) or elastic recoil

detection analysis (ERDA) [25]. RBS does not provide any chemical bonding information which we can get from XPS. The strength of RBS lies in quantitative analysis. However, conventional RBS systems cannot analyse ultrathin films since the depth resolution is only about 10 nm using surface barrier detector [24].

### 3.3.6 Attenuated Total Reflection

Attenuated total reflection (ATR) spectroscopy derives from internal reflection spectroscopy, and it was independently pioneered by Fahrenfort and Harrick in the early 1960's [26]. When light beam propagating through a transparent medium of high index of refraction encounters an interface with a medium of a lower index of refraction, it undergoes total internal reflection for incidence angles greater than the "critical angle". The critical angle  $\theta_c$ , is given by

$$\theta_c = \sin^{-1} (n_2/n_1),$$

where  $n_2$  and  $n_1$  are the refractive indices of the liquid and the solid, respectively. Although the incident light beam totally internally reflects at the interface, an electromagnetic field called the 'evanescent wave' penetrates a small distance into the liquid medium and propagate parallel to the surface in the plane of incidence. The evanescent wave is capable of exciting fluorescent molecules that might be present near the interface. This effect has been regarded as experimental proof of the existence of the evanescent wave.

The evanescent electric field intensity  $I(z)$  decays exponentially with perpendicular distance  $z$  from the interface:

$$I(z) = I_0 e^{-z/d},$$

where

$$d = \frac{\lambda_0}{4\pi} [n_1^2 \sin^2 \theta - n_2^2]^{-1/2}$$

for angles of incidence  $\theta > \theta_c$  and light wavelength in vacuum  $\lambda_0$ . Depth  $d$  is independent of the polarization of the incident light and decreases with increasing  $\theta$ . Except for  $\theta \sim \theta_c$  (where  $d \rightarrow \infty$ ),  $d$  is on the order of  $\lambda_0$  smaller [27].

→

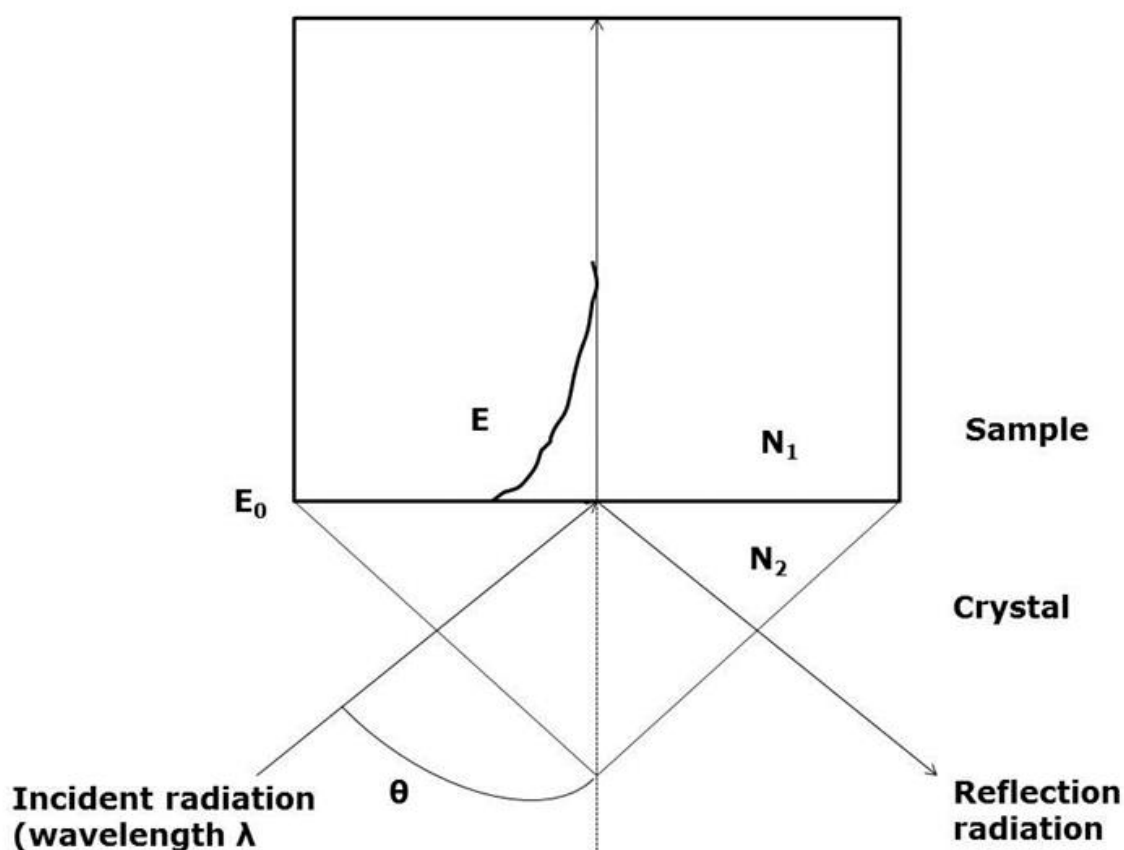


**Figure3. 10** Schematic diagram of the attenuated total reflection of the infrared beam in a monoreflection ATR accessory

### Advantages

Faster sampling with no preparation. Excellent sample-to-sample reproducibility. Minimal operator-induced variations. ATR has advanced to become the standard FT-IR sampling technique, providing excellent data quality combined with high reproducibility. Most samples can be analysed with a diamond ATR-crystal which possesses extreme chemical and mechanical robustness, while Germanium can be used for special purposes, e.g. for measuring highly absorbing samples or thin layers [28].

### Limitations:

The main limitation may arise from the ATR element itself. Each material has a transmission threshold, which may be located at a high wavenumber, such as silicon. Other materials with a low transmission threshold may be too reactive towards solutions. Thus, ZnSe can be attacked by acid or zinc-complexing species. A usual choice made by ATR-elements-

dealers is an element made in ZnSe, but covered by a thin layer of diamond to increase its chemical resistance. This possibility exists only for small ATR crystals, allowing only few reflections of the infrared beam. To increase sensitivity, large ATR crystals are used. Besides the above limitations due to the ATR element, two gases present in the ambient atmosphere lead to absorption bands in IR spectra: carbon dioxide, and water. The main bands consist in a doublet at 2361 and 2339  $\text{cm}^{-1}$  ( $\text{CO}_2$ ), and numerous narrow peaks in the range 2000 – 1300 ( $\text{H}_2\text{O}$  bending) and 4000 – 3400 ( $\text{H}_2\text{O}$  stretching). Generally, the band of  $\text{CO}_2$  does not interfere with bands of adsorbates, but  $\text{H}_2\text{O}$  bending can interfere with adsorbed organic molecules. Several methods exist to solve this problem [29].

### **3.3.7 Raman spectroscopy**

Raman spectroscopy is a powerful tool to get complementary information to IR spectroscopy. Raman spectroscopy is based on Raman scattering. Scattering of electromagnetic radiation occurs, because the oscillating electric field of the radiation induces oscillation of electrons in a molecule, which in turn emits electromagnetic radiation. Unlike elastic Rayleigh scattering which is used to determine the shape and weight of macromolecules, Raman scattering is inelastic scattering. Approximately 1 in  $10^7$  scattered photons has a different energy than the incoming photons. This energy is neither created nor lost completely: the energy difference is equal to the energy of a transition, the molecules undergoes in response to the collision with the photon [30].

A typical Raman system consists of the following basic components: (1) an excitation source, usually a laser; (2) optics for sample illumination; (3) A double or triple monochromator; and (4) a signal processing system consisting of a detector, an amplifier, and an output device. A number of stages are involved in the acquisition of Raman spectrum. A sample is mounted in the sample chamber and a laser light is focused on it with the help of a lens. Generally, liquids and solids are samples in a Pyrex capillary tube. The scattered light is collected using another lens and is focused at the entrance slit of the monochromator. Monochromator slit width are set for desired spectrum resolution. The monochromator effectively rejects stray light and serves as a dispersing element for incoming radiation. The light leaving the exit slit of the monochromator is collected and focused on the surface of a detector. This optical signal is converted to an electrical signal within the detector, and further manipulate using detector electronics. Such a signal is stored in computer memory for each predetermined frequency interval. In a conventional Raman system a photomultiplier tube (PMT) detector, light intensity at various frequencies is measured by scanning the

monochromator. A plot of signal intensity against wavelength constitutes its Raman spectrum [31].

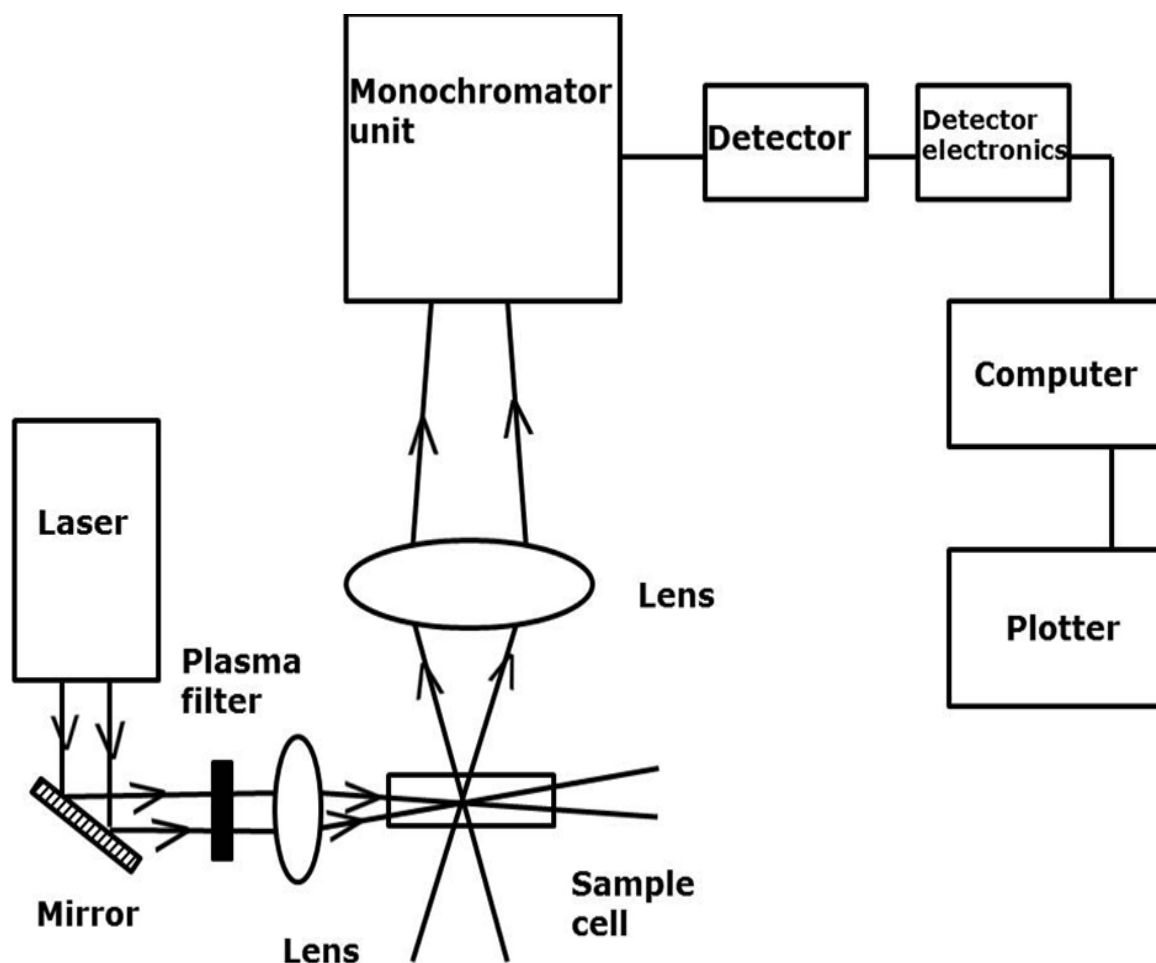


**Figure 3. 11** Schematic of Laser Raman system

When light interacts with matter, the photons which make up light may be absorbed or scattered, or may not interact with the material and may pass straight through it. If the energy of an incident photon corresponds to the energy gap between the ground state of a molecule and an excited state, the photon may be absorbed and the molecule promoted to the higher energy excited state. It is this change which is measured in absorption spectroscopy by the detection of the loss of that energy of radiation from the light. However, it is also possible for the photon to interact with the molecules and scatter from it. In this case there is no need for the photon to have an energy which matches the difference between two energy levels of the molecules. The scattered photon can be observed by collecting light at an angle to the incident light beam, and provided there is no absorption from any electronic transitions which have similar energies to that of the incident light, the efficiency increases as the fourth power of the frequency of the incident light [32].

### **Advantages:**

Raman has small sample size requirements, minimal sample preparation, and the lack of chemical or mechanical pre-treatment [33]. Raman spectra can be obtained non-invasively, the bulk and final product can be tested directly in their packaging. It can be used to study small particles within inhomogeneous sample matrices. Since water is a weak Raman scatterer, it possible to analyse aqueous solution by Raman spectroscopy [34].

### **Limitations:**

- (i) The laser heating could lead to loss of hydration water, phase transition, partial reduction and, thus, to artificially change samples. This can be reduced by applying low laser powers ( $< 10 \text{ mW}$ ), cooling with inert gas of high thermal conductivity or focusing lens techniques, which decrease the energy flux.
- (ii) Fluorescence can overwhelm the Raman spectrum, which can be due to organic impurities, basic surface of OH groups, proton superpolarizability. This can be solved by burning the organic contaminants.
- (iii) The Raman scattering has an inherently low sensitivity due to the small Raman scattering cross-sections as compared to IR absorption coefficient. The low sensitivity can be improved by increasing the excitation frequency due to the  $\nu^4$  law [35].

### **1.2.1 X-ray Photoelectron Spectroscopy**

X-ray photoelectron spectroscopy (XPS) is one of the most widely used surface analytical techniques.

XPS principle:

The surface to be analysed is irradiated with soft X-ray photons. When a photon of energy  $h\nu$  interact with an electron in a level with binding energy  $E_B$ , the entire photon energy is transferred to the electron, with the results that a photoelectron is ejected with kinetic energy

$$E_{\text{kin}} = h\nu - E_B - \Phi_s \quad 1.1$$

Where  $\Phi_s$  is a small, almost constant, work function term

$h\nu$  must be greater than  $E_B$ . The ejected electron may come from a core level or from the occupied portion of the valence band, in XPS most attention is focused on the electrons in core level. Since no two elements share the same set of electronic binding energies, measurements of the photoelectronic kinetic energies enables elemental analysis. Equation 1.1 indicate that any change in EB are reflected in  $E_{kin}$ , which means that changes in the chemical environment of an atom can be followed by monitoring changes in the photoelectron energies, leading to the provision of chemical information. In principle, XPS can be used to analyse all elements in a periodic Table; however, in general, hydrogen and helium cannot be detected due to the low cross-section of interaction [36].

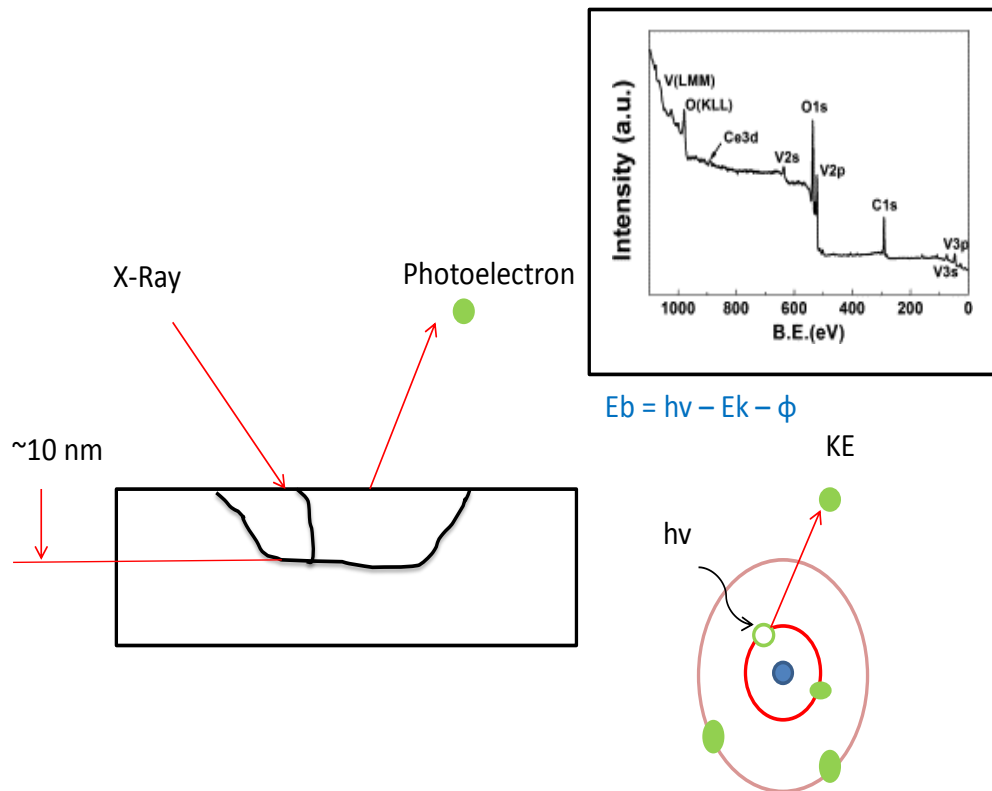


**Figure 3. 12** Schematic diagram of Principle of XPS

Instrumentation:

The basic components of an XPS spectrometer include an X-ray source, electron energy analyzer, and detection system as seen in figure 3.16. Within the XPS spectrometer, the

emitted photo-electrons need to travel a considerable distance before they reach a detector. To ensure that energy losses due to collisions with gas molecules are kept to a minimum, XPS spectrometer need to operate under ultra-high vacuum conditions, typically  $1 \times 10^{-7}$  mbar ( $7.5 \times 10^{-8}$  torr) or better. Any solid sample that is compatible with these conditions can be analysed and requires little or no prior sample preparations [37]

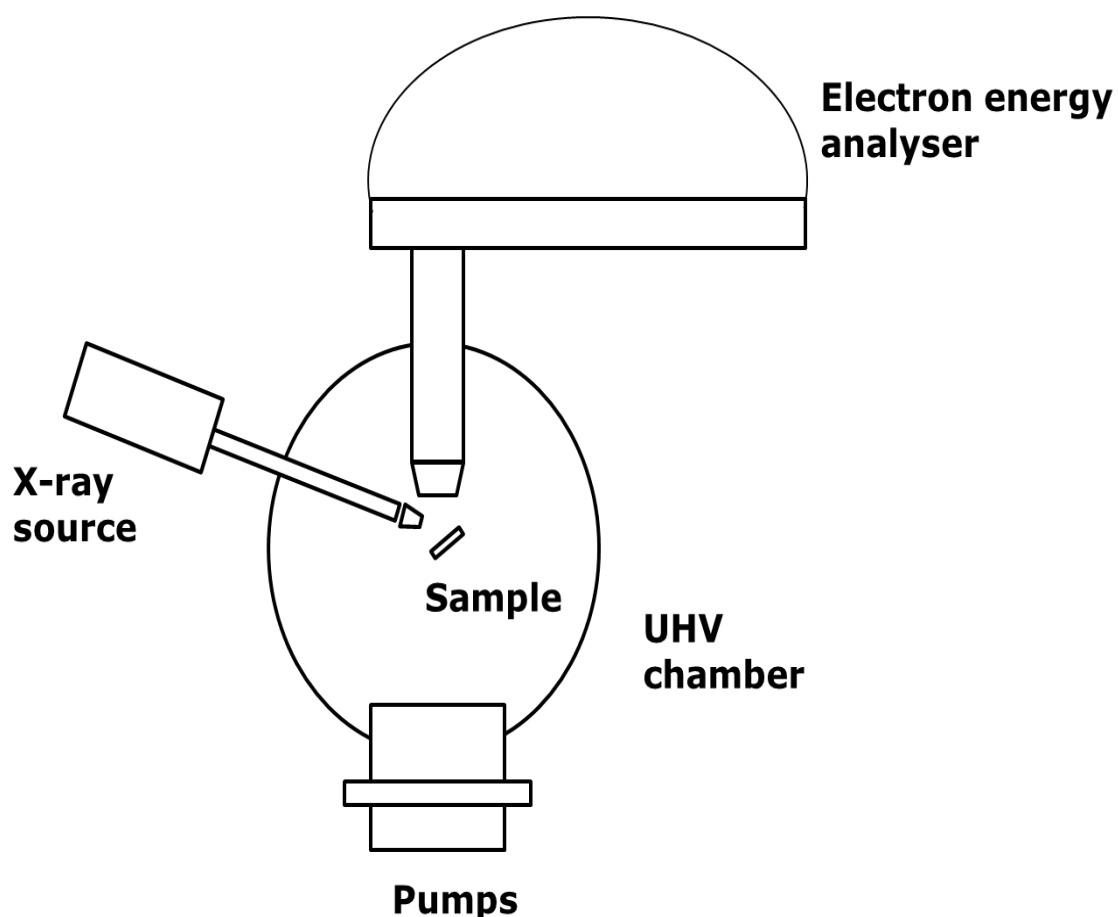


**Figure3. 13** Schematic representation of XPS components

**Advantages:**

XPS techniques are good surface sensitivity, straightforward elemental and chemical state analysis and reliable quantification of the data. XPS is non-destructive and can be used for metal-, ceramics- or polymers- samples. However the samples must be solid and vacuum compatible. It is relatively straightforward quantitative method for elemental composition. Sampling depth in XPS is typically  $\sim 10 - 100 \text{ \AA}$ . There is extensive database of chemical shift information.

**Limitations:**

The most serious limitation is the ex-situ nature of the technique. The instrument is very costly and complex and the monochromatic X-ray sources have low flux. XPS is not usually spatially sensitive, sampling depth varies with electron kinetic energy and the spectrum is complicated by secondary features like X-ray satellite [38].

### 3.4 References

- [1] T. Lippert and C.W. Schneider, *Thin Film Deposition of Functional Materials by Pulsed Laser Deposition*, <http://www.azom.com/article.aspx?ArticleID=5986>
- [2] The Principles of Pulsed Laser Deposition (PLD),  
<http://titan.physx.u-szeged.hu/~lamilab/plden.htm>
- [3] E. Morintale C. Constantinescu, M. Dinescu, *Physics AUC*, Vol. 20 (Part 1), 43-56 (2010)
- [4] Hans-Ulrich Krebs, Martin Weisheit, Jorg Faupel, Erik Suske, Thorsten Scharf, Christian Fuhse, Michael Stormer, Kai Sturm, Michael Seibt, Harald Kijewski, Dorit Nelke, Elena Panchenko, and Michael Buback, *PLD - a versatile thin film technique*
- [5] Dr Sergey Fedoseev, *Fundamentals of Pulsed Laser Deposition* (2009)
- [6] P. R. Willmott and J. R. Huber, *Reviews of Modern Physics*, Vol. 72, No. 1, (2000)
- [7] F. Hinterberger, *Electrostatic accelerators*
- [8] *Radiation chemistry and Nuclear Chemistry*, Particle Accelerators, Chapter 13, 356-365
- [9] R. Guinebretière, *X-ray Diffraction by Polycrystalline Materials*. Chapter 1, P 3, (2007)
- [10] Guozhang Cao, *NANO structures and NANO materials*, imperial college press, p331-333, 2004
- [11] James A. Pineault & Michael E. Brauss, *Residual Stress Characterization of Welds Using X-Ray Diffraction Techniques*
- [12] Steve Johnson, *Advantages & Disadvantages of XRD and XRF*,  
[http://www.ehow.com/list\\_6054766\\_advantages-disadvantages-xrd-xrf.html](http://www.ehow.com/list_6054766_advantages-disadvantages-xrd-xrf.html)
- [13] Arantxa Vilalta-Clemente and Kathrin Gloystein, *Physics of Advanced Materials Winter School*, 2008
- [14] Daniel Johnson, Nidal Hilal and W. Richard Bowen, *Basic Principles of Atomic Force Microscopy*, Chapter 1, 1-30

- [15] Cheryl R. Blanchard, *the chemical educator*, vol. 1, no. 5, 1996
- [16] Robert A. Wilson and Heather A. Bullen, *Introduction to Scanning Probe Microscopy (SPM)*, Basic Theory Atomic Force Microscopy (AFM)
- [17] lifeshouldgoon, *Advantages and disadvantages of atomic force microscopy*,  
machinemakers.typepad.com, (2011)
- [18] Bharat P. V. Syam Sandeep P. ME-MECH, *Materials and Structure Property Correlation*, Atomic Force Microscopy (AFM)
- [19] C. T. K.-H. Stadtländer, *Modern Research and Educational Topics in Microscopy*, 2007
- [20] Dr. Dmitri Kopeliovich, *Scanning Electron Microscope*,  
[http://www.substech.com/dokuwiki/doku.php?id=scanning\\_electron\\_microscope](http://www.substech.com/dokuwiki/doku.php?id=scanning_electron_microscope)
- [21] Soumya El Abed, Saad Koraichi Ibnsouda, Hassan Latrache and Fatima Hamadi, *Scanning Electron Microscopy (SEM) and Environmental SEM: Suitable Tools for Study of Adhesion Stage and Biofilm Formation*, Scanning Electron Microscopy, Dr. Viacheslav Kazmiruk (Ed.), 717-730, 2012
- [22] Karen S. Garvin, eHow contributor, viewed 2 feb 2012,  
[http://www.ehow.com/list\\_6309088\\_advantages-transmission-electron-microscope\\_.html](http://www.ehow.com/list_6309088_advantages-transmission-electron-microscope_.html)
- [23] M. Mayer, *Rutherford Backscattering Spectrometry (RBS)*, p 59-70
- [24] Anders Hallén, *Brief introduction to Rutherford Backscattering Spectrometry*, 2012
- [25] M. Mayer, *Rutherford Backscattering Spectrometry (RBS)*, Max-Planck-Institut für Plasmaphysik, EURATOM Association, Garching, Germany, (2003)
- [26] Liqun Wang, *infrared attenuated total reflection spectroscopy for monitoring biological Systems*, PhD thesis, Department of Chemistry, Georgia Institute of Technology (2009)
- [27] Axelrod, Burghardt & Thompson, *Ann. Rev. Biophys. Bioeng*, 13: 247-48, (1984)
- [28] AZOM, *Attenuated Total Reflection (ATR) Mode - Advantages for FT-IR Spectroscopy*,

- <http://www.azom.com/article.aspx?ArticleID=5958>, (2012)
- [29] Lefèvre Grégory, Preočanin Tajana, Lützenkirchen Johannes, *Infrared Spectroscopy*, Theophile Theophanides (Ed.), (2012)
- [30] Franziska Hofmann, Stephan Steinmann, *Raman Spectroscopy*, (2007)
- [31] R.H. Atalla, U.P. Agarwal, AND J.S. Bond, Methods in Lignin Chemistry, S.Y. Lin and C.W. Dence (eds.), *Raman Spectroscopy*, New York: Springer-Verlag: 162-176; (1992)
- [32] Ewen Smith and Geoffrey Dent, *Modern Raman Spectroscopy – A Practical Approach*, John Wiley & Sons Ltd, (2005)
- [33] Irina Geiman, Marco Leona, and John R. Lombardi, *J Forensic Sci*, Vol. 54, No. 4, (2009)
- [34] Rakesh R. Somani et al, *Der Chemica Sinica*, 1 (1): 1-12, (2010)
- [35] G. Mestl/ *Journal of Molecular Catalysis A: Chemical* 158, 45–65, (2000)
- [36] Henning Bubert , John C. Rivière , and Wolfgang S.M. Werner, *X - Ray Photoelectron Spectroscopy (XPS), Surface and Thin Film Analysis: A Compendium of Principles, Instrumentation and Applications, Second Edition*, 7-34, 2011.
- [37] Tim Nunney and Richard White, *X-ray Photoelectron Spectroscopy*, 22- 28, (2011)
- [38] H. R. Verma, *Atomic and Nuclear Analytical Methods: XRF, Mössbauer, XPS, NAA and Ion-Beam*, 241, 2007

# Chapter 4

## Results and Discussions

### 4.1 film micro-structure study

Figure 4.1 shows a typical X-ray diffraction (XRD) pattern of polycrystalline structure of the monoclinic (M) phase VO<sub>2</sub> deposited on Mica substrate. The XRD was carried out using a BRUKER AXS D8 Advance X-ray Diffractometer with Cu-K<sub>α</sub> radiation with wavelength,  $\lambda (K_{\alpha 1}) = 1.5406 \text{ \AA}$ . The X-ray tube was powered with a current of 40 mA and a voltage of 40 kV, the XRD patterns show diffraction peaks due to VO<sub>2</sub> thin film, these diffraction peaks at  $2\theta = 27.8^\circ, 37.4^\circ, 44.1^\circ, 57.2^\circ$  and  $88.2^\circ$  correspond to these diffracting planes (0 1 1), ( $\bar{2}$  1 1), (1 2 0), (0 2 2) and (3 0 0) respectively of monoclinic VO<sub>2</sub>. Peng He et al. prepared VO<sub>2</sub> on mica using sol-gel method. They achieved the VO<sub>2</sub> along the (011) and ( $\bar{2}11$ ) orientation, which is in consistence with this current work [1].

All the reflections of all the samples are the similar with the intensity of (330) peak decreasing with increasing deposition time. According to the calculated pattern description of the hexagonal structure of the mineral name of Zinnwaldite 3 T (mica) (JCPDS No: 79-1668), all others reflections seen in figure 4.1, correspond to the mica Substrate. It should be noted that although the multiple valence states of vanadium ions lead to several vanadium oxide phases such as Magneli phases (V<sub>n</sub>O<sub>2n-1</sub>) and Wadsley phases (V<sub>2n</sub>O<sub>5n-2</sub>), no other peak corresponding to any other vanadium oxide phases mentioned is present in the XRD spectra, indicating the exclusive formation of single-phase VO<sub>2</sub> films on Mica substrate.

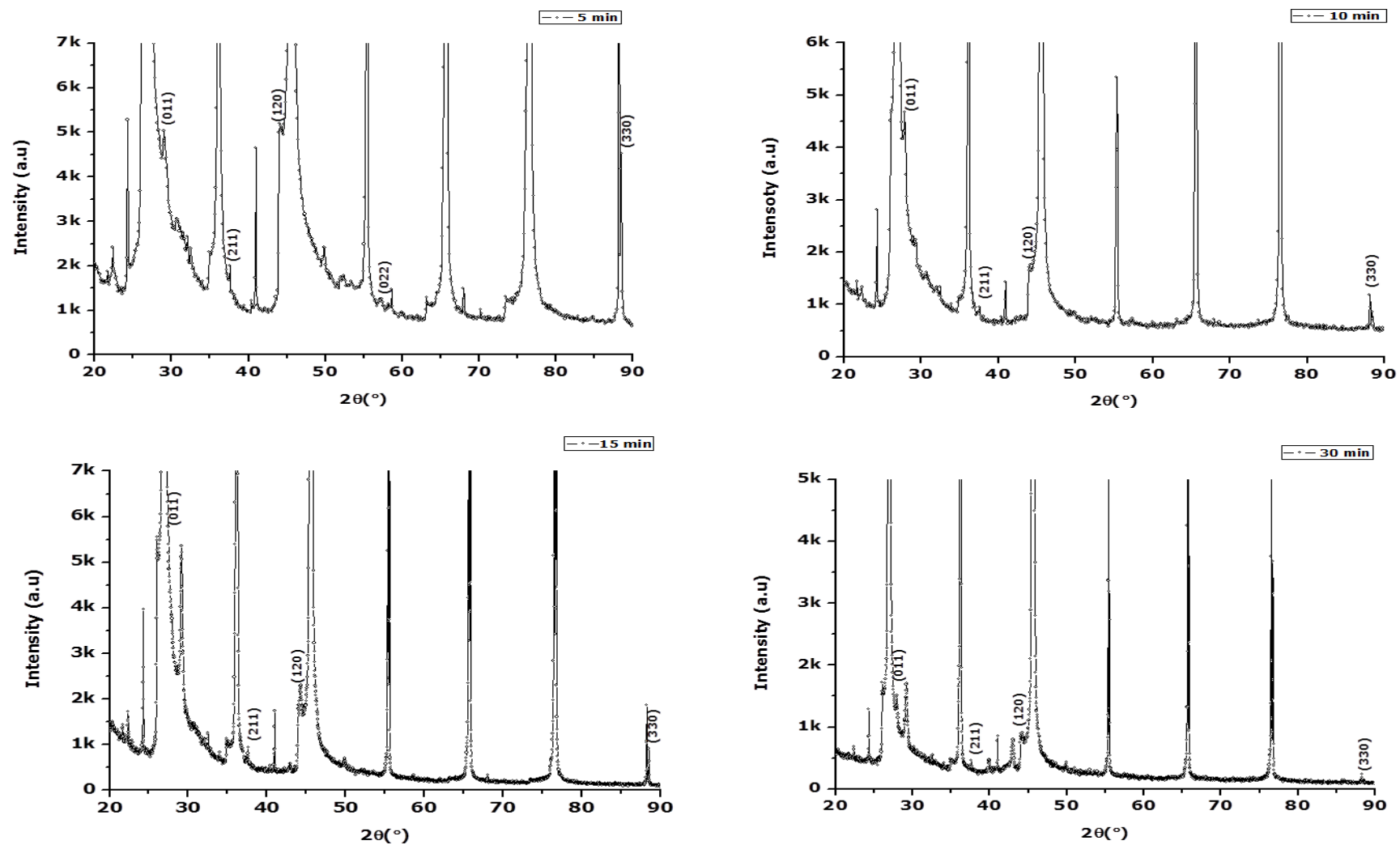


**Figure 4. 1** X-ray diffraction pattern of VO<sub>2</sub> deposited on mica by PLD for (a) 5 min, (b) 10 min, (15) min, (d) 30 min

## 4.2 High Resolution transmission electron microscopy (HRTEM)

Further structural characterization of the VO<sub>2</sub> films were performed using High-resolution transmission electron microscopy (HRTEM). Fig. 4.2(a) presents the TEM image obtained by directing the electron beam perpendicular of the film. HRTEM images were taken from the film at room temperature and also at high temperature about 100°C. Fig. 4.2(b) shows a very polycrystalline structure with clear lattice fringes. Fig.4.2.1(c) shows the electron diffraction spotted ring pattern of VO<sub>2</sub> at room temperature (monoclinic phase) indicating the development of regions of localized crystallinity.

The interplanar spacing is calculated to be 0.30 nm using the formula  $d = \frac{\lambda L}{R}$ , where  $\lambda$  is the wavelength of an electron, L is the camera length in cm and R is the distance from the central bright spot to one of the ring, this value is in agreement with the d spacing of (011) plane of monoclinic VO<sub>2</sub>. A phase transition between monoclinic and tetragonal VO<sub>2</sub> phase showing a reversible transition would be crucial for achieving abrupt changes in electrical and optical properties [2]. For this reason, we characterised the structural reversible phase transition of crystalline VO<sub>2</sub> film using TEM. Fig 4.2.1(d) shows the tetragonal spotted ring diffraction pattern of VO<sub>2</sub> at high temperature of about 100°C. With more ring being formed, the interplana spacing is calculated to be 3.04 nm, which is in agreement with the d spacing of (110) of tetragonal VO<sub>2</sub>. It is noted from the fig 4.2.1 (c) and (d) that the (011) in a monoclinic structure correspond to that of (110) in a tetragonal structure. This demonstrates that the phase transition from monoclinic to a tetragonal has occurred during heating. After the sample was cooled to room temperature, the same convergent beam pattern as shown in figure 4.2c appeared again.

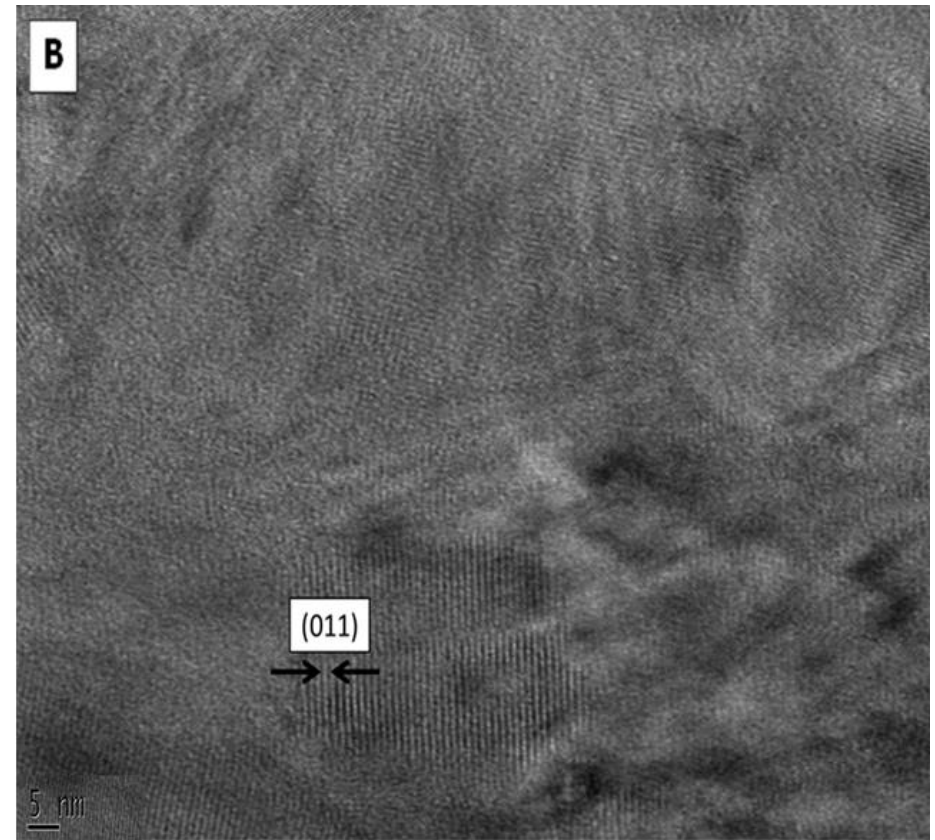
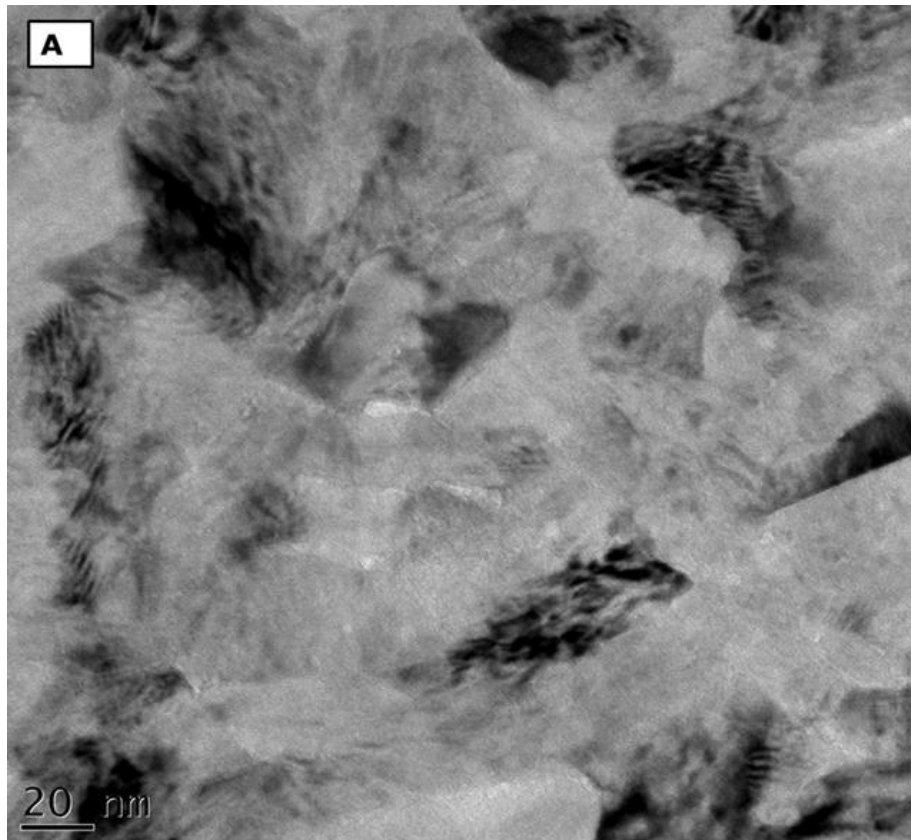


**Figure 4. 2** shows (a) HRTEM images of VO<sub>2</sub> on mica, (b) clear lattice fringes of VO<sub>2</sub> on mica

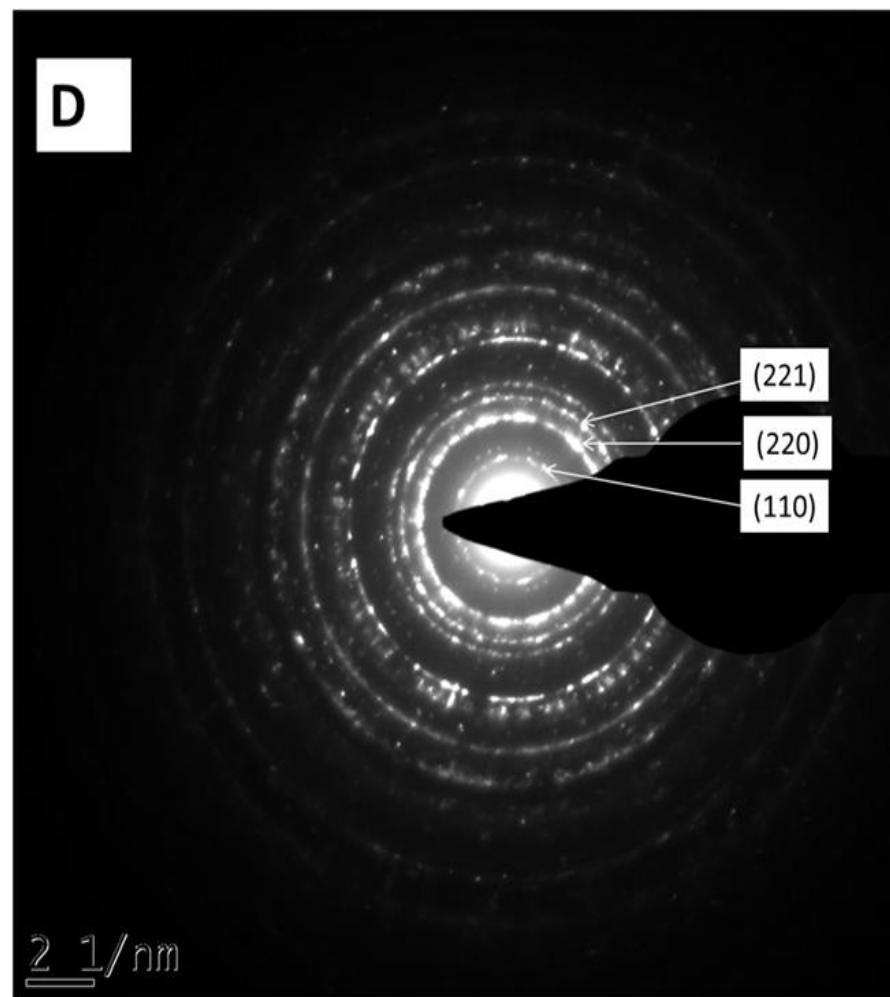
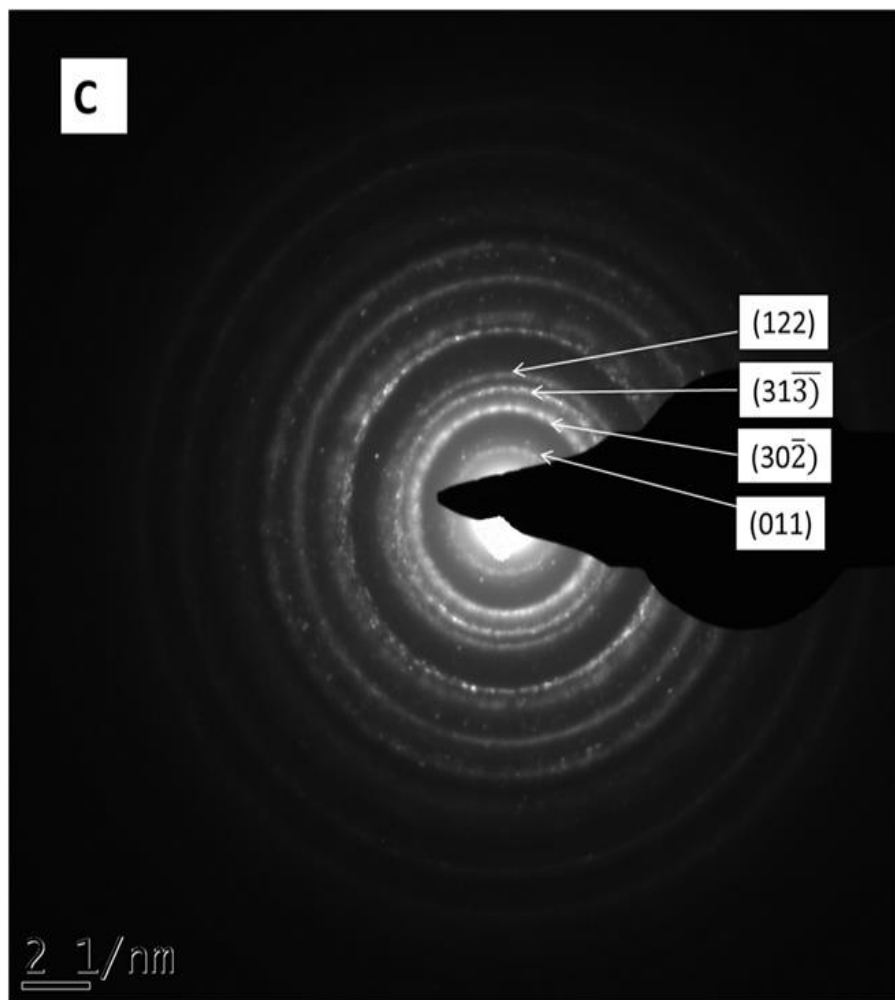


**Figure 4.2** 1 shows electron diffraction spotted ring pattern of (c) VO<sub>2</sub> at room Temperature, (d) VO<sub>2</sub> at high temperature above 100°C

### 4.3 Rutherford backscattering spectroscopy results

Rutherford backscattering spectroscopy (RBS) has been used to determine the film thickness by using XRUMP simulation software. Alpha particles with incident energy of 2 MeV were used and the tilted angle was  $-10^\circ$ . Using various deposition times, variable film thickness measured from RBS were obtained in a range 10 -348 nm with an error of about 5%. A linear correlation was obtained between time of deposition and film thickness. It is hard to evaluate the oxygen concentration of the film for a couple of reasons. The oxygen signal overlaps the mica signal, and it is difficult to separate ion scattering contribution from oxygen on the film and in the substrate (Raman et al) [3]. Fig4.3 Shows the plot of simulated spectra where the thickness were obtained. The estimated values are tabulated in table 4.1 as well as the deposition rate, which is somehow constant because the deposition conditions for all the samples were the same. It can be seen in that the simulated curve (Red line) calculated using the experimental parameters for a film of 10 nm thickness using the bulk target composition is in good agreement with this experimental RBS spectrum. This observation indicates that the film had a stoichiometric VO<sub>2</sub> composition over thickness of 10 nm and the rest. The element composition abundances for all the elements present in both the films and the substrate were found to be very closely the same and with a Vanadium/Oxygen atomic abundance ratio of 2:1 for all specimen, in good agreement with the EDS results figure 4.5.

**Table 4.1** the estimated values of film thickness from XRUMP simulation.

Time of Deposition	Film thickness (nm)	Deposition Rate (nm/sec)
50 sec	10.0	0.2
5 min	34.8	0.1
10 min	138.6	0.2
15 min	154.9	0.2
30 min	348.1	0.1

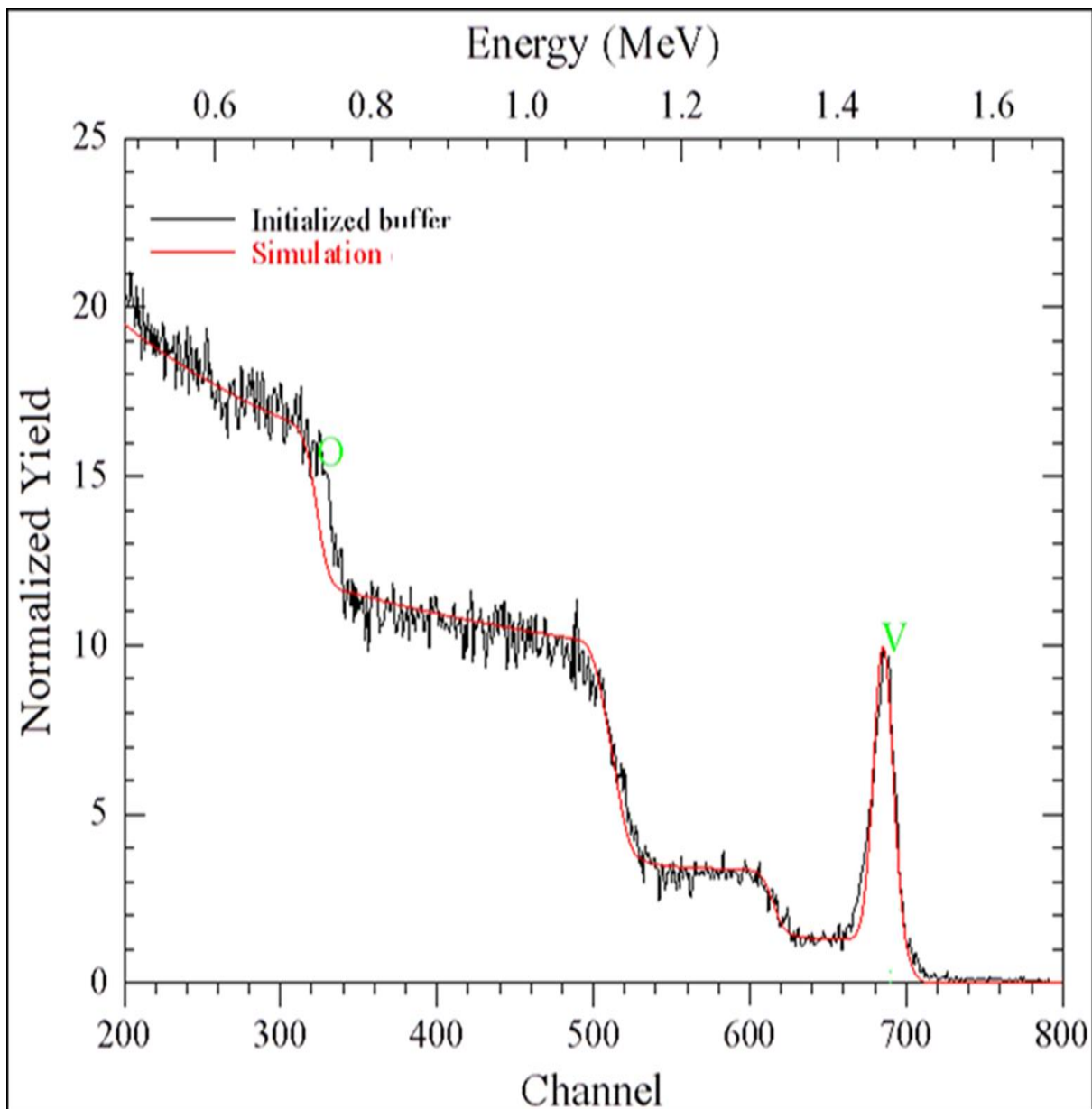


**Figure4. 3** RBS spectrum of  $\text{VO}_2$  deposited on mica by PLD. The solid red line is the corresponding fitting using XRUMP

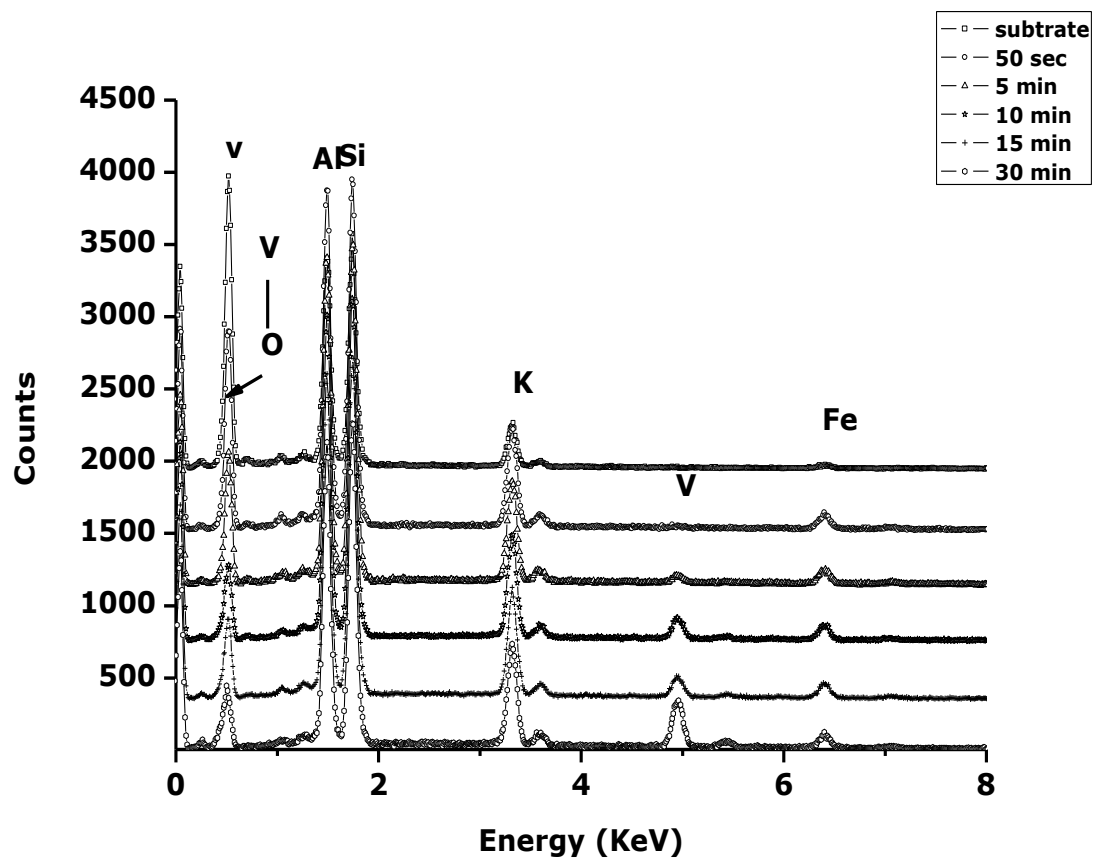


**Figure4. 4** EDS spectrum of  $VO_2$  deposited on mica

#### **4.4 Film surface Topography**

The film topology was investigated using Atomic Force Microscopy (AFM) and analysed using the Nanoscope software to get the roughness of the films surface. The topography of the films was taken at room temperature, meaning that it was taken at the semiconducting phase. AFM analysis shows that the film surface becomes increasingly rough as the film thickness increases. The roughness ranges from 3.14 nm to 17.29 nm. The difference in roughness is due to difference in grain size which is caused by difference in deposition time. For the film in figure 4.5 (a), the height is almost the same for all the grains, resulting in roughness of 3.14 nm. For the film in figure 4.4 (e), the grains are larger and have different heights, resulting in an abrupt increase of roughness of 17.29 nm. The roughness has effect on the carrier density of the material, the thicker the film the more carrier density. Fig 4.6 shows the graph of film thickness versus the roughness of the films. The graph shows an increase in roughness with increasing time of deposition.

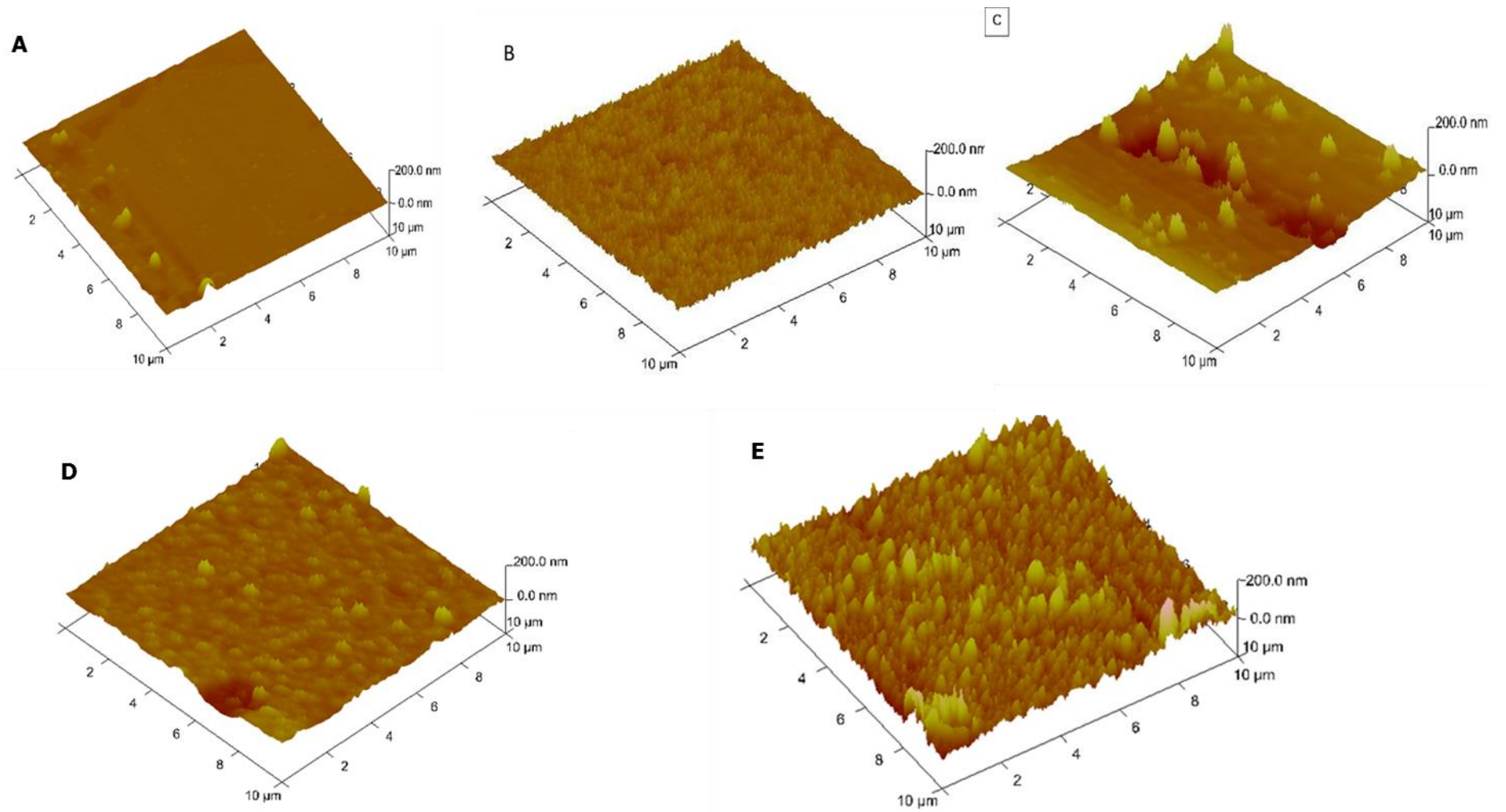


**Figure 4. 5** shows the AFM scan of  $\text{VO}_2$  on mica deposited for (a) 50 sec, (b) 5 min, (c) 10 min, (d) 15 min, and (e) 30 min

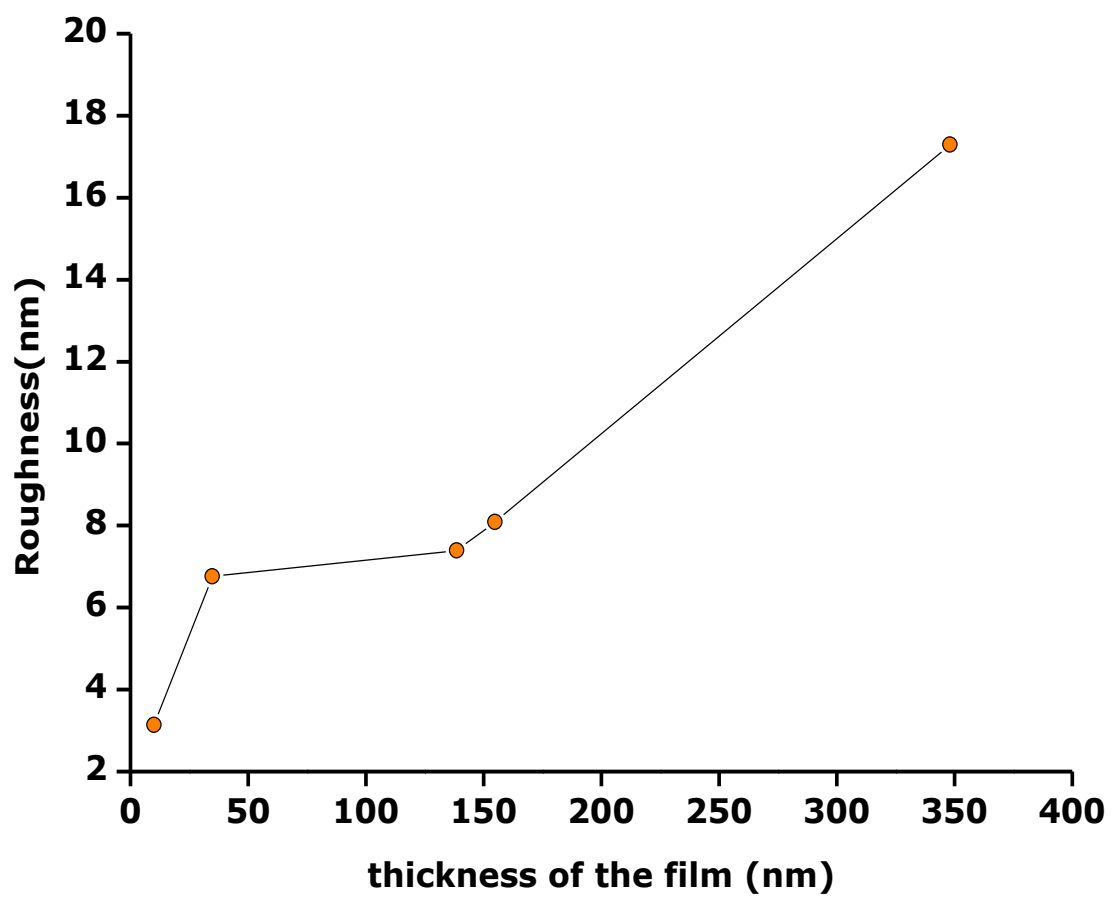


**Figure4. 6** Graph of thickness v/s roughness of VO<sub>2</sub> on mica

## 4.5 surface morphology

Figure 4.6 shows the Scanning electron microscopy (SEM) images of VO<sub>2</sub> film deposited on mica with varying deposition time. A morphology evolution with the film thickness increase, as evidenced in fig 4.7 a-d, is characterised an increasing connectivity. This behaviour is related to the increasing deposition time which allows for increased diffusion and migration of deposited atoms on the substrate surface. As the time of deposition increases, the small grains become larger. The grain sizes ranges from (200 nm) to (252 nm). This is an epitaxial growth with growth model of Volmer-Weber (island growth).

There is a growth competition that starts among the neighbouring crystals in the case of different orientation, according to type of growth faces. The faster growing crystals grows over slower ones as seen in fig 4.7b, and this is terminated only when the crystals exhibit the same type of crystal faces proceed to the face surface. This competition leads to change in surface morphology and texture along the film thickness. As the film grows from 10 to 154 nm thickness, there is island coalescence. The complete coalescence of the contacting crystals is a periodic process during the film growth and, besides the increase of grain size. Small grains are absorbed by larger grains increasing the radius and height. While being absorbed, the surface energy is reduced. Hence atoms leave small islands more readily than large island. The grains are percolating and the percolation threshold is at 10 min [4].

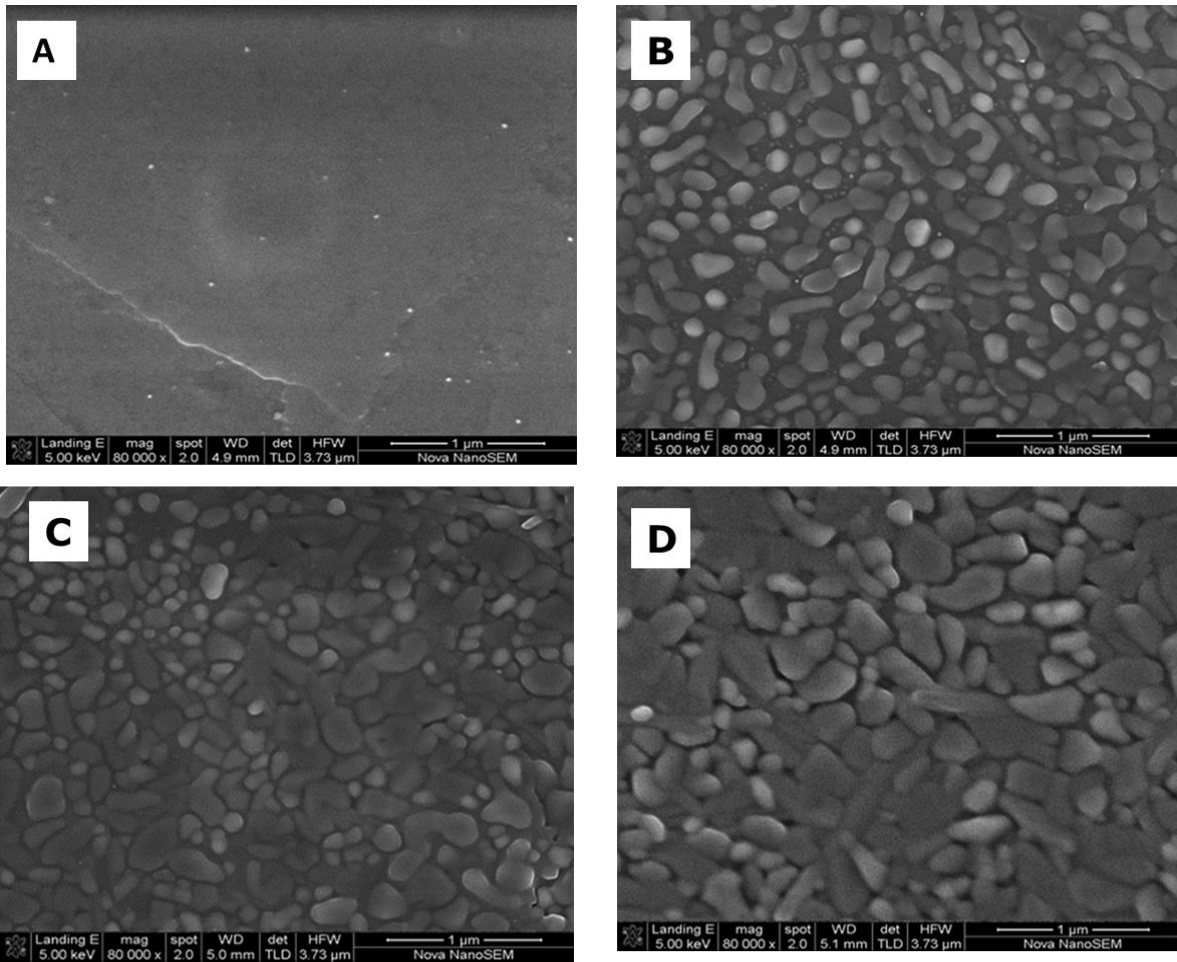


**Figure 4. 7** shows SEM images of VO<sub>2</sub> on mica for thickness of (a) 34.8 nm, (b) 138.6 nm, (c) 154.9nm, (d) 348.1 nm

## 4.6 Electrical measurements

The resistance versus temperature curves for VO<sub>2</sub> films are shown in Figures 4.8 (a) – (d). The transition temperatures were derived from the temperature derivative of the resistance  $dR/dT$ .  $((dR/dT)-R(T))$ . The temperature at which  $(dR/dT)-R$  just becomes equal to zero is taken to define the semiconductor to- metal transition (SMT) temperature both heating temperature ( $T_H$ ) and cooling temperature ( $T_C$ ) branches of the hysteresis loop. The semiconductor to-metal transition temperature ( $T_{SMT}$ ) is then defined by  $T_{SMT} = (T_H + T_C)/2$ , and the hysteresis by  $\Delta T = (T_H - T_C)$ . These definitions yield the results in table below.

**Table 4.2** summary of the electrical results

<b>Sample thickness</b>	<b>34.8 nm</b>	<b>138.6 nm</b>	<b>154.9 nm</b>	<b>348.1 m</b>
<b>Grain size</b>	200 nm	209 nm	213 nm	243 nm
<b>Heating Temperature</b>	70°C	70°C	71°C	61.87°C
<b>Cooling Temperature</b>	63°C	64°C	65°C	67.09°C
<b>Transition Temperature</b>	67°C	67°C	68°C	64°C
<b>Hysteresis</b>	7	6	6	5
<b>Order Of Magnitude</b>	4	4	4	2

Table 4.2 shows the summary of the electrical results, where the film with smaller grain sizes promotes higher order of magnitude and higher hysteresis. *Angus et al.* [5] report on the effect of grain size on the electrical properties of VO<sub>2</sub> thin films deposited on mica, they found that bigger size have higher order of magnitude in resistance which consist with work done by *D. Brassard et al.* [6]. In our findings small grains size promote high order of magnitude in resistance as well as smaller hysteresis width, the difference compared with the work done by Angus et al. maybe related to the difference in grain size range since our films are having lower grain size. As reported into the literature single crystal VO<sub>2</sub> gives 4-5 orders of magnitude [7], this is in consistence with our results. In regards to the sharpness of the hysteresis width, our results consist within the reported value in the literature on the thermo-electrical properties of single crystal of VO<sub>2</sub>.

The changes of electrical properties of VO<sub>2</sub> thin films are usually explained as results of the competing effects between grains size, nucleation defects, grain boundaries and crystal imperfections [8, 9]. In fact the less percolated film Fig4.8(a) presents less grain boundaries and less nucleation centres thus could explain why the small grain promote smaller SMT and hysteresis width as well as bigger order of magnitude compared to the film in Fig4.8(d) where we have more percolation, more structural defect and grain boundaries. Thus, Fig4.8 (a) presents fewer defects that make it more conductive than the Fig 4.8(d). In other words, it would require less driving force in order to change from tetragonal to monoclinic phase. This could be attributed to the lack of nucleation defect and the large interfacial energies which are determined by the characteristics of the particles in the deposited films shown Fig 4.8(a) to 4.8(d) namely the small grain and spheroidal grains. The smaller the grain size, the smaller is the density of nucleation defects, similarly the bigger the grain size the higher the density of nucleation defects [8]. Compared with the granular VO<sub>2</sub> nanoparticles sample, with more nucleation defects containing dislocations, grain boundaries, or other structural imperfections [8], the above discussion helps explain why the smaller grain size promote smaller transition temperature and smaller hysteresis width. As a result, we could conclude that the effect of the nucleation defect, dislocations, grain boundaries are predominant to contribute to the electrical properties changes of the films compared to the effect of grain size.

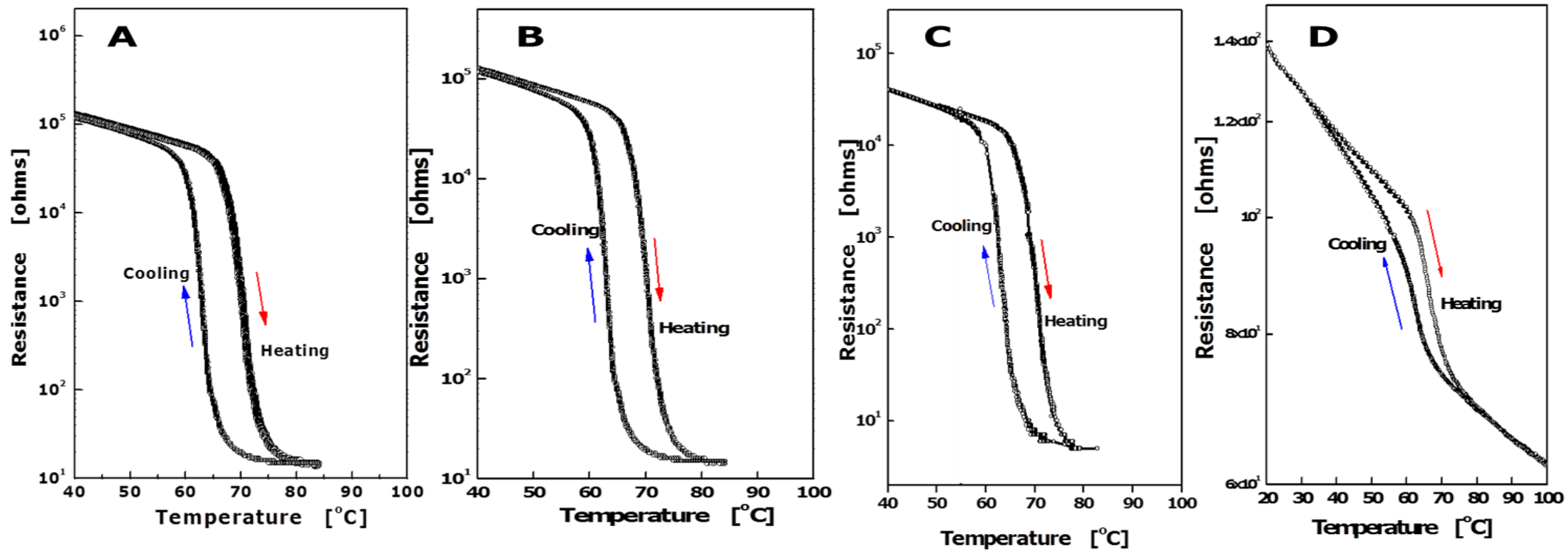


**Figure 4. 8** shows the electrical resistance as a function of temperature of VO<sub>2</sub> on mica for the thickness of (a) 34.8 nm, (b) 138.6 nm, (c) 154.9nm, (d) 348.1 nm

## 4.7 X-ray photoelectron spectroscopy

The XPS spectra for the 4 samples of VO<sub>2</sub> is given in figure 4.9 with corresponding deposition time measured at room temperature. The spectra are recorded at room temperature and show a typical two-peak structure (V2p<sub>1/2</sub> and V2p<sub>3/2</sub>) due to the spin-orbit splitting [10]. V2p<sub>3/2</sub> peak is more sensitive to phase change; hence the peak is used to identify the phase change of vanadium oxide. In fig 4.9a, the peak at 516.1 eV is attributed to V2p<sub>3/2</sub> and the peak at 530.4 eV is associated to O1s. There is a small peak at 523.7 eV, which represent the V2p<sub>1/2</sub> line. The V2p<sub>3/2</sub> peak at 516.1 eV can be attributed to V<sup>4+</sup>; the position does fit well in the reported data regions of V<sup>4+</sup><sub>2p3/2</sub> [11]. The peak binding energy and FWHM of VO<sub>2</sub> for all the samples are listed in table 4.3. The peaks values we have measured are within the binding energy range reported in the literature [12], which is attributed to the formation of VO<sub>2</sub>. It is apparent that there is no influence of thickness on the surface composition, since there is no obvious change of the surface XPS peak positions and FWHM for all the thin films on mica substrate. The peak intensities of the samples are different, indicating that the amount of VO<sub>2</sub> on the surface is different.

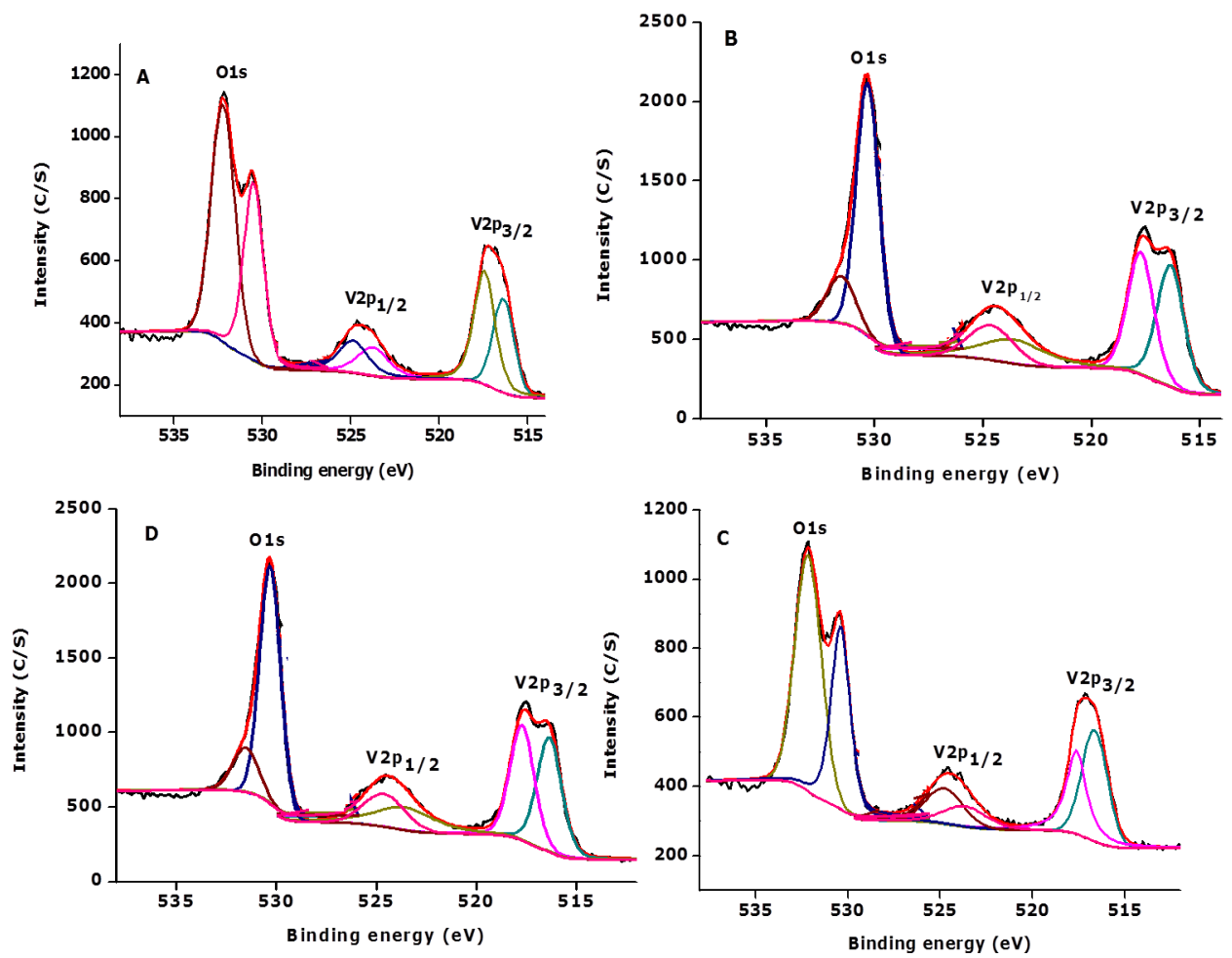


**Figure 4. 9** O1s and V2p spectra and fit of VO<sub>2</sub> on mica polycrystalline for (a) 34.8 nm, (b) 138.6 nm, (c) 154.9 n, (d) 348.1 nm

**Table 4.3** Reported V2p and O1s binding energies and FWHM for vanadium dioxide

Sample (VO <sub>2</sub> /mica)	Core line	BE (eV)	FWHM	Area	% L -G	Δ (eV)
5 min	V2p <sub>3/2</sub>	516.1	1	235	27	14.4
	O 1s	530.4	1.3	876	26	
10 min	V2p <sub>3/2</sub>	516.3	1.2	714	1	14
	O 1s	530.3	1.3	2132	0	
15 min	V2p <sub>3/2</sub>	516.6	1.6	567	2	13.8
	O 1s	530.4	1.2	732	49	
30 min	V2p <sub>3/2</sub>	516.1	1.3	885	9	14
	O 1s	530.1	1.1	1979.89	18	

## References

- [1] Peng He, Wan-Xia Huang, Jia-Zhen Yan, Mao-Yong Zhi, Jing-Han Cai, Rong-Rong Luo, *Materials Research Bulletin*, 46, 966–969, (2011)
- [2] Jung Inn Sohn, Heung Jin Joo, Alexandra E. Porter, Chel-Jong Choi, Kinam Kim, Dae Joon Kang, and Mark E. Welland. *Nano Lett.*, 7 (6),1570-1574, (2007)
- [4] I. Petrov, P.B Barna, L.Hultman, J.E Greene, *J. Vac. Sci. Technol. A*, 21, S117-S128, (2003)
- [5] Angus Gentle, Abbas Maarooof and Geoff Smith, *Current Applied Physics* 8, 229-232 (2008)
- [6] D. Brassard, S. Fournaux, M. Jean-Jacques, J. C. Kieffer. M. A. El Khahani, *Appl. Phys. Lett.* 87, 205118 (2005)
- [7] P.B. Allen, R.M. Wentzcovitch, W.W. Schultz, *Phys. Rev. B.* 48, 4359 (1993)
- [8] J.Y. Suh, R. Lopez, L.C. Feldman, R.F. Haglund, *Journal of Applied Physics* 96, 1209 (2004).
- [9] R. Lopez, T.E. Haynes, L.A. Boatner, L.C. Feldman, R.F. Haglund Jr., *Physical Review B* 65, 22411 (2002)
- [10] E. U. Donev, R. Lopez, L. C .Feldmant, R. F. Haglund, *Nano Letters* 9, 702 (2009)
- [11] D.H. Youn, H.T. Kim, B.G. Chae, Y.J. Hwang, J.W. Lee, S.L. Maeng, K.Y. Kang, *J. Vac. Sci. Technol. A* 22 719 (3), (2004)
- [12] J. Cui, D. Da, W. Jiang, *Appl. Surf. Sci.* 133, 225, (1998)

# Chapter 5

## Irradiation of VO<sub>2</sub>

### 5.1 Surface morphology of irradiated VO<sub>2</sub>

Proton irradiation of 348 nm thickness of VO<sub>2</sub>/mica film was conducted using the Van de Graaf accelerator which can accelerate proton. 2MeV of energy was chosen for this study. The fluency of the protons was varied in the range of  $18 \times 10^{15} \text{ cm}^{-2}$  to  $210 \times 10^{15} \text{ cm}^{-2}$ . The vacuum pressure in the chamber was set to  $10^{-5} \text{ Pa}$ . during the experiment; the proton beam was perpendicular to the VO<sub>2</sub>/mica film side. Proton-beam irradiation has been proposed as an alternative way to modify the physical properties and the surface structures of VO<sub>2</sub> samples. With high-energy proton beams, especially with the Bragg peak energy impact on VO<sub>2</sub>, one may predict change in the surface morphology due to defects induced on the surface of the VO<sub>2</sub> [1]. Change in surface morphology was examined by Scanning electron microscopy (SEM); fig 5.1a-f shows the SEM morphology after being irradiated with various fluencies. It can be seen that the surface of the sample is flat and consist of grains before proton irradiation (chapter 4 fig 4.2). Some rod-like structure appears on the surface of the VO<sub>2</sub>/mica film under the fluency of  $18 \times 10^{15} \text{ cm}^{-2}$ . The rod-like structure further increases with increasing proton fluency, as shown in fig 5.1d. There are spherical particles on the film appearing together with the rod-like structure. These spherical particles are due to the temperature of irradiated surface which increases due to beam heat. The spherical particles increases with increasing fluency, with only few minor rod-like structures left for the fluency  $210 \times 10^{15} \text{ cm}^{-2}$ . The spherical particles increases with increasing fluency, therefore, it is believed that the temperature rises, to a given extent.

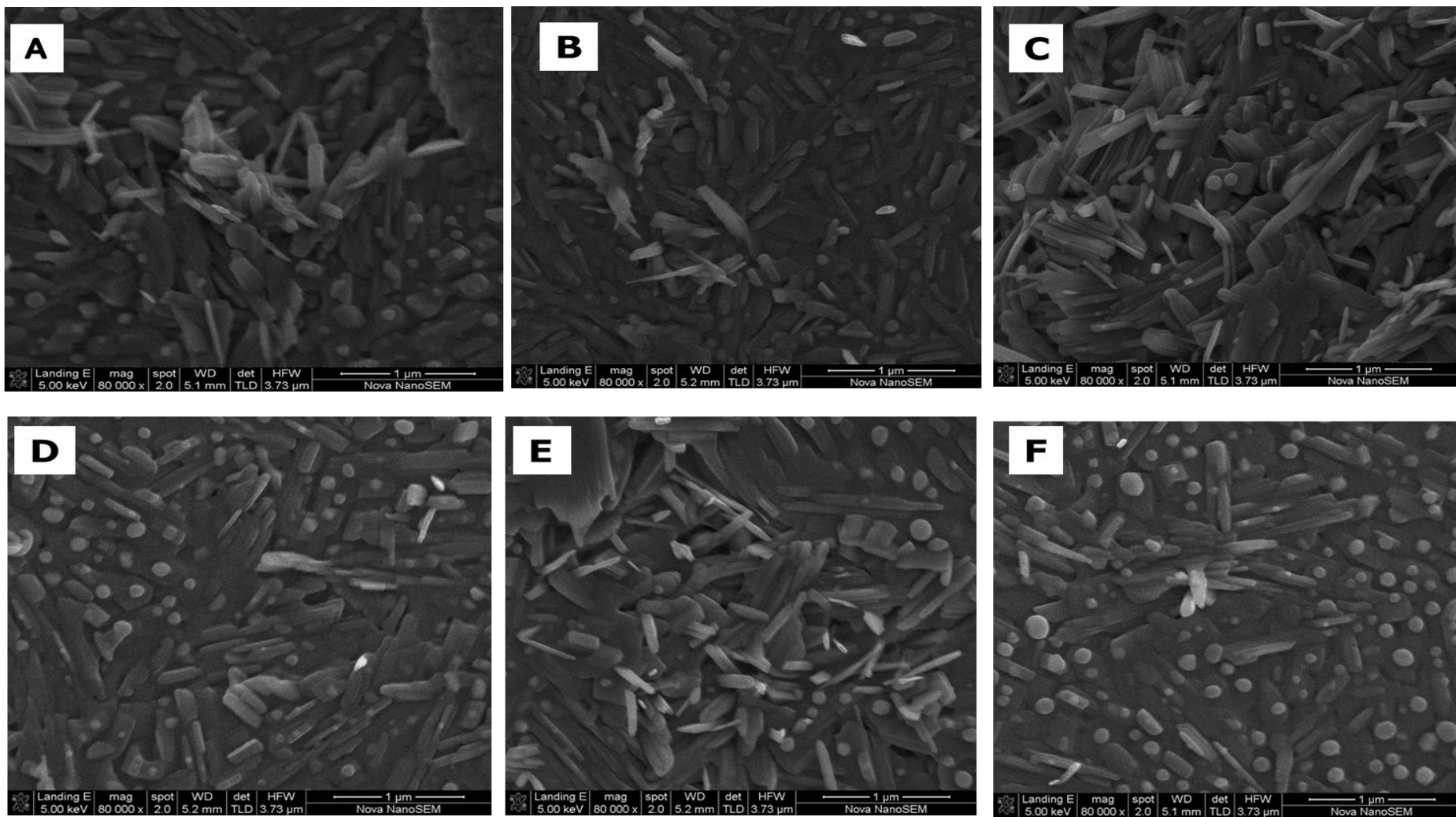


**figure 5.** 1 shows the SEM images of  $\text{VO}_2$  on mica with fluency of (a)  $18 \times 10^{15}$  ions  $\text{cm}^2$ , (b)  $36 \times 10^{15}$  ions  $\text{cm}^2$ , (c)  $72 \times 10^{15}$  ions  $\text{cm}^2$ , (d)  $110 \times 10^{15}$  ions  $\text{cm}^2$ , (e)  $140 \times 10^{15}$  ions  $\text{cm}^2$ , (f)  $210 \times 10^{15}$  ions  $\text{cm}^2$

## 5.2 Surface topology

Figure 5.2 shows the AFM roughness versus fluency graph. The rod-like structure increases and reaches a maxima (fluency of  $110 \times 10^{15} \text{ cm}^{-2}$ ) and then decreases. The surface roughness was obtained from the NANO-scope software. Only the mean roughness of the film is reported. The roughness value increases but suddenly decreases, at fluency  $110 \times 10^{15} \text{ cm}^{-2}$ , with further increasing fluency. It can be seen that the fluency of  $110 \times 10^{15} \text{ cm}^{-2}$ , the ion-beam energy deposited in the sample induces large quantity of rod-like structure on the surface increasing the surface roughness. After the fluency of  $110 \times 10^{15} \text{ cm}^{-2}$ , the roughness decreases, this can be due to melting of  $\text{VO}_2/\text{mica}$  film. This roughness Variation is suggested to be caused by the change in grain orientation.

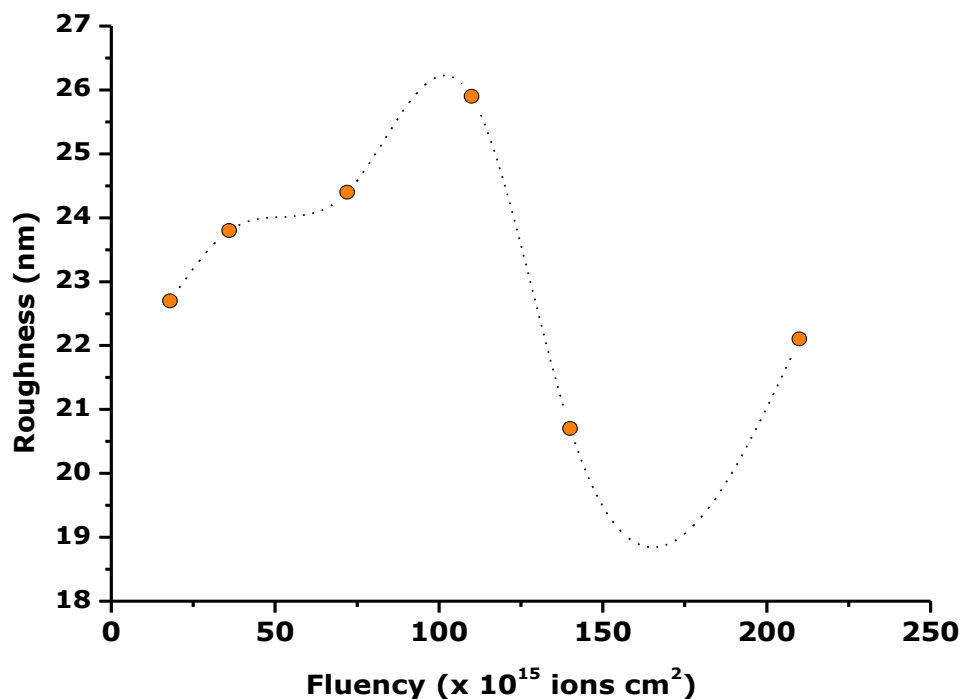


**figure5. 2** Graph showing the roughness v/s fluency of  $\text{VO}_2$  on mica irradiated thin film

### 5.3 Raman Study of VO<sub>2</sub>

Raman-scattering measurements have been used to study vibrational modes of thin films. Raman spectroscopy data of the VO<sub>2</sub> samples were collected using a T64000 micro-Raman spectrometer from HORIBA scientific, Jobin Yvon Technology equipped with a triple monochromator system to eliminate contributions from the Rayleigh line. All samples were analysed with a 514 nm Argon excitation laser (12 mW at laser exit to avoid thermal effects), a 50 x objective with recording times ranging between 120 s and a resolution of 2 cm<sup>-1</sup>. The Raman spectra of the non-irradiated and irradiated samples are shown in fig5.3 and fig5.4 respectively. The Raman spectrum in a range of 100 – 800 cm<sup>-1</sup> is dominated by the peaks at 194, 260, 412, and 700 cm<sup>-1</sup> for non-irradiated VO<sub>2</sub> and 141, 196, 268, 407, 693 cm<sup>-1</sup> for irradiated VO<sub>2</sub>.

The peak at 693 cm<sup>-1</sup> is assigned to the doubly coordinated oxygen (V<sub>2</sub>-O) stretching mode which results from corner-shared oxygen in common to three pyramids. The peak at 407 cm<sup>-1</sup> is assigned to the bending vibration of the V = O bonds. The low frequency Raman peak at 196 cm<sup>-1</sup> is assigned to the stretching mode of (V<sub>2</sub>O<sub>2</sub>)<sub>n</sub> which correspond to the film translation [2]. The peak at 141 is assigned to B<sub>1g</sub> [3]. The peaks at 268 and 445 are assigned to B<sub>g</sub> mode and peak at 499 an A<sub>g</sub> mode [4].

The peak at 144 cm<sup>-1</sup> for non-irradiation has shifted to intense 141 cm<sup>-1</sup> after irradiation and the peak at 194 cm<sup>-1</sup> has shifted to 196 cm<sup>-1</sup> respectively. As observed from the SEM results, the enhancement of the intensity of Raman peaks also mean after crystallization, crystalline growth grow up. But at some time, several heterophases appears which induces some weak peak in the Raman spectra after irradiation because of the morphology defects of the films.

**Table 5.1** Raman modes for VO<sub>2</sub> thin films

Present work			M. Pan et al		P. Schilba
Non-irradiated	irradiated				
144	141	B <sub>1g</sub>			149
194 A <sub>g</sub>	196	A <sub>g</sub>	194	A <sub>g</sub>	199
219	268	B <sub>g</sub>	265	B <sub>g</sub>	A <sub>g</sub>
260 A <sub>g</sub>					
308 A <sub>g</sub>	325		339	B <sub>g</sub>	339
412	407				B <sub>g</sub>
	445	B <sub>g</sub>	444	B <sub>g</sub>	
	499	A <sub>g</sub>	489	B <sub>g</sub>	
621 A <sub>g</sub>	601		618	A <sub>g</sub>	444
	643		650	B <sub>g</sub>	B <sub>g</sub>
	693				489
700					B <sub>g</sub>
755					618
					A <sub>g</sub>
					670
					B <sub>g</sub>

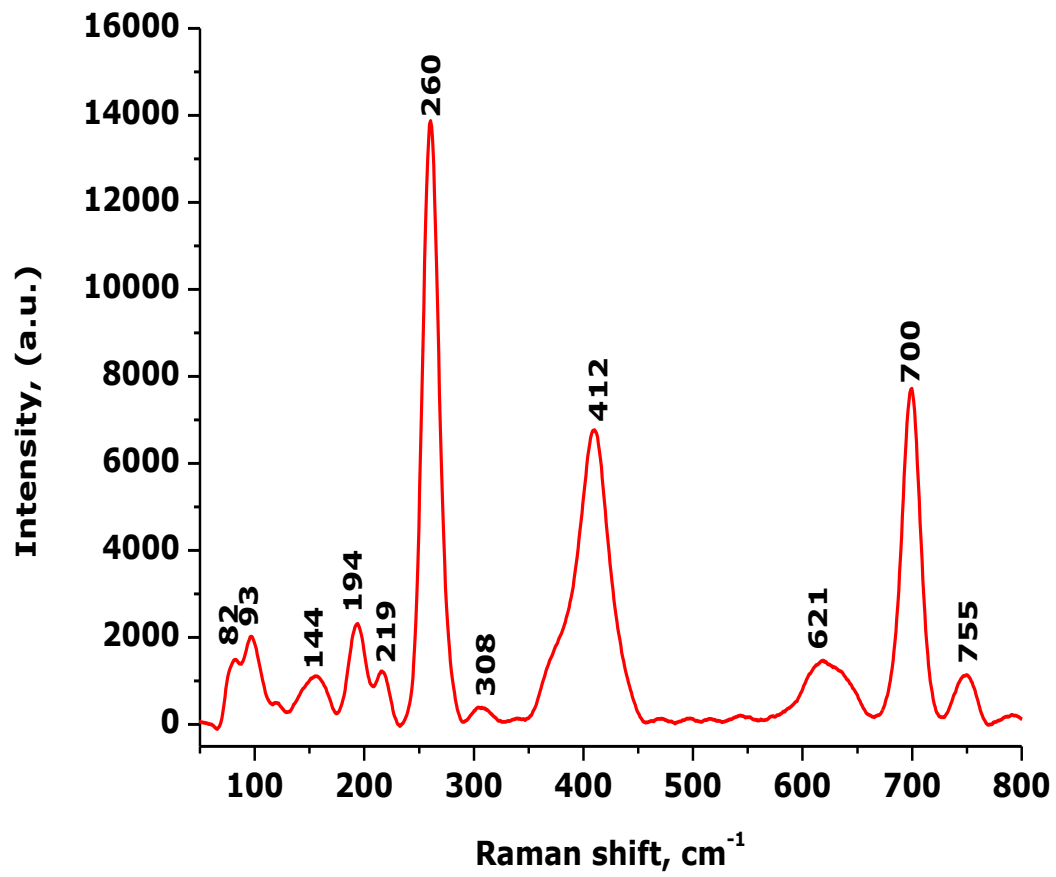


**figure5. 3** Raman shift of non-irradiated VO<sub>2</sub> on mica

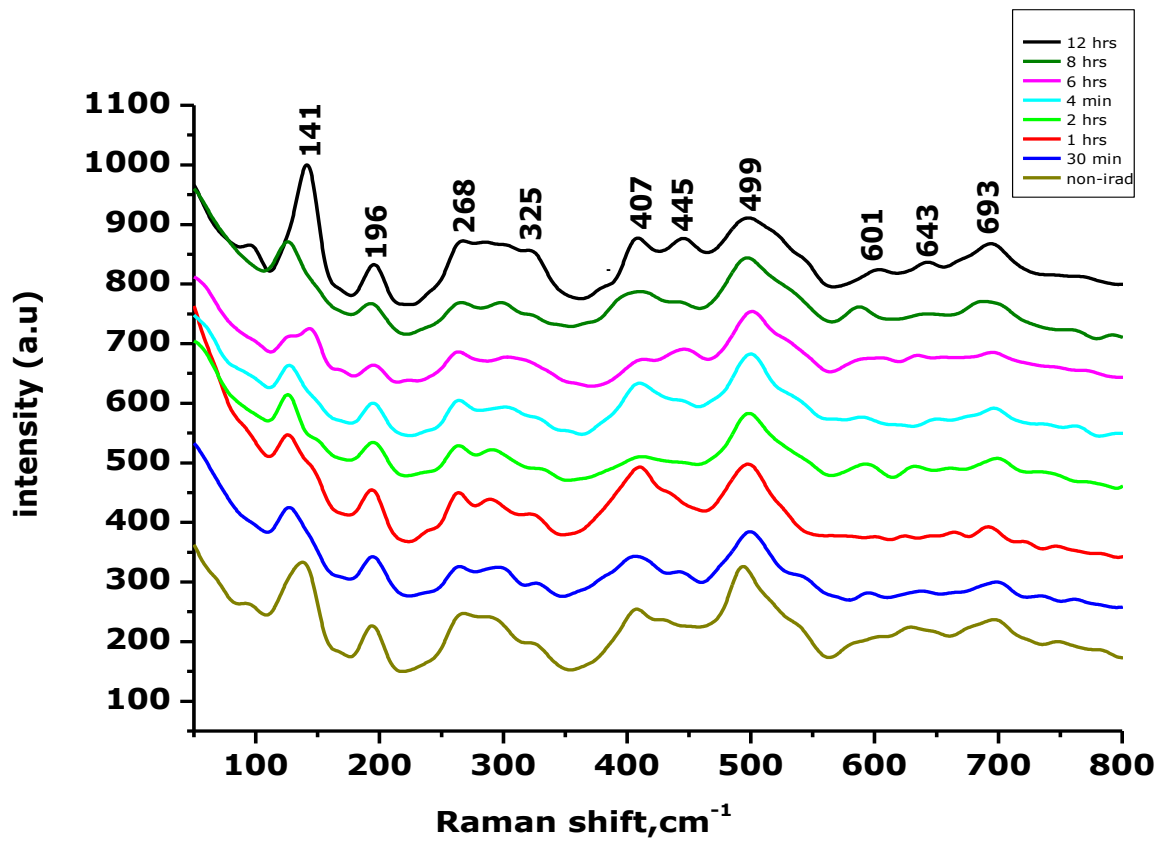


**figure5. 4** Raman shift of irradiated VO<sub>2</sub> on mica

## References

- [1] Jae-Kyun Jeon, Jeonggil Lee, Euikwoun Kim, Yun-Man Lee, Sang-Hwa Lee, Hyemin Shin, Soo-Bin Choi and Jae-Yong Kim, journal of the Korean physical society, 54 (5), 2046-2049, (2009)
- [2] Wen Chen, Liqiang Mai, Junfeng Peng, Qing Xu, and Quanyao Zhu , Journal of Solid State Chemistry 177, 377-379, (2004)
- [3] Manil Kang, Sok Won Kim, Ji-Wook Ryu, and Taejong Noh, AIP Advances 2, 012168 (2012)
- [4] Xiang-Bai Chen, Journal of the Korean Physical Society, 58 (1), 100-104, (2011)

## Chapter 6 Conclusion

In his work we showed that the thin films of monoclinic VO<sub>2</sub> of high quality can be deposited on Mica substrate by Pulsed laser deposition under optimized conditions. Time of deposition was varied to obtain the different thicknesses of the films. The effect of thickness on the microstructure and SMTs of crystalline VO<sub>2</sub> thin films were investigated. The XRD confirmed the monoclinic structure of the films with the orientation in the VO<sub>2</sub> (011). The morphology evolution within the films is characterised by a change from isolate, multiply-connected less-percolating islands to a percolating granular film. The grain sizes increases with increasing time of deposition (30 - 252 nm) and film thickness from 10 - 348 nm. For RBS results the films exhibit stoichiometric VO<sub>2</sub> with the same elemental concentration irrespective of the thickness which confirms the purity of the deposited VO<sub>2</sub> thin films.

The electrical investigation shows that smaller grains sizes promote higher order of magnitude and smaller hysteresis width which found to be in contradiction with what have been reported in the literature. This is being attributed to the lack of nucleating defects and the large interfacial energies which are determined by the characteristics of the particles in fig 4.6 (a) compared to the fig 4.6 (d). As a result, we could note that the effect of the nucleating defects, dislocations, grain boundaries are predominant to contribute to the electrical properties of the films compared to the effect of grains size. This study shows that VO<sub>2</sub> with good electrical properties that are much closer those of VO<sub>2</sub> single crystal can be deposited directly on mica substrate without post treatment.

The 348 nm film was irradiated by protons under different fluencies and the morphology evolution was observed using SEM. The film changes from film with grain to rods like structured film. The rod-like structure further increases with increasing proton fluency. The spherical particles formed on the film are due to the temperature of irradiated surface which increases due to beam heat. The spherical particles increases with increasing fluency, with only few minor rod-like structures left for the fluency  $210 \times 10^{15} \text{ cm}^{-2}$ . Vibrational modes of the irradiated VO<sub>2</sub> film was studied by Raman spectroscopy, modes belonging to VO<sub>2</sub> were identify (141, 196, 268, 407, 693, 445, 499 cm<sup>-1</sup>).